VILNIUS UNIVERSITY
LIFE SCIENCES CENTER

Melissa Maria Misar

Establishment of Hypoxia-Inducible Factor Knockouts in Pancreatic Cancer Cells via MuLE CRISPR/Cas9 System

Master's Thesis

Genetics study program

Thesis supervisor

Dr. Giancarlo Russo

Academic consultant

Rūta Matulevičiūtė

Thesis completed at

VU LSC-EMBL PI, Group for Genome Informatics and Sequencing

Vilnius 2025

Table of Contents

Abbreviations

AAV – Adeno-associated virus

ADM – Acinar-to-ductal metaplasia

bHLH – Basic helix-loop-helix (protein domain)

CAF – Cancer-associated fibroblast

cDNA – complementary DNA

CSC – cancer stem cell

C-TAD – C-terminal transactivation domain (protein domain)

Cq – quantification cycle

DMEM – Dulbecco's Modified Eagle Medium

DSB – double-strand break

dsDNA – double-stranded DNA

ECM – extracellular matrix

EMT – Epithelial-to-mesenchymal transition

FACS – Fluorescence-activated cell sorting

FBS – Fetal Bovine Serum

HDR – homology-directed repair

HIF – Hypoxia-inducible factor (protein family)

HRE – hypoxia-response element

HS – Horse Serum

IPMN – Intraductal mucinous neoplasm

LB – Luria-Bertani

MCN – Mucinous cystic neoplasm

MMP – Matrix Metalloproteinase Family (protein family)

MOI – Multiplicity of Infection

MuLE – Multiple Lentiviral Expression

N-TAD – N-terminal transactivation domain (protein domain)

NHEJ – non-homologous end joining

NTC – No-template control

OD – optical density

ODDD – oxygen-dependent degradation domain (protein domain)

PAM – protospacer adjacent motif

PanIN – Pancreatic intraepithelial neoplasia

PAS – Per-ARNT-Sim (protein domain)

PDAC – Pancreatic ductal adenocarcinoma

PEI – Polyethylenimine

PenStrep – Penicillin-Streptomycin

pMuLE – Plasmid for Multiple Lentiviral Expression

pO_2 – partial oxygen pressure

Pol – Polymerase (HIV-1 enzyme polyprotein)

RAS – rat sarcoma (protein family)

ROS – reactive oxygen species

RT – reverse transcription

RT-qPCR – Real-Time Quantitative PCR

sgRNA – Single-guide RNA

TF – Transcription factor

TME – Tumor microenvironment

TSG – Tumor suppressor gene

TU – Transduction Units

VEGF - Vascular Endothelial Growth Factor Family

Abstract

VILNIUS UNIVERSITY
LIFE SCIENCES CENTER

Melissa Maria Misar

Master's thesis

Establishment of Hypoxia-Inducible Factor Knockouts in Pancreatic Cancer Cells via MuLE CRISPR/Cas9 System

ABSTRACT

Pancreatic ductal adenocarcinoma (PDAC) is a highly lethal malignancy characterized by a severely hypoxic tumor microenvironment (TME), which promotes tumor progression and therapy resistance. Hypoxia-inducible factors (HIFs) are central mediators of the cellular response to low-oxygen conditions, but their isoform-specific functions in PDAC remain insufficiently understood.

This thesis aimed to establish the Multiple Lentiviral Expression (MuLE) system as a platform for the isoform-specific knockout of *HIF1A*, *HIF2A*, and *HIF3A* in the human PDAC cell line MIA PaCa-2. The objectives included the construction of single-guide RNA (sgRNA) and Cas9-expressing MuLE vectors, generation of lentiviral particles, optimization of transduction and selection protocols, and preliminary transcriptional profiling of wild-type cells under hypoxia.

Functional MuLE constructs were successfully assembled and validated. Transduction and selection of MIA PaCa-2 cells were optimized using fluorescence and antibiotic resistance. In parallel, wild-type cells were subjected to defined hypoxic conditions, with and without pharmacological inhibition of HIF-1α using the small-molecule inhibitor CAY10585. Transcriptional profiling revealed a general downregulation of HIFs and selected hypoxia target genes under hypoxia, whereas HIF-1α inhibition partially restored their expression, suggesting a complex, context-dependent regulatory mechanism.

Together, this work demonstrates the potential of the MuLE system for isoform-specific gene targeting in PDAC and provides a methodological foundation for further functional studies. Continued work will be required to validate knockout efficiency and characterize isoform-specific phenotypes to investigate the distinct roles of HIF isoforms in the cellular adaptation to hypoxia.

Santrauka

VILNIAUS UNIVERSITETAS
GYVYBĖS MOKSLŲ CENTRAS

Melissa Maria Misar

Magistro baigiamasis darbas

Hipoksijos indukuojamų faktorių nokautų kūrimas kasos vėžio ląstelėse naudojant MuLE CRISPR/Cas9 sistemą

SANTRAUKA

Kasos adenokarcinoma yra itin piktybiškas vėžinis susirigimas, pasižymintis hipoksiška naviko mikroaplinka, kuri skatina naviko progresavimą ir pasižymi atsparumu gydymui. Hipoksiją indukuojantys veiksniai (angl. hypoxia-inducible factors, HIF) tarpininkauja ląstelių prisitaikyme prie mažo deguonies kiekio, tačiau jų izoformų vaidmuo kasos vėžyje dar menkai žinomas.

Šio darbo tikslas – sukurti daugialypės lentivirusinės ekspresijos (angl. Multiplexed Lentiviral Expression, MuLE) sistemą kaip platformą *HIF1A*, *HIF2A* ir *HIF3A* izoformų nokautų kūrimui žmogaus kasos vėžio ląstelių linijoje MIA PaCa-2. Tyrimo metu siekiama sukurti vedančiąją RNR ir Cas9 baltymo raišką turinčius MuLE vektorius, sukurti lentivirusines daleles, optimizuoti transdukcijos ir atrankos protokolus ir atlikti preliminarų Mia PaCa-2 ląstelių transkripcijos profiliavimą hipoksijos sąlygomis.

Tyrimo metu buvo sėkmingai surinkti ir patvirtinti funkcionalūs MuLE konstruktai. MIA PaCa-2 ląstelių transdukcija ir atranka buvo optimizuotos naudojant fluorescenciją ir atsparumą antibiotikams. Lygiagrečiai laukinio tipo ląstelės buvo veikiamos nustatytomis hipoksinėmis sąlygomis, naudojant mažos molekulės inhibitorių CAY10585 ir be jo, farmakologiškai slopinant HIF-1α. Transkripcijos profiliavimas atskleidė bendrą HIF ir pasirinktų hipoksijos taikinių genų sumažėjimą hipoksijos sąlygomis, o HIF-1α slopinimas iš dalies atkūrė jų raišką, o tai rodo sudėtingą, nuo konteksto priklausomą reguliavimo mechanizmą.

Šis tyrimas rodo, kad MuLE sistema gali būti panaudota specifinių izoformų genų nokautų ir genų raiškos analizei kasos vėžio ląstelėse ir suteikia metodologinį pagrindą tolesniems funkciniams tyrimams. Tolimesnių tyrimų metu bus siekiama patvirtinti nokautų efektyvumą. Taip pat apibūdinti konkrečiam izomero nokautui būdingus fenotipus, siekiant ištirti skirtingus ir nepersidengiančius HIF izoformų vaidmenis ląstelių prisitaikyme prie hipoksijos.

Introduction

PDAC is a highly aggressive malignancy with one of the lowest survival rates among solid tumors (National Cancer Institute, n.d.). Although it accounts for a relatively small proportion of global cancer incidence, PDAC is projected to become one of the leading causes of cancer-related deaths, primarily due to late diagnosis, limited treatment options, and resistance to conventional therapies (Stoffel et al., 2023; Bray et al., 2024). Histologically, PDAC typically originates from acinar cells of the exocrine pancreas, which undergo acinar-to-ductal metaplasia (ADM) and may progress through precursor lesions such as pancreatic intraepithelial neoplasias (PanINs). These lesions can gradually accumulate driver mutations in key oncogenes and tumor suppressor genes (TSGs), including *KRAS*, *TP53*, *CDKN2A,* and *SMAD4*, ultimately leading to the development of invasive carcinoma (Zeitouni et al., 2016; Orth et al., 2019).

A hallmark of PDAC is its severely hypoxic TME, resulting from excessive desmoplasia and dysfunctional vasculature (Koong et al., 2000; Yuen & Díaz, 2014). Hypoxia enhances malignant progression and therapeutic resistance through the stabilization and activation of HIFs, a family of transcription factors (TFs) that regulate genes involved in angiogenesis, metabolism, invasion, and immune response (Bigos et al., 2024; Shi & Gilkes, 2025). While the roles of HIF-1α and HIF-2α have been extensively studied, the functional relevance of HIF-3α in PDAC remains poorly characterized (Ravenna et al., 2016; Zhou et al., 2018). Emerging evidence indicates that HIF isoforms can exert distinct and sometimes opposing effects on tumor progression, depending on oxygen availability, cellular context, and duration of hypoxic exposure (Loboda et al., 2010; Ravenna et al., 2016; Zhang et al., 2017). A deeper understanding of their isoform-specific roles is crucial to uncovering new therapeutic targets in PDAC.

CRISPR/Cas9 technology has emerged as a powerful tool for dissecting gene function through targeted knockout. Multiplexed approaches, in particular, allow the simultaneous disruption of several genes, enabling the analysis of gene interactions and functional redundancies (McCarty et al., 2020). The MuLE system offers an efficient platform for lentiviral delivery of Cas9 and multiple sgRNAs into mammalian cells, allowing stable and multiplexed gene knockout (Albers et al., 2015). While this system has been applied in other cancer models, its potential for isoform-specific gene targeting in PDAC remains unexplored.

This study focuses on the establishment of the MuLE system for the targeted knockout of *HIF1A*, *HIF2A*, and *HIF3A* in the human PDAC cell line MIA PaCa-2. This cell line harbors typical PDAC-associated mutations and exhibits considerable phenotypic plasticity, making it a suitable model for hypoxia-related research (Gradiz et al., 2016; Sasaki et al., 2020). In parallel to knockout construct generation, wild-type MIA PaCa-2 cells were exposed to defined hypoxic conditions, with

and without pharmacological inhibition of HIF-1α, to establish a preliminary transcriptional reference baseline. Together, these approaches aim to lay the foundation for future studies investigating the isoform-specific roles of HIFs in hypoxia-driven tumor behavior in PDAC.

Aim of the thesis:

To establish the MuLE system as a stable and efficient platform for isoform-specific knockout of *HIF1A*, *HIF2A*, and *HIF3A* in the human pancreatic cancer cell line MIA PaCa-2.

Objectives:

1. To construct sgRNA-expressing entry vectors targeting *HIF1A*, *HIF2A*, or *HIF3A* as a basis for isoform-specific gene disruption using the MuLE system.
2. To generate MuLE-based lentiviral constructs enabling targeted knockout of individual HIF isoforms.
3. To produce and validate lentiviral particles carrying HIF-targeted CRISPR/Cas9 components for efficient delivery into mammalian cells.
4. To evaluate the integration and expression efficiency of MuLE constructs in MIA PaCa-2 cells using fluorescence and antibiotic resistance as indicators of successful vector delivery.
5. To define hypoxia-induced transcriptional changes in wild-type MIA PaCa-2 cells under 1 % O_2, with and without pharmacological inhibition of HIF-1α using the small-molecule inhibitor CAY10585, to provide a baseline for further comparative analysis.

1. Literature Review

1.1. Pancreatic Cancer

1.1.1. Global Burden and Biological Origin

Pancreatic cancer is one of the most lethal malignancies worldwide, characterized by a rising incidence and persistently poor prognosis. Although it accounts for only 2.6 % of all cancers, it ranks as the sixth leading cause of cancer-related deaths globally (Bray et al., 2024). In 2022, more than 510 000 new cases and 467 000 deaths were reported, with the highest incidence rates observed in highly developed regions, particularly in Southern and Western Europe, as well as North America (Figure 1.1) (Bray et al., 2024). Within these regions, the countries of Hungary, Austria, and France reported the highest age-standardized incidence rates per capita in 2022 (Ferlay et al., 2024). Over the past years, the burden of pancreatic cancer has continued to increase (Siegel et al., 2025), particularly in highly developed countries, and it is projected to become the leading cause of cancer-related deaths in the coming decades (Stoffel et al., 2023).

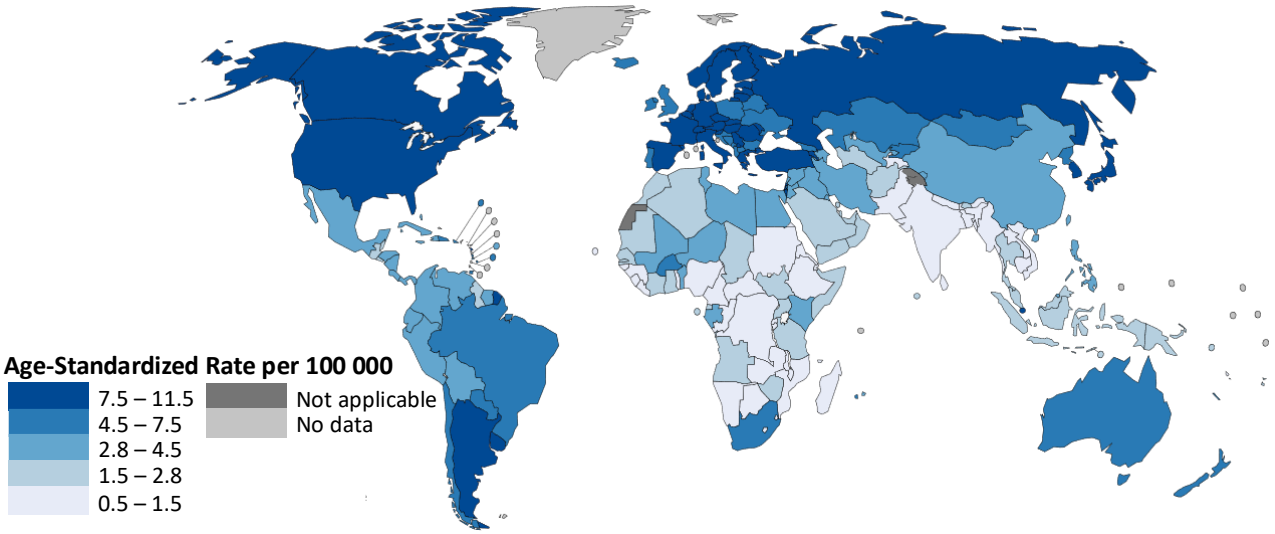

Figure 1.1 Global distribution of age-standardized incidence rates for pancreatic cancer in 2022 for both sexes by country. The figure was adapted from Ferlay et al. (2024).

PDAC is the predominant subtype of pancreatic cancer, accounting for approximately 90 % of all cases (Stoffel et al., 2023). Although PDAC exhibits ductal morphology, it predominantly originates from acinar cells of the exocrine pancreas, which synthesize digestive enzymes (Jiang et al., 2020; Neuhöfer et al., 2021). Acinar cells can transdifferentiate into duct-like progenitor cells through ADM, a process considered the initiating event in PDAC development (Orth et al., 2019). In contrast, less common pancreatic neuroendocrine tumors arise from hormone-secreting endocrine cells and are generally associated with a more favorable prognosis and slower disease progression (Rawla et al., 2019). Given its prevalence and aggressive nature, PDAC is the central focus of current research. In the scientific literature, the term “pancreatic cancer” typically refers to PDAC, while other pancreatic

tumor types such as neuroendocrine tumors are addressed separately (Stoffel et al., 2023). Accordingly, this thesis will focus exclusively on PDAC, and other pancreatic tumors will not be further discussed.

1.1.2. Clinical Relevance and Diagnostic Challenges

Given that PDAC accounts for the majority of pancreatic cancer cases, its clinical relevance is underscored by the fact that it is typically diagnosed at an advanced stage, due to the absence of specific symptoms in early disease and the lack of efficient screening (McGuigan et al., 2018). Common symptoms, such as weight loss, abdominal or back pain, jaundice, and new-onset diabetes usually appear only once the disease is in a progressed state (Park et al., 2021). Consequently, over 80 % of patients are diagnosed at a stage when the tumor is already locally advanced or metastatic (Park et al., 2021). As a result, pancreatic cancer has the lowest 5-year overall survival rate of all cancer types, remaining around 12 % (National Cancer Institute, n.d.).

Given the challenges of early detection, identifying high-risk individuals is critical for preventive or surveillance strategies. Modifiable risk factors include tobacco use, obesity, type 2 diabetes, heavy alcohol consumption, and pancreatitis (McGuigan et al., 2018; Hu et al., 2021; Stoffel et al., 2023). Non-modifiable risk factors, on the other hand, include increasing age, a family history of pancreatic cancer, and inherited genetic predispositions – particularly pathogenic germline variants in genes associated with hereditary cancer syndromes, such as hereditary breast and ovarian cancer syndrome and Lynch syndrome (McGuigan et al., 2018; Hu et al., 2021; Stoffel et al., 2023).

PDAC remains highly lethal with limited treatment options and poor overall prognosis. Surgical resection offers the only chance for cure but is possible in less than 20 % of patients due to late presentation (McGuigan et al., 2018; Park et al., 2021). Even after complete resection, recurrence rates are high, and long-term survival is uncommon. Systemic chemotherapy remains the standard of care in both localized and metastatic disease but has limited survival benefits (Park et al., 2021). Although mutations in the *KRAS* gene are nearly universal in PDAC, effective therapeutic targeting remains challenging due to rapid development of resistance and phenotypic heterogeneity (Singhal et al., 2024). Research thus focuses on earlier detection and the identification of predictive biomarkers such as circulating tumor DNA and CA19-9, as well as the development of more effective targeted therapies (Stoffel et al., 2023).

1.1.3. Pathophysiology and Molecular Mechanisms

PDAC develops through a multistep process, starting with the development of precursor lesions and progressing toward invasive malignancy. The main precursor lesions include PanINs, intraductal papillary mucinous neoplasms (IPMNs), and mucinous cystic neoplasms (MCNs) (Park et al., 2021; Stoffel et al., 2023). While IPMNs and MCNs are less frequently involved in PDAC pathogenesis

(Stoffel et al., 2023), PanINs represent the predominant precursor lesion and typically arise through ADM from acinar cells (Figure 1.2A) (Orth et al., 2019; Neuhöfer et al., 2021). ADM usually serves as an adaptive mechanism by which acinar cells convert to a duct-like state in response to inflammation or tissue injury, supporting epithelial repair (Storz, 2017). Under normal conditions (Figure 1.2B), ADM is reversible. However, when oncogenic mutations occur – especially in the gene *KRAS* – ADM becomes dysregulated, causing cells to remain locked in a progenitor-like phenotype with an increased risk of malignant transformation (Zeitouni et al., 2016). In this way, PanIN lesions are initiated and gradually progress from low-grade dysplasia (PanIN-1A/B and PanIN-2) (Figure 1.2C) to high-grade dysplasia (PanIN-3) (Figure 1.2D) over time, establishing the foundation for subsequent pancreatic tumorigenesis (Park et al., 2021).

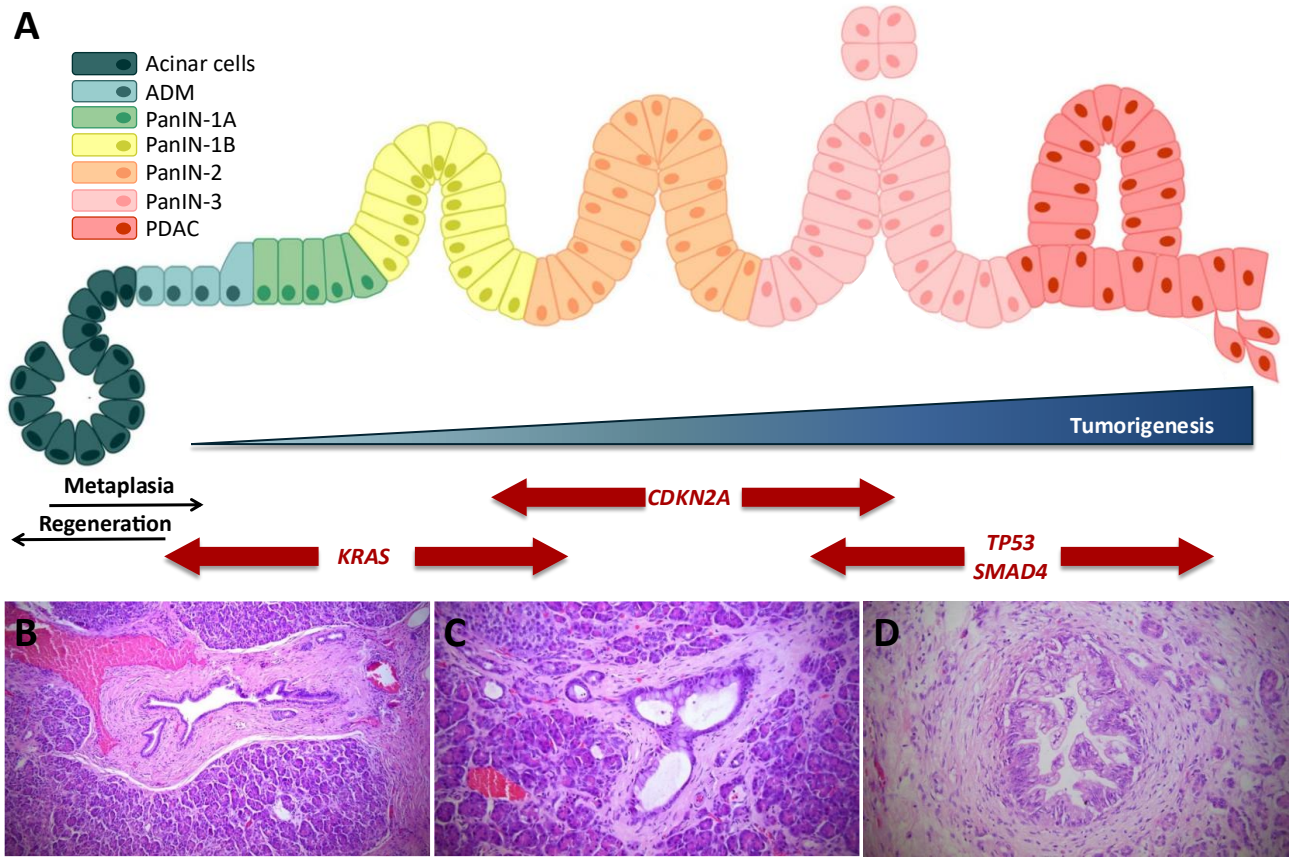

Figure 1.2 Stepwise progression toward PDAC. **(A)** Schematic overview of genetic and histological progression from normal duct to PDAC, driven by mutations in *KRAS*, *CDKN2A*, *TP53*, and *SMAD4*. The figure was adapted from Storz et al. (2017) and Orth et al. (2019). **(B-D)** Representative histologic images of human pancreatic tissue, representing normal duct **(B)**, low-grade PanIN **(C)**, and high-grade PanIN **(D)**. The figure was adapted from McGuigan et al. (2018). No error bars were provided in the original source.

This histological progression is paralleled by the stepwise accumulation of genetic alterations over many years. Activating mutations in the *KRAS* oncogene are the earliest and most common events, present in more than 90 % of PDACs and detectable already in low-grade PanINs (Park et al., 2021; Stoffel et al., 2023). *KRAS* encodes a small GTPase belonging to the rat sarcoma (RAS) family of signaling proteins. Under physiological conditions, KRAS functions as a molecular switch, cycling between an active GTP-bound and an inactive GDP-bound state to regulate cell proliferation and

survival (Zeitouni et al., 2016). In pancreatic cancer, the most frequent *KRAS* mutation involves a glycine-to-aspartate substitution at codon 12 ($KRAS^{G12D}$), which results in constant activation, promoting early proliferative and anti-apoptotic signaling (Zeitouni et al., 2016). However, *KRAS* activation alone is insufficient to drive malignancy. As PanINs progress, additional inactivation of TSGs, including *CDKN2A* (~90 %), *TP53* (~75 %), and *SMAD4* (~50 %), is commonly observed (Stoffel et al., 2023). Together, these genetic alterations disrupt critical cellular processes such as cell cycle regulation, DNA damage response, and apoptosis, thereby driving the transition from early PanIN lesions to high-grade dysplasia and ultimately to invasive PDAC (Stoffel et al., 2023).

1.1.4. MIA PaCa-2 as an *In Vitro* Model for Pancreatic Cancer

The MIA PaCa-2 cell line is one of the most widely used *in vitro* models for PDAC. It was originally established in 1975 from the tumor of a 65-year-old Caucasian male diagnosed with undifferentiated pancreatic carcinoma (American Type Culture Collection, 2024b; Leibnitz Institute DSMZ, n.d.). Classified as an epithelial cell line, MIA PaCa-2 is derived from pancreatic tissue and displays typical epithelial morphology, growing as adherent single cells or in loosely attached clusters (American Type Culture Collection, 2024b). The cell line has a doubling time of approximately 30 hours to 40 hours and exhibits a hypotriploid karyotype with a modal chromosome number of 61 (American Type Culture Collection, 2024b). Genetically, MIA PaCa-2 harbors several characteristic PDAC mutations, including activating mutations in *KRAS* and inactivating mutations in *CDKN2A* and *TP53*, while *SMAD4* remains wild-type (Simon et al., 1994; Gradiz et al., 2016).

In culture, MIA PaCa-2 cells exhibit notable morphological heterogeneity, consisting of three subpopulations described as round adherent, spindle-shaped adherent, and round floating cells (Figure 1.3A) (Sasaki et al., 2020). Importantly, the cell line demonstrates dynamic morphological plasticity, as round and spindle-shaped adherent cells can reversibly transition between forms, while some round adherent cells detach to become floating cells, which in turn can reattach and readopt an adherent morphology (Figure 1.3B) (Sasaki et al., 2020). This phenotypic flexibility is thought to reflect early steps of cell migration and metastatic progression (Sasaki et al., 2020).

On the molecular level, MIA PaCa-2 represents a hybrid epithelial-mesenchymal, or quasi-mesenchymal, phenotype. It co-expresses epithelial markers such as E-cadherin and mesenchymal markers such as vimentin, predominantly in adherent cells (Gradiz et al., 2016). On the other hand, floating cells show increased expression of mesenchymal markers, including N-cadherin, SNAI1 and SNAI2, suggesting a transitional state between epithelial and mesenchymal and an enhanced invasive phenotype (Sasaki et al., 2020). Furthermore, MIA PaCa-2 expresses cancer stem cell (CSC) markers such as CD44 and CD326, while the absence of other CSC markers such as CD133 may indicate limited metastatic capacity (Gradiz et al., 2016). These characteristics make MIA PaCa-2 a biologically relevant *in vitro* model suitable for exploring hypoxia-driven mechanisms in PDAC.

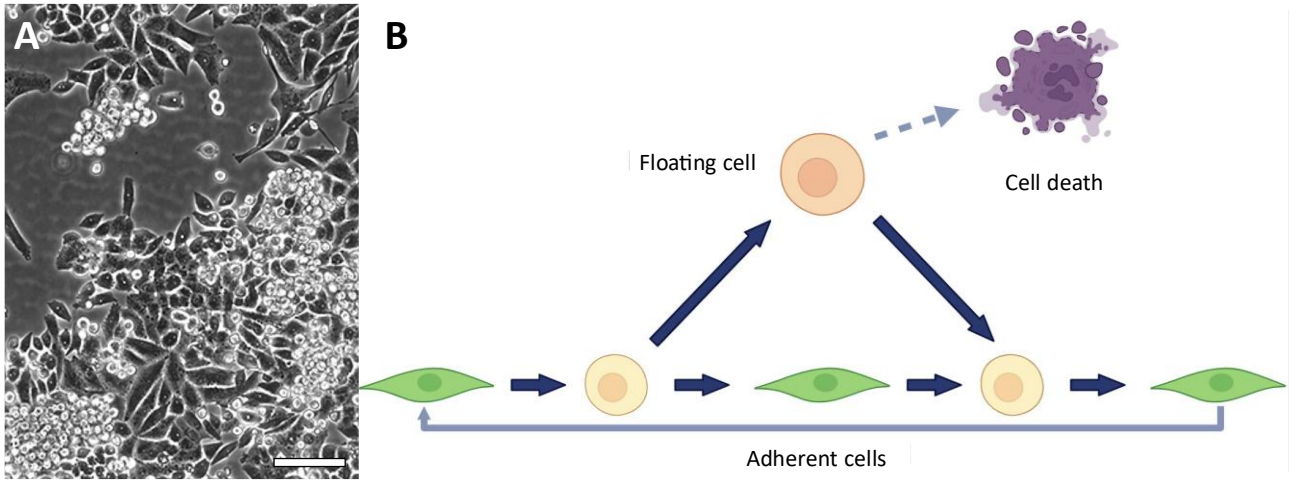

Figure 1.3 Morphology of MIA PaCa-2 cell line. **(A)** Morphology of MIA PaCa-2 cells under adherent culture conditions; scale bar: 100 µm. The figure was adapted from the American Type Culture Collection (2024b). **(B)** Schematic representation of reversible transition between different morphologies. The figure was adapted from Sasaki et al. (2020) and created with Biorender.com.

1.2. Hypoxia in Cancer Progression

1.2.1. Oxygen Gradients and Hypoxia in Solid Tumors

Hypoxia, defined as a state of reduced oxygen availability, represents a hallmark of solid tumors (Bigos et al., 2024). Under physiological conditions, tissue oxygen levels are maintained by regulation of oxygen delivery through the vasculature and its consumption by cells (Nascimento-Filho et al., 2022). In solid tumors, the high proliferation rate of neoplastic cells often exceeds the development of a functional vascular network, resulting in an inadequate oxygen supply (Vito et al., 2020). This imbalance leads to the formation of hypoxic regions within the TME, which can influence tumor progression and clinical outcomes (Vito et al., 2020).

Under physiological conditions, tissue oxygenation varies depending on vascular density and metabolic activity. For instance, well-oxygenated tissues such as the lung typically display partial oxygen pressure (pO_2) of approximately 100 mmHg (equivalent to 14 % O_2), while less perfused organs such as the pancreas maintain lower pO_2 values of around 50 mmHg (7 % O_2) (Koong et al., 2000; Nascimento-Filho et al., 2022). In contrast, solid tumors display markedly reduced oxygen levels, with moderate hypoxia defined by a pO_2 under 10 mmHg and extreme hypoxia characterized by pO_2 levels falling below 1 mmHg (Vaupel et al., 2021).

This reduced oxygenation in solid tumors emerges because of an imbalance between oxygen supply and demand. Whereas healthy tissues maintain homeostasis through an organized vasculature, tumor-induced angiogenesis results in a structurally and functionally aberrant vascular network characterized by disorganization, leakiness, and impaired perfusion (Vito et al., 2020; Bigos et al., 2024). As a result, oxygen distribution becomes spatially heterogeneous. Chronic hypoxia typically develops in regions beyond 100 µm to 200 µm from blood vessels, where oxygen diffusion becomes limited, while acute hypoxia results from temporary changes in perfusion (Vaupel et al., 2021). These hypoxic

conditions drive strong evolutionary pressure, promoting tumor heterogeneity through clonal selection (Qian & Rankin, 2019). Cells that successfully adapt to low oxygen availability acquire selective advantages that promote malignant progression (Qian & Rankin, 2019).

1.2.2. Hypoxia in PDAC

PDAC is characterized by severe hypoxia, which plays an important role in its aggressiveness and poor prognosis (Sadozai et al., 2024). Direct measurements in pancreatic tumors have shown median intratumoral pO_2 levels below 5 mmHg, showing severe hypoxia with markedly lower oxygenation compared to adjacent healthy tissues (Koong et al., 2000). These values correspond to oxygen concentrations often lower than 0.7 %, establishing PDAC as one of the most hypoxic cancer types (Koong et al., 2000).

This severe hypoxia primarily comes from the tumor's unique stromal architecture, marked by extensive desmoplasia and poor vascularization (Yuen & Díaz, 2014). The stroma, consisting mainly of extracellular matrix (ECM), activated cancer-associated fibroblasts (CAFs), and various inflammatory cells, can account for up to 90 % of the total tumor mass (Schwörer et al., 2023). The dense and fibrotic ECM physically compresses intratumoral blood vessels, impairs perfusion, and restricts oxygen delivery, thereby promoting hypoxic conditions within the TME (Yuen & Díaz, 2014). Even where new vessels form, the resulting vasculature remains structurally abnormal and functionally inefficient (Hao et al., 2021), contributing to heterogeneous oxygen distribution with regions of both chronic and acute hypoxia (Vaupel et al., 2021). In addition to promoting tumor progression, persistent hypoxia in PDAC plays a major role in limiting the effectiveness of therapeutic interventions, further worsening patient outcomes (Bigos et al., 2024). However, the specific mechanisms underlying hypoxia-induced therapy resistance will be discussed later.

1.3. HIFs in Cancer Biology

1.3.1. Structural Organization of HIFs

HIFs are the main mediators of the cellular response and adaptation under hypoxic conditions. They form a family of TFs that regulate the expression of genes involved in cellular processes such as angiogenesis, metabolism, cell survival, and invasion (Bigos et al., 2024). The HIF gene family comprises four members, namely *HIF1A*, *HIF2A* (also known as *EPAS1*), *HIF3A*, and *ARNT* (also known as *HIF1B*), which encode the proteins HIF-1α, HIF-2α, HIF-3α, and HIF-1β, respectively (Table 1.1) (Shi & Gilkes, 2025). Each gene is located on a different chromosome and undergoes alternative splicing, producing multiple transcript variants leading to modulation of function and regulatory mechanisms (Shi & Gilkes, 2025).

HIFs share a conserved structural architecture that includes a basic helix-loop-helix (bHLH) domain and a Per-ARNT-Sim (PAS) domain, both essential for dimerization and DNA binding

Table 1.1 Characterization of HIF-family members. mRNA length, exon count, protein length, and molecular mass are representative given only for the MANE Select transcript variant. Data was obtained from NCBI, Ensembl, and GeneCards.

Gene	***HIF1A***	***HIF2A***	***HIF3A***	***ARNT***
Chromosomal Location	14q23.3	2p21	19q13.32	1q21.3
Orientation	Plus	Plus	Plus	Minus
Gene Length (bp)	52 747	93 031	46 392	66 996
Transcript variants	12	10	19	12
mRNA Length (bp)	3946	5155	5856	4710
Exon count	15	16	15	22
Encoded Protein	HIF-1α	HIF-2α	HIF-3α	HIF-1β
Protein Length (aa)	826	870	669	789
Molecular Mass (Da)	92 670	96 459	72 433	86 636

(Figure 1.4) (Jiang et al., 1996). All three α-subunits possess an oxygen-dependent degradation domain (ODDD), which regulates protein stability in response to oxygen availability (Cockman et al., 2000). Additionally, HIF-1α and HIF-2α contain two transactivation domains: an N-terminal transactivation domain (N-TAD), involved in protein stability and transcriptional regulation, and a C-terminal transactivation domain (C-TAD), essential for recruiting co-activators to promote gene transcription (Arany et al., 1996). In contrast, HIF-3α lacks the C-TAD but may contain a leucine zipper domain in certain isoforms, contributing to its distinct structure and functional roles (Ravenna et al., 2016).

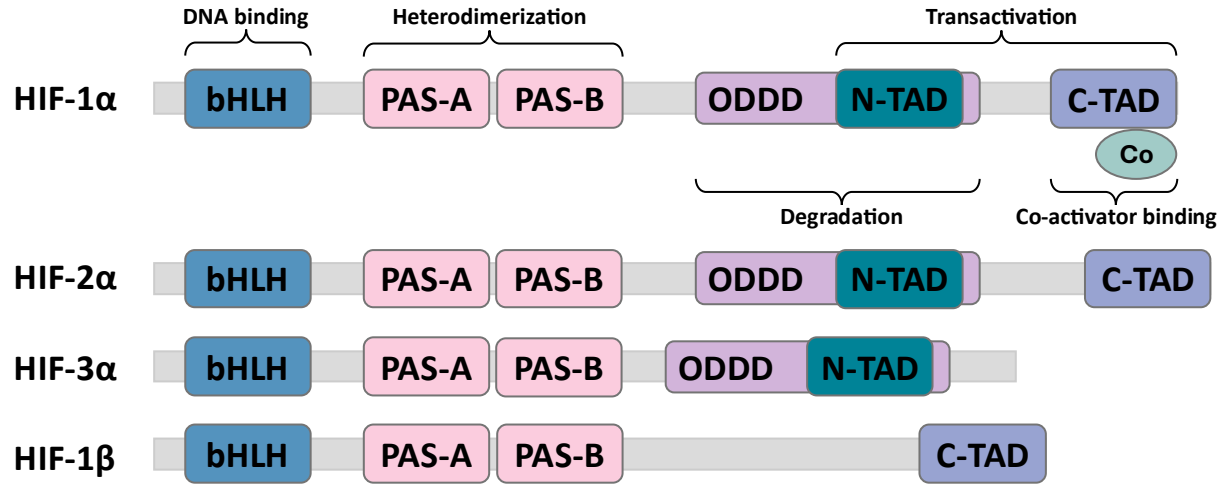

Figure 1.4 Structural domains of HIF isoforms. bHLH – basic helix-loop-helix; C-TAD – C-terminal transactivation domain; N-TAD – N-terminal transactivation domain; ODDD – oxygen-dependent degradation domain; PAS – Per-ARNT-Sim. The figure was adapted from Shi & Gilkes (2025).

Unlike the α-subunit, the β-subunit lacks an ODDD and remains stable regardless of oxygen levels (Shi & Gilkes, 2025). Structurally, HIF-1β contains the conserved bHLH and PAS domains required for dimerization and DNA binding but includes only the C-TAD (Jiang et al., 1996). It primarily serves as a binding partner, enabling nuclear localization and transcriptional activation with the α-subunit (Jiang et al., 1996). As this thesis focuses on the oxygen-sensitive α-subunits HIF-1α, HIF-2α, and HIF-3α, and their corresponding genes, HIF-1β will not be further specified or discussed.

1.3.2. Regulation and Activation of the Alpha Subunit

HIFs function as heterodimers consisting of an oxygen-sensitive α-subunit, encoded by *HIF1A*, *HIF2A*, or *HIF3A*, and a constitutively expressed β-subunit, encoded by *ARNT* (Wang & Semenza, 1995). HIF activity can be regulated by canonical and non-canonical mechanisms.

Canonical regulation involves the oxygen-dependent degradation of the α-subunit under normoxia (Figure 1.5). In this process, specific proline residues in the ODDD are hydroxylated by PHDs (Yu et al., 2001), allowing recognition by the VHL protein, which mediates ubiquitination and proteasomal degradation (Cockman et al., 2000). However, under hypoxia, PHD activity is inhibited, enabling HIF-α stabilization and accumulation (Yu et al., 2001; Shi & Gilkes, 2025). Stabilized HIF-α translocates into the nucleus, where it dimerizes with HIF-1β (Jiang et al., 1996). The resulting heterodimer, in cooperation with the transcriptional co-activators p300/CBP, binds to hypoxia-response elements (HREs) within the promoter regions of target genes, thereby promoting their transcription (Jiang et al., 1996).

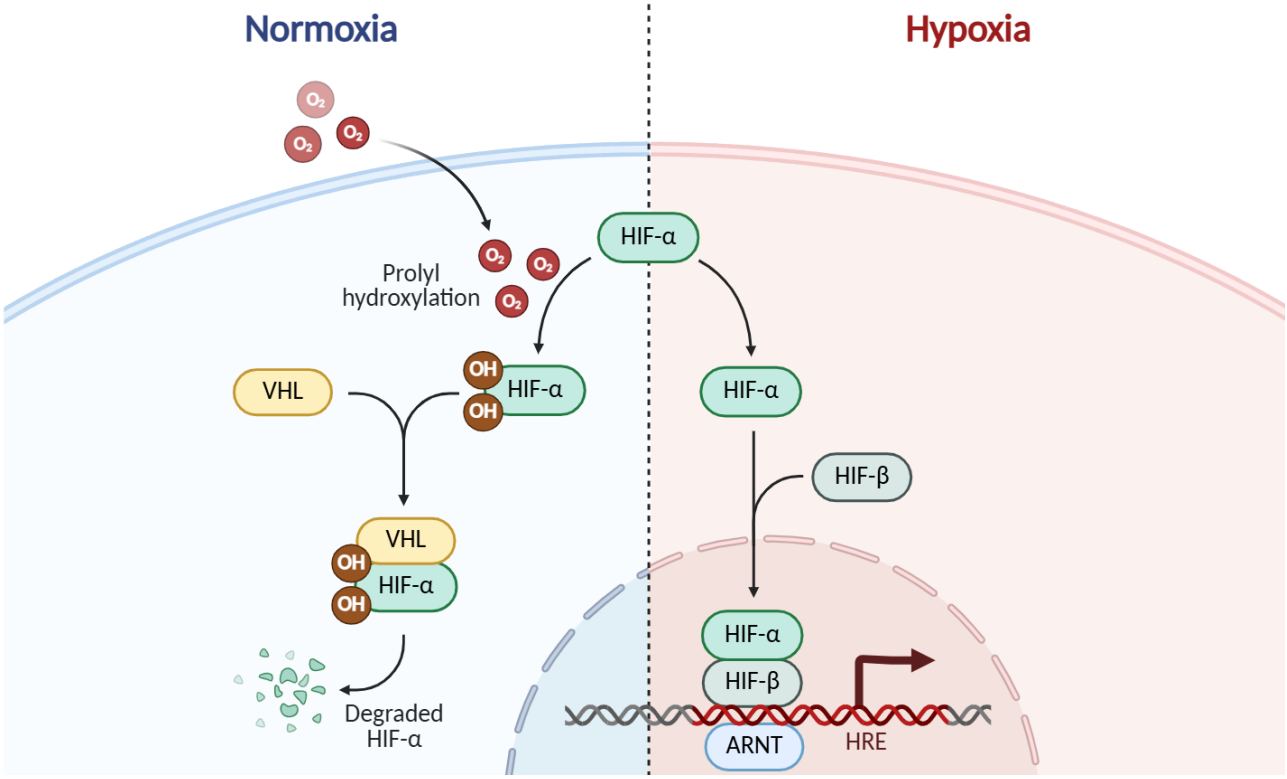

Figure 1.5 HIF signaling pathway under normoxic and hypoxic conditions through canonical mechanisms. The figure was created with Biorender.com.

An additional regulatory layer is introduced by FIH, another oxygen-dependent hydroxylase (Lando et al., 2002). FIH hydroxylates asparagine residues within the C-TAD of HIF-1α and HIF-2α, preventing their association with transcriptional co-activators p300/CBP and thereby limiting full transcriptional activation even under hypoxic conditions (Mahon et al., 2001).

Beyond canonical regulation, HIFs are also modulated by non-canonical mechanisms that function independently of oxygen levels, including post-translational and epigenetic modifications, as

well as interactions with TSGs and reactive oxygen species (ROS) (Jeong et al., 2002; Yoo et al., 2006; Parandavar & Yazdanparast, 2017). These processes further regulate HIF activity and may fine-tune cellular responses to environmental and metabolic changes. However, since this thesis primarily focuses on canonical mechanisms, non-canonical pathways will not be further explained.

1.3.3. Cellular and Microenvironmental Adaptation to HIF Activation

As a hallmark of solid tumors, hypoxia acts as a driver of tumor progression by influencing both cancer cell behavior and the surrounding TME. The limited oxygen availability in solid tumors drives selective pressure that induces transcriptional and metabolic reprogramming that enables cancer cells to adapt and survive under given conditions (Figure 1.6) (Shi et al., 2021). These adaptive responses are orchestrated primarily through the stabilization and activation of HIFs, which serve as the central transcriptional regulators under hypoxia (Bigos et al., 2024; Shi & Gilkes, 2025). Although many studies do not differentiate between individual HIF-α isoforms, it has become clear that HIF-1α, HIF-2α, and HIF-3α can have overlapping, distinct, or even antagonistic functions depending on cell type, tissue origin, and the duration and severity of hypoxia (Heikkilä et al., 2011; Ravenna et al., 2016).

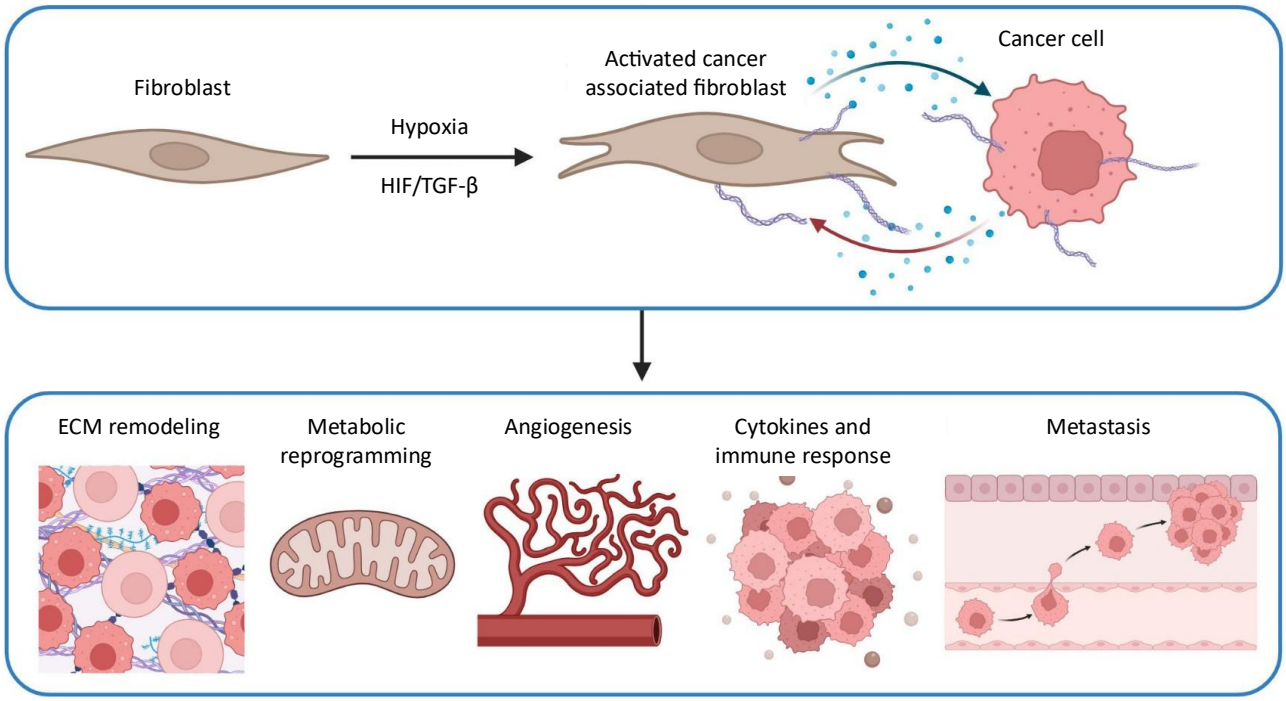

Figure 1.6 Cellular and microenvironmental adaptation to hypoxia. Fibroblasts are activated into CAFs by tumor-derived signals and hypoxia. CAFs promote tumor progression and metastasis by remodeling the ECM, promote metabolic reprogramming and angiogenesis, and modulate the immune response. The figure was adapted from Bigos et al. (2024).

Among HIFs, HIF-1α and HIF-2α are the best-characterized isoforms and are frequently co-expressed in hypoxic cells. While HIF-1α is predominantly stabilized during acute and severe hypoxia (from 0 % to 2 % O_2), HIF-2α becomes dominant under moderate hypoxia (from 2 % to 5 % O_2), where it drives long-term adaptations associated with tumor progression (Bigos et al., 2024).In

contrast to HIF-1α and HIF-2α, HIF-3α is the most structurally divergent isoform and remains less well characterized. It undergoes extensive alternative splicing, resulting in multiple transcript variants with variable domain composition and function (Heikkilä et al., 2011; Ravenna et al., 2016). Most HIF-3α isoforms lack a C-TAD and therefore do not activate classical HRE-driven transcription (Rankin & Giaccia, 2008). Instead, HIF-3α often acts as a dominant-negative regulator by binding HIF-1β or inhibiting HIF-1α and HIF-2α, thereby preventing their nuclear translocation and transcriptional activity (Rankin & Giaccia, 2008). Nonetheless, some HIF-3α variants have been shown to transcriptionally activate specific genes such as *GLUT1* in a context-dependent manner, particularly when HIF-1β is limiting (Heikkilä et al., 2011). Moreover, HIF-3α has been implicated in regulating apoptosis and modulating tumor progression, with certain isoforms promoting invasion and metastasis under hypoxic conditions (Ravenna et al., 2016; Zhou et al., 2018). The downstream effects of HIF activation can be broadly categorized into intracellular adaptations within tumor cells and microenvironmental remodeling within the TME.

Intracellular Adaptations

At the cellular level, one of the key adaptations to hypoxia is a metabolic shift from mitochondrial oxidative phosphorylation toward aerobic glycolysis, a process known as the Warburg effect (Warburg et al., 1927). This adaptation is predominantly mediated by HIF-1α, which drives the transcription of genes such as *GLUT1*, *LDHA*, and *CA9* to maintain ATP production and regulate intracellular pH under low-oxygen conditions (Bigos et al., 2024). The accumulation of lactate as a consequence of glycolytic reprogramming further acidifies the TME, thereby leading to extracellular changes that promote local invasion and immune evasion (Chen et al., 2023).

In addition to metabolic reprogramming, hypoxia induces phenotypic changes that promote tumor progression. HIFs, particularly HIF-1α and HIF-2α, drive the epithelial-to-mesenchymal transition (EMT) of cells by modulating the expression of TFs such as SNAI1, which in turn repress epithelial markers like E-cadherin and upregulate mesenchymal markers including N-cadherin and vimentin (Zhang et al., 2017; Shi et al., 2021). Consequently, cancer cells gain increased motility, invasiveness, and resistance to apoptosis, enabling them to detach from the primary tumor and migrate to distant sites (Shi et al., 2021).

Additionally, HIF-2α is implicated in the maintenance of a stem-like phenotype by promoting the expression of genes such as *POU5F1,* facilitating tumor aggressiveness and metastatic potential (Zhang et al., 2017). Divergent regulation of proliferative pathways further distinguishes HIF isoforms: while HIF-2α enhances c-Myc activity, promoting proliferation, HIF-1α inhibits c-Myc and induces G1 arrest (Loboda et al., 2010), highlighting the complex and isoform-specific differences of these isoforms.

Microenvironmental Consequences

Hypoxia not only has an intracellular effect, but also has a crucial influence on the TME. One of the primary consequences is the induction of angiogenesis, the formation of new blood vessels. This process is largely mediated by HIF-driven upregulation of vascular endothelial growth factors (Liao & Johnson, 2007). HIF-1α prominently induces *VEGFA* expression to stimulate new vessel formation (Liao & Johnson, 2007; Bigos et al., 2024). However, the resulting vasculature is often abnormal, structurally disorganized, functionally inefficient, and, as a result, insufficient to restore normal oxygen delivery (Bigos et al., 2024).

Simultaneously, hypoxia drives extensive ECM remodeling through HIF-regulated expression of matrix-modifying enzymes such as MMPs and LOX, facilitating collagen cross-linking and increasing ECM stiffness (Chen et al., 2023). The ECM in the TME is composed of a complex network of structural proteins, including collagens, fibronectin, and hyaluronan (Chen et al., 2023). Under hypoxic conditions, the production and cross-linking of these components are enhanced, resulting in a denser and stiffer ECM architecture (Chen et al., 2023). These structural changes not only enable local invasion but also reshape the biochemical landscape of the TME by releasing growth factors and cytokines that further activate pro-tumorigenic pathways such as angiogenesis and immune suppression (Shi et al., 2021).

A central feature of this hypoxia-altered TME is the activation and expansion of CAFs. Hypoxia activates fibroblasts into CAFs through HIF-mediated mechanisms and the induction of factors such as TGF-β (Chen et al., 2023). Activated CAFs contribute to tumor progression by enhancing ECM remodeling, promoting metabolic reprogramming, and releasing immunosuppressive cytokines, such as IL6, which inhibit anti-tumor immune responses (Chen et al., 2023). HIF-2α has been particularly implicated in driving CAF activation and the establishment of an immunosuppressive TME (Garcia et al., 2022).

1.3.4. HIF Signaling in PDAC

In PDAC, HIF signaling is activated early during tumorigenesis, with HIF-1α expression already detectable in low-grade PanINs, suggesting that hypoxia and its downstream mediators contribute to disease initiation and progression (Lee et al., 2016). In advanced disease stages, immunohistochemical analyses of human pancreatic cancer tissue have demonstrated the presence of all three major isoforms (Zhou et al., 2018). Notably, HIF-3α exhibited the highest expression levels and was predominantly localized in the cytoplasm (Zhou et al., 2018).

HIF-1α has been associated with both tumor-promoting and tumor-suppressive effects depending on the experimental context, a phenomenon often referred to as the hypoxia paradox. In pancreatic epithelial cells of a murine model, deletion of *HIF1A* was shown to promote progression of PanINs containing the $KRAS^{G12D}$ mutation and to increase cell proliferation, suggesting a protective

role of HIF-1α in early pancreatic tumorigenesis (Lee et al., 2016). Conversely, loss of *HIF1A* has been shown to facilitate p53 degradation, thereby promoting a more invasive and metastatic phenotype in both human and murine PDACs (Tiwari et al., 2020).

In contrast, HIF-2α is consistently associated with pro-oncogenic effects in PDAC. High expression of HIF-2α has been linked to EMT, increased proliferation, enhanced stemness, and poor clinical outcome (Zhang et al., 2017). HIF-2α contributes to EMT by activating β-catenin and inducing the expression of TFs such as *TWIST2*, thereby promoting the transition toward a mesenchymal phenotype (Zhang et al., 2017; Tao et al., 2021). *In vivo*, HIF-2α promotes tumor growth, and its expression correlates with high tumor grade and metastasis (Zhang et al., 2017). Furthermore, HIF-2α regulates *VEGF* and *MMP9* expression, promoting angiogenesis and matrix remodeling (Zhang et al., 2017). Importantly, cell-type-specific deletion experiments in murine models showed that stromal HIF-2α, but not HIF-1α, drives PDAC progression (Garcia et al., 2022).

Given the complexity of HIF signaling in PDAC, the MIA PaCa-2 cell line represents a relevant model to explore HIF isoform-specific functions under hypoxic conditions in pancreatic cancer. Exposure to low oxygen significantly enhances EMT, shown by strong Twist1 upregulation and increased migratory behavior (Salnikov et al., 2012). In addition, the presence of mutant p53 may amplify hypoxia-mediated EMT and stemness, possibly through cooperation with HIF-regulated pathways (Salnikov et al., 2012). Among the HIF isoforms, HIF-3α is markedly upregulated in MIA PaCa-2 under hypoxia, where it promotes invasion and migration via activation of the RhoC-ROCK1 signaling axis, underscoring its importance in cytoskeletal remodeling and metastatic potential (Zhou et al., 2018).

1.3.5. Clinical Implications and Therapeutic Targeting of HIF Pathways

The presence of hypoxia in PDAC and other solid tumors has significant clinical implications (Bigos et al., 2024). In PDAC specifically, severe and chronic hypoxia results from the dense desmoplastic stroma and poor vascularization, creating a highly hypoxic, chemoresistant TME (Bigos et al., 2024). In the context of radiotherapy, hypoxia significantly impairs treatment efficacy, as oxygen is a critical factor for generating ROS that mediate DNA damage and apoptosis (Rakotomalala et al., 2021). When tissue pO_2 drops below 20 mmHg, cells become resistant to radiation-induced damage, as the absence of molecular oxygen prevents the stabilization of radiation-induced DNA lesions (Bigos et al., 2024). Moreover, radiation itself can worsen hypoxia by damaging tumor-associated vasculature, thereby further reducing oxygen delivery and promoting HIF activation, angiogenesis, and tumor recurrence – an outcome frequently observed in PDAC following radiotherapy (Huang et al., 2023).

Hypoxia also contributes to chemotherapy resistance in PDAC through multiple mechanisms. The TME is often acidic due to enhanced glycolysis and lactate production, a condition that reduces

drug uptake, particularly for weak base drugs such as gemcitabine, a standard chemotherapeutic agent used in PDAC (Bigos et al., 2024). Reduced perfusion and the structurally abnormal vasculature typical of PDAC further impair drug delivery, contributing to the formation of a hypoxic and chemoresistant tumor core (Tao et al., 2021).

Given the central role of HIFs in driving therapy resistance and tumor progression, several hypoxia-targeted strategies have been developed. Direct HIF inhibitors block transcriptional activity, while indirect inhibitors interfere with HIF expression or stability (Huang & Zhou, 2020). Balzutifan, a selective HIF-2α inhibitor, and downstream effectors such as *CA9* are under investigation for their potential to enhance chemosensitivity, particularly to gemcitabine, by disrupting pH homeostasis (Tao et al., 2021). To improve drug delivery in hypoxic PDAC regions, hypoxia-responsive nanoparticles and vascular normalization strategies show promise in enhancing perfusion and immune infiltration (Tao et al., 2021). Additionally, hypoxia-activated prodrugs like tirapazamine aim to selectively induce cytotoxicity in low-oxygen environments (Bigos et al., 2024). Although adoption in clinical settings remains limited, combining hypoxia-targeted approaches with chemo- and radiotherapy holds promise for improving therapeutic outcomes in PDAC and other hypoxic malignancies (Tao et al., 2021).

1.4. Functional Genomics Through Gene Editing

1.4.1. CRISPR/Cas9-Mediated Gene Knockout

The CRISPR/Cas9 system is a powerful gene editing tool that enables targeted genome modifications through RNA-guided DNA cleavage. Originally derived from a bacterial adaptive immune system, the Type II CRISPR/Cas9 system naturally functions by using a sgRNA to direct the Cas9 endonuclease to foreign DNA, where it introduces double-strand breaks (DSBs) adjacent to protospacer adjacent motifs (PAMs) to defend against viral infection (Jinek et al., 2012; Makarova et al., 2015).

Based on this natural mechanism, CRISPR/Cas9 has been adapted for genome editing in mammalian cells (Figure 1.7). In this context, Cas9 is guided by a synthetic sgRNA to a specific genomic locus, where it introduces DSBs that are primarily repaired by the error-prone non-homologous end joining (NHEJ) pathway, often introducing small insertions or deletions that disrupt the coding sequence and cause frameshift mutations (Jinek et al., 2012). Alternatively, cells may employ homology-directed repair (HDR), a less frequent but precise mechanism that restores the DNA sequence using a homologous template (Mali et al., 2013).

Cas9 mediates targeted DNA cleavage through two nuclease domains, each of which cleaves one DNA strand at the target site (Jinek et al., 2012). Specific targeting is achieved through the sgRNA, which encodes a 20-nucleotide region complementary to the DNA sequence of interest,

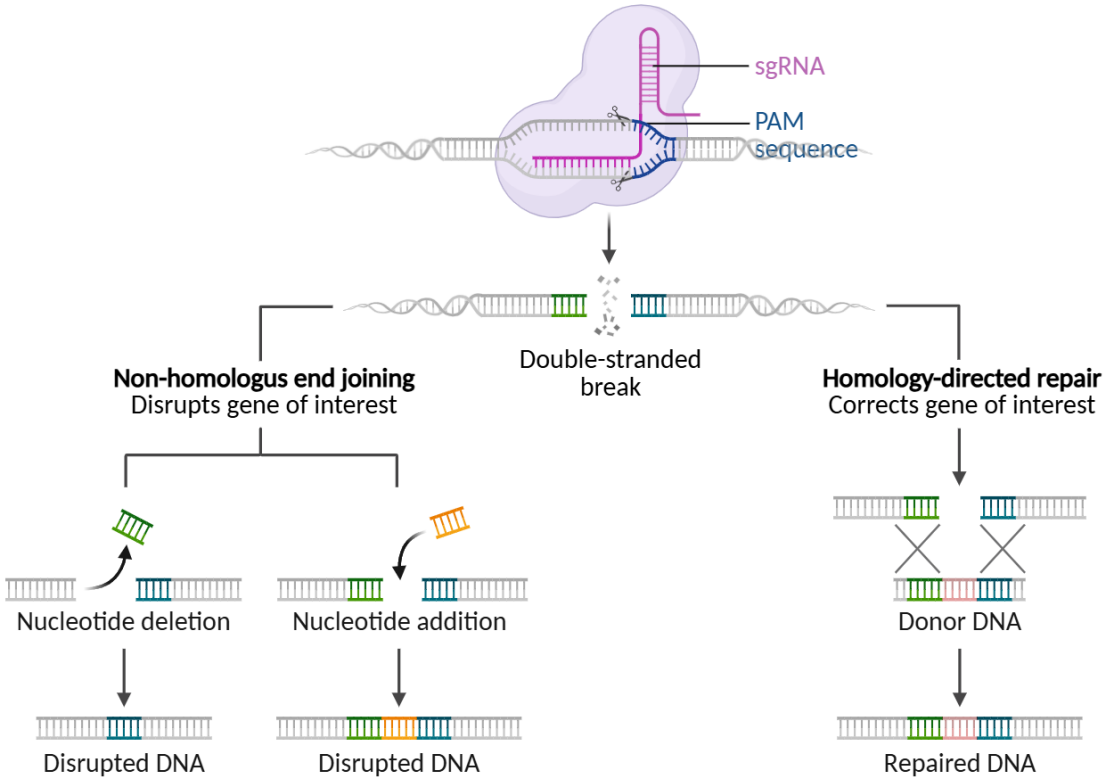

Figure 1.7 CRISPR/Cas9 mechanisms of knockout and knock-in. Cas9 induces DSBs mediated by sgRNA and PAM. Repair via NHEJ typically introduces disruptive insertions or deletions, leading to gene knockout, while HDR enables precise gene integration. The figure was created with Biorender.com.

located next to a required PAM site (Jinek et al., 2012). Additionally, sgRNAs are typically transcribed under the control of a U6 promoter in mammalian systems, as these RNA polymerase III promoters are well-suited for the robust expression of short RNA sequences such as sgRNAs (Mali et al., 2013). Beyond single-gene editing, the system‘s modular design enables multiplexed gene disruption by co-expressing multiple sgRNAs, allowing simultaneous knockout or editing of several genes in a single experiment (Cong et al., 2013; McCarty et al., 2020).

In pancreatic cancer research, CRISPR/Cas9 has been employed to study the function of individual genes involved in hypoxic signaling and tumor progression. Knockout studies have targeted various HIF-regulated genes such as *GLUT1*, revealing roles in angiogenesis, survival, and invasion (Yang et al., 2019). Although some knockout or knockdown studies have investigated potential roles of HIF isoforms individually, research remains limited, and comparative analyses between different HIF isoforms – especially to clarify the individual role of HIF-3α – are still needed to better understand their distinct contributions to hypoxia-driven tumor progression in PDAC.

1.4.2. Lentiviral Delivery for Stable Gene Editing

Lentiviral vectors, derived from HIV-1, are widely used for the stable delivery of genetic material into mammalian cells (Dong & Kantor, 2021). Their unique ability to transduce both dividing

and non-dividing cells, along with their capacity for genomic integration, makes them especially suitable for long-term gene expression studies, including CRISPR/Cas9-mediated editing (Elegheert et al., 2018; Dong & Kantor, 2021).

Structurally, lentiviral vector systems have evolved through multiple generations, each improving safety and efficiency. Among these, second-generation systems are most commonly used in research and are the focus of this section. Second-generation lentiviral systems are composed of three key components: a transfer vector carrying the construct of interest, a packaging plasmid encoding viral proteins such as Gag, Pol, Tat, and Rev, and an envelope plasmid, typically expressing VSV-G for broad host range tropism (Dong & Kantor, 2021). Gag encodes structural compartments, while Pol provides essential enzymatic functions, including reverse transcriptase, protease, and integrase, which are essential for viral replication and integration (Dong & Kantor, 2021).

Following transduction, the viral RNA genome is reverse-transcribed into double-stranded DNA (dsDNA) by the viral reverse transcriptase (Figure 1.8) (Dong & Kantor, 2021). This DNA is then transported into the nucleus via host-derived importins and nucleoporins – an ability that distinguishes lentiviruses from other retroviruses and allows efficient gene delivery even into non-dividing cells (Zhou et al., 2011; Dong & Kantor, 2021). Inside the nucleus, the viral integrase catalyzes the insertion of the proviral DNA into the host genome, resulting in stable integration (Elegheert et al., 2018). Additionally, the integrated provirus is transcribed by host polymerases, supporting the continuous production of the encoded elements (Dong & Kantor, 2021). Due to these properties, lentiviral systems are frequently used for CRISPR/Cas9 delivery, particularly in models requiring stable expression or involving hard-to-transfect cell types (Pirona et al., 2020).

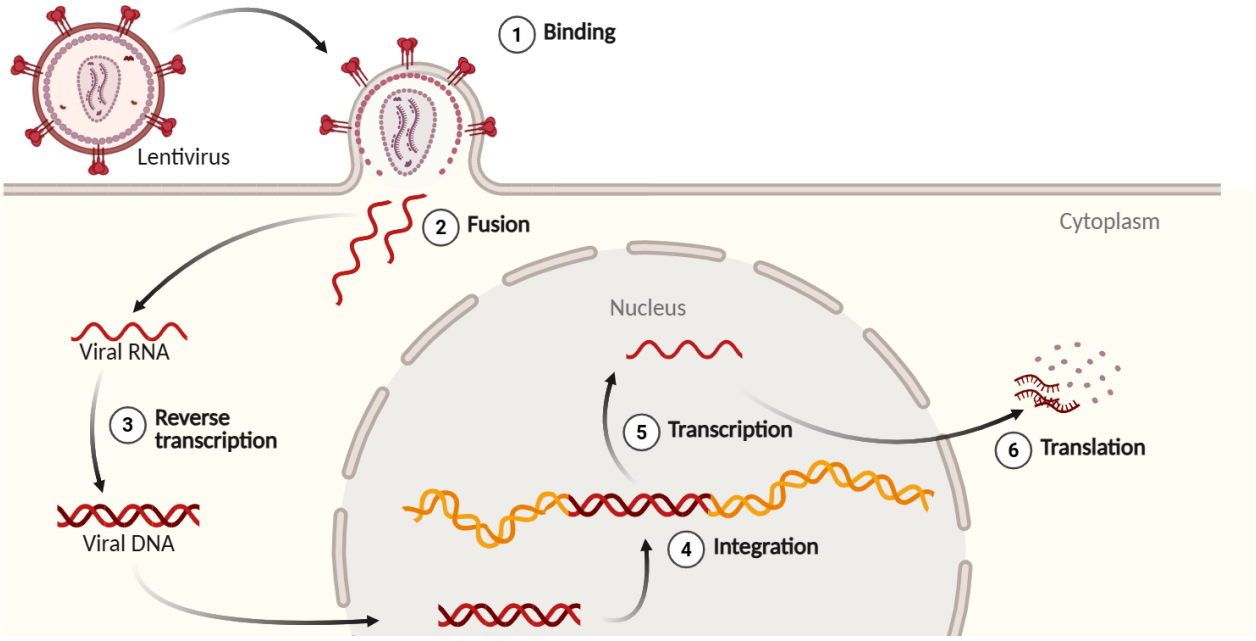

Figure 1.8 Schematic overview of lentivirus-mediated gene delivery. Lentiviral transduction through **(1)** receptor binding, **(2)** membrane fusion, **(3)** reverse transcription, **(4)** nuclear import and integration, **(5)** transcription, and **(6)** translation. The figure was created with Biorender.com.

1.4.3. The MuLE System for Multiplexed Knockouts

Knockout approaches have long been fundamental in functional genomics, enabling researchers to investigate gene functions by observing phenotypic consequences following gene disruption. However, many biological processes are controlled by complex networks rather than single genes acting in isolation. Consequently, single-gene knockouts often fail to capture functional redundancies, compensatory mechanisms, or regulatory interactions. To address these limitations, multiplexed gene knockout strategies have emerged as powerful tools to dissect gene interactions and functional dependencies within dynamic biological systems (McCarty et al., 2020; Fujii et al., 2023).

A central technical challenge in multiplexed genome editing is the coordinated expression of Cas9 and multiple sgRNAs within the same cell. The MuLE system addresses this by enabling the expression of several sgRNAs alongside Cas9 from a single lentiviral construct with high efficiency and directional specificity (Albers et al., 2015; Chee & Foan, 2015).

The MuLE workflow involves three main steps (Figure 1.9). First, individual elements such as sgRNAs, Cas9, fluorescent reporters, or antibiotic resistance markers are cloned into entry vectors via restriction enzyme-based cloning, typically using Type IIS enzymes (Albers et al., 2015) (Figure 1.9A). Each entry vector is flanked by specific attachment sites (*attL* and *attR*) that define the order and orientation of the inserts (Chee & Foan, 2015). Second, the selected entry vectors are combined into a lentiviral destination vector through the MultiSite Gateway LR recombination reaction (Albers et al., 2015) (Figure 1.9B). This site-specific recombination is catalyzed by a recombinase enzyme, which mediates recombination between *att* sites, enabling directional assembly of multiple inserts into a single construct with defined order and orientation (Albers et al., 2015; Chee & Foan, 2015). In the third step, the assembled MuLE construct serves as a transfer plasmid and is co-transfected with packaging and envelope plasmids into a producer cell line to generate lentiviral particles (Albers et al., 2015) (Figure 1.9C). These viral particles are harvested and used to transduce target cells (Albers et al., 2015). Following transduction, the lentiviral genome is stably integrated into the host cell's DNA, enabling persistent expression of Cas9 and multiple sgRNAs from the same vector system (Elegheert et al., 2018; Dong & Kantor, 2021). This stable integration is particularly advantageous for generating polyclonal or long-term knockout cell lines and has been successfully applied to achieve the simultaneous disruption of up to three genes in a single construct (Albers et al., 2015).

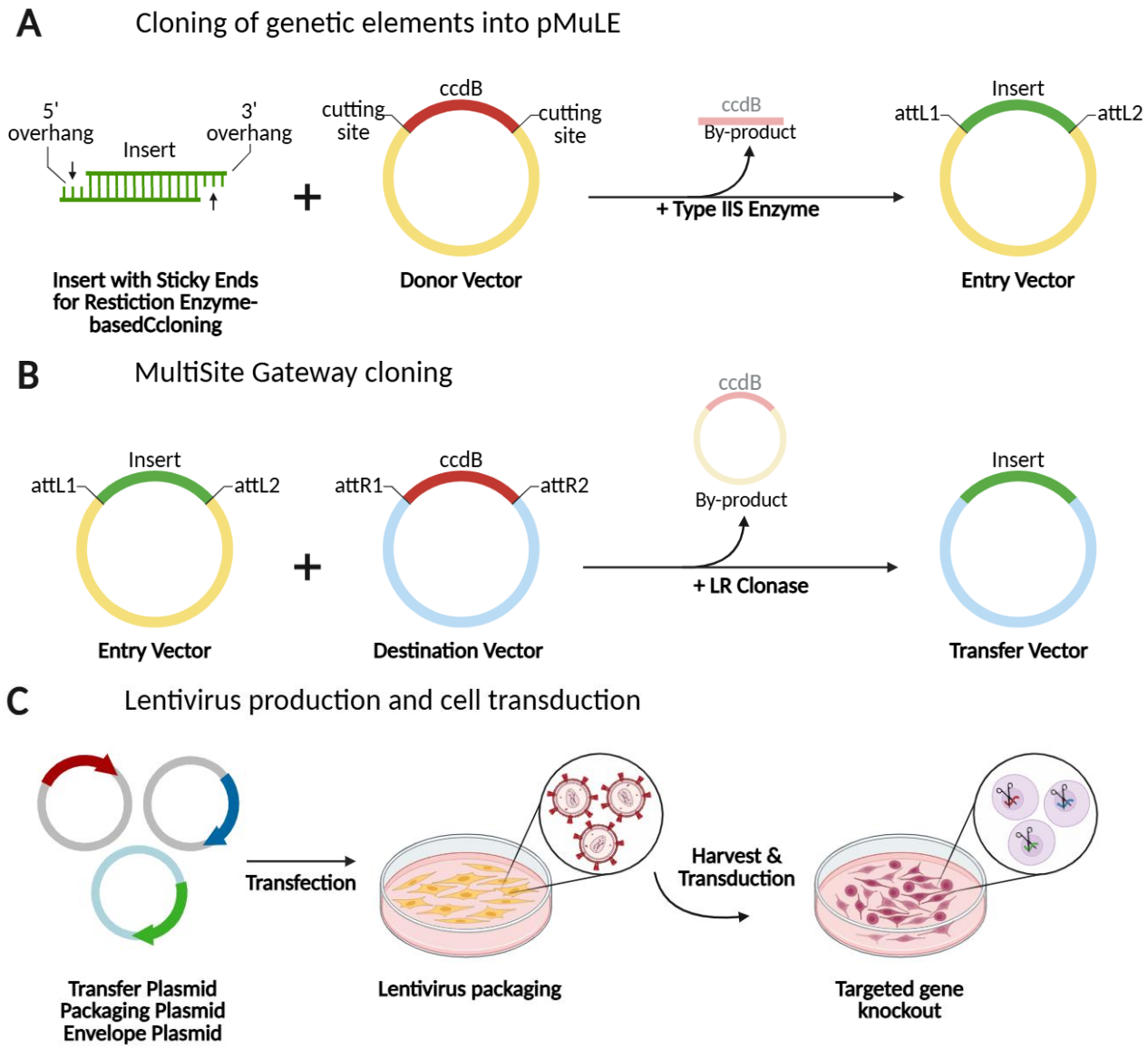

Figure 1.9 Overview of the MuLE system for multiplexed gene knockout. **(A)** Genetic elements are cloned into entry vectors via restriction enzyme-based cloning. **(B)** MultiSite Gateway recombination assembles multiple inserts into a transfer vector in defined order and orientation. **(C)** The transfer vector is packaged into lentiviral particles and used to transduce target cells, enabling stable integration and long-term expression. The figure was created with Biorender.com.

2. Materials and Methods

2.1. Materials

2.1.1. Reagents and Chemicals

Table 2.1 Reagents and chemicals used for this work and their manufacturers.

Manufacturer	Reagents
Abcam	CAY10585 – HIF-1α inhibitor #ab144422
Carl Roth	ampicillin sodium salt #K029; chloroform #6340.2; chloroquine diphosphate #C6628; geneticin disulfate #239.3; kanamycin #T832.1; sodium acetate trihydrate #6779.1; sodium dodecyl sulfate (SDS) #BP166-500; yeast extract #2904.2
Fisher BioReagents	agar #BO1423-500; glycerol #BP229-4; sodium chloride (NaCl) #BP358-212; sodium hydroxide (NaOH) #BP359-500; Tris-acetate-EDTA (TAE) #BP13332-4; Tris-EDTA buffer #BP2473-500
Gibco	Dulbecco‘s Modified Eagle Medium (DMEM) #11995065; Fetal Bovine Serum (FBS) #A5256801; Horse Serum (HS) #16050-122; Opti-MEM™ #31985-062; Penicillin-Streptomycin (PenStrep) #15140-122; Trypsin-EDTA #15400-054
Honeywell	ethanol #32221
Invitrogen	nuclease-free water #AM9937; SYBR™ Safe DNA Gel Stain #S33102; trypan blue #T10282
Thermo Scientific	agarose #R0492; chloramphenicol #10368030; crystal violet #C0775-25G; dimethyl sulfoxide (DMSO) #036480.AP; isopropanol #184130025; L-alanyl-L-glutamine #J66996.22; phosphate-buffered saline (PBS) #10010023; polybrene #TR-1003-G; polyethylenimine (PEI) #11460630/181978-5G; RNA Loading Dye #R0641; RNase AWAY™ #11580095; TriTrack DNA Loading Dye #R1161; tryptone #16279751; Virkon™ #12338667

2.1.2. Master Mixes and Commercial Kits

Table 2.2 Master mixes and commercial kits used for this work and their manufacturers.

Manufacturer	Master Mix/Commercial Kit
Invitrogen	SuperScript™ IV VILO™ Master Mix with ezDNase Enzyme #11766050
Qiagen	RNeasy Mini Kit #74104.00
Thermo Scientific	DreamTaq PCR Master Mix #K1081; GeneJET Gel Extraction Kit #K0831; GeneJET Plasmid Miniprep Kit #K0502; LR Clonase™ II Plus Enzyme Mix #12538120; PowerTrack™ SYBR™ Green Master Mix #MAN0018825

2.1.3. Enzymes and Molecular Size Standards

„FastDigest BamHI“ #FD0054, „FastDigest BveI“ #FD1744, „FastDigest EcoRI“ #FD0275, „FastDigest SmaI“ #FD0663, „FastDigest XhoI“ #FD0694, „Proteinase K“ #EO0491, „O‘GeneRuler DNA Ladder Mix“ #SM0331. All enzymes and molecular size standards were purchased from Thermo Scientific and used according to the manufacturer‘s recommendations.

2.1.4. Media and Buffers

Table 2.3 Media and buffers prepared in-house and their composition.

Name	Composition
Annealing buffer	50 mM NaCl in Tris-EDTA buffer
Complete medium for HEK293T/17 cells	10 % v/v FBS, 4mM L-alanyl-L-glutamine in DMEM
Complete medium for MIA PaCa-2 cells	10 % v/v FBS, 2.5 % HS, 4 mM L-alanyl-L-glutamine in DMEM
Freezing medium	5 % v/v DMSO in FBS
Growth medium for HEK293T/17 cells	10 % v/v FBS, 1 % v/v PenStrep in DMEM
Growth medium for MIA PaCa-2 cells	10 % v/v FBS, 2.5 % v/v HS, 1 % v/v PenStrep in DMEM
Luria-Bertani (LB) agar	2 % agar, 1 % NaCl, 1 % tryptone, 0.5 % yeast-extract in distilled water
LB broth	1 % NaCl, 1 % tryptone, 0.5 % yeast-extract in distilled water

2.1.5. Bacterial Strains and Mammalian Cell Lines

Table 2.4 Bacterial strains and mammalian cell lines used for research.

Name	Species/Tissue origin	Supplier
DH10B	*Escherichia coli*	*Escherichia coli* strain DH10B was obtained from Invitrogen.
HEK293T/17	*Homo sapiens*, embryonic kidney	HEK293T/17 cell line was a gift from Urte Neniškytė's lab and provided by Neringa Daugelavičienė.
MIA PaCa-2	*Homo sapiens,* pancreatic carcinoma	The MIA PaCa-2 cell line (human pancreatic carcinoma, ACC-733) was obtained from the German Collection of Microorganisms and Cell Cultures (DSMZ, Braunschweig, Germany).

2.1.6. Plasmids

Table 2.5 Plasmids used in this work and their specific features.

Plasmid Name	Vector Type	Manufacturer/Supplier
psPAX2	Second-generation lentiviral packaging plasmid providing *gag*, *pol*, *rev*, and *tat* genes necessary for virus particle assembly; confers ampicillin resistance.	Didier Trono; Addgene #12260
pMD2.G	Lentiviral envelope plasmid expressing VSV-G glycoprotein for broad tropism in target cells; confers ampicillin resistance.	Didier Trono; Addgene #12259
pMuLE ENTR U6 stuffer sgRNA scaffold L1-R5	MultiSite Gateway Donor vector containing a U6 promoter, stuffer sequence, and sgRNA scaffold flanked by *attL1* and *attR5* sites; confers kanamycin and chloramphenicol resistance.	Ian Frew; Addgene #1000000060
pMuLE ENTR U6 stuffer sgRNA scaffold L1-L4	MultiSite Gateway Donor vector containing a U6 promoter, stuffer sequence, and sgRNA scaffold flanked by *attL1* and *attL4* sites; confers kanamycin and chloramphenicol resistance.	Ian Frew; Addgene #1000000060
pMuLE ENTR U6 stuffer sgRNA scaffold L5-L4	MultiSite Gateway Donor vector containing a U6 promoter, stuffer sequence, and sgRNA scaffold flanked by *attL5* and *attL4* sites; confers kanamycin and chloramphenicol resistance.	Ian Frew; Addgene #1000000060
pMuLE ENTR U6 stuffer sgRNA scaffold R4-R3	MultiSite Gateway Donor vector containing a U6 promoter, stuffer sequence, and sgRNA scaffold flanked by *attR4* and *attR3* sites; confers kanamycin and chloramphenicol resistance.	Ian Frew; Addgene #1000000060
pMuLE ENTR SV40-hCas9 L3-L2	MultiSite Gateway Entry vector encoding SV40-driven human codon-optimized Cas9, flanked by *attL3* and *attL2* sites; confers kanamycin resistance.	Ian Frew; Addgene #1000000060
pMuLE ENTR SV40-hCas9 L5-L2	MultiSite Gateway Entry vector encoding SV40-driven human codon-optimized Cas9, flanked by *attL5* and *attL2* sites; confers kanamycin resistance.	Ian Frew; Addgene #1000000060
pMuLE Lenti Dest eGFP	MultiSite Gateway Destination vector carrying an eGFP reporter for fluorescent tracking of transduced cells and containing *attR1* and *attR2* sites; confers ampicillin and chloramphenicol resistance.	Ian Frew; Addgene #1000000060
pMuLE Lenti Dest Neo	MultiSite Gateway Destination vector carrying a neomycin (G418) resistance gene for stable selection of transduced cells and containing *attR1* and *attR2* sites; confers ampicillin and chloramphenicol resistance.	Ian Frew; Addgene #1000000060

Table 2.6 Recombinant plasmids constructed in-house in the work.

Plasmid Name	Description
pMuLE ENTR U6 HIF1A sgRNA L1-R5	MultiSite Gateway Entry vector expressing sgRNA targeting *HIF1A*, flanked by *attL1* and *attR5* sites; confers kanamycin resistance. Derived from pMuLE ENTR U6 stuffer sgRNA scaffold L1-R5.
pMuLE ENTR U6 HIF2A sgRNA L1-R5	MultiSite Gateway Entry vector expressing sgRNA targeting *HIF2A*, flanked by *attL1* and *attR5* sites; confers kanamycin resistance. Derived from pMuLE ENTR U6 stuffer sgRNA scaffold L1-R5.
pMuLE ENTR U6 HIF3A sgRNA L1-R5	MultiSite Gateway Entry vector expressing sgRNA targeting *HIF3A*, flanked by *attL1* and *attR5* sites; confers kanamycin resistance. Derived from pMuLE ENTR U6 stuffer sgRNA scaffold L1-R5.
pMuLE ENTR U6 scrambled sgRNA L1-R5	MultiSite Gateway Entry vector expressing scrambled sgRNA as a non-targeting control, flanked by *attL1* and *attR5* sites; confers kanamycin resistance. Derived from pMuLE ENTR U6 stuffer sgRNA scaffold L1-R5.
pMuLE ENTR U6 HIF1A sgRNA scaffold L1-L4	MultiSite Gateway Entry vector expressing sgRNA targeting *HIF1A*, flanked by *attL1* and *attL4* sites; confers kanamycin resistance. Derived from pMuLE ENTR U6 stuffer sgRNA scaffold L1-L4.
pMuLE ENTR U6 HIF2A sgRNA scaffold L1-L4	MultiSite Gateway Entry vector expressing sgRNA targeting *HIF2A*, flanked by *attL1* and *attL4* sites; confers kanamycin resistance. Derived from pMuLE ENTR U6 stuffer sgRNA scaffold L1-L4.
pMuLE ENTR U6 HIF2A sgRNA scaffold L5-L4	MultiSite Gateway Entry vector expressing sgRNA targeting *HIF2A*, flanked by *attL5* and *attL4* sites; confers kanamycin resistance. Derived from pMuLE ENTR U6 stuffer sgRNA scaffold L5-L4.
pMuLE ENTR U6 HIF2A sgRNA scaffold R4-R3	MultiSite Gateway Entry vector expressing sgRNA targeting *HIF2A*, flanked by *attR4* and *attR3* sites; confers kanamycin resistance. Derived from pMuLE ENTR U6 stuffer sgRNA scaffold R4-R3.
pMuLE ENTR U6 HIF3A sgRNA scaffold R4-R3	MultiSite Gateway Entry vector expressing sgRNA targeting *HIF3A*, flanked by *attR4* and *attR3* sites; confers kanamycin resistance. Derived from pMuLE ENTR U6 stuffer sgRNA scaffold R4-R3.
pMuLE Lenti U6 HIF1A sgRNA SV40-hCas9 eGFP	MultiSite Gateway Transfer vector for lentiviral production expressing sgRNA targeting *HIF1A* and SV40-driven human codon-optimized Cas9, with eGFP reporter; confers ampicillin resistance. Derived from pMuLE ENTR U6 HIF1A sgRNA L1-R5, pMuLE ENTR SV40-hCas9 L5-L2, and pMuLE Lenti Dest eGFP. Used for single-gene knockout of *HIF1A*.
pMuLE Lenti U6 HIF2A sgRNA SV40-hCas9 eGFP	MultiSite Gateway Transfer vector for lentiviral production expressing sgRNA targeting *HIF2A* and SV40-driven human codon-optimized Cas9, with eGFP reporter; confers ampicillin resistance. Derived from pMuLE ENTR U6 HIF2A sgRNA L1-R5, pMuLE ENTR SV40-hCas9 L5-L2, and pMuLE Lenti Dest eGFP. Used for single-gene knockout of *HIF2A*.
pMuLE Lenti U6 HIF3A sgRNA SV40-hCas9 Neo	MultiSite Gateway Transfer vector for lentiviral production expressing sgRNA targeting *HIF3A* and SV40-driven human codon-optimized Cas9, with neomycin (G418) reporter; confers ampicillin resistance. Derived from pMuLE ENTR U6 HIF3A sgRNA L1-R5, pMuLE ENTR SV40-hCas9 L5-L2, and pMuLE Lenti Dest Neo. Used for single-gene knockout of *HIF3A*.

2.1.7. Primers and Oligonucleotides

Table 2.7 Primers used for RT-qPCR during the work.

Name	Sequence (5‘–3‘)	Target	Product (bp)	Manufacturer
GAPDH_fw	TGGAGAAGGCTGGGGCTCATTT	*GAPDH*	162	Nanodiagnostika
GAPDH_rv	GTGCTAAGCAGTTGGTGGTGCA			Nanodiagnostika
GLUT1_fw	TTCACTGTCGTGTCGCTGTT	*GLUT1*	156	Eurofin Genomics
GLUT1_rv	GGCCACGAATGCTCAGATAGG			Eurofin Genomics
HIF1A_fw	GTATTGCACTGCACAGGCCACA	*HIF1A*	177	Nanodiagnostika
HIF1A_rv	ATCCAGGCTGTGTCGACTGAGG			Nanodiagnostika
HIF2A_fw	GACAAGGCCTCCATCATGCGAC	*HIF2A*	158	Nanodiagnostika
HIF2A_rv	TGGGTCACCACGGCAATGAAAC			Nanodiagnostika
HIF3A_fw	CATGCGCCTCACCATCAGCTAC	*HIF3A*	155	Nanodiagnostika
HIF3A_rv	CACCTTCCTCCTGGACAGGGTC			Nanodiagnostika
RHOC_fw	TTCAGCAAGGATCAGTTTCCGG	*RHOC*	129	Eurofin Genomics
RHOC_rv	ATCATAGTCTTCCTGCCCTGCT			Eurofin Genomics
VEGFA_fw	AAGGCCAGCACATAGGAGAGAT	*VEGFA*	125	Eurofin Genomics
VEGFA_rv	CTTTCGTTTTTGCCCCTTTCCC			Eurofin Genomics
VEGFC_fw	AGCTACCTCAGCAAGACGTTATTT	*VEGFC*	96	Eurofin Genomics
VEGFC_rv	TCGGCAGGAAGTGTGATTGG			Eurofin Genomics

Table 2.8 Oligonucleotides used in the work.

Name	Sequence (5‘–3‘)	Target	Manufacturer
HIF1a_p	ACCGGCTGTGATGAGGCTTACCATC	*HIF1A*	Nanodiagnostika
HIF1a_n	AAACGATGGTAAGCCTCATCACAGC		Nanodiagnostika
HIF2a_p	ACCGGCACAGTGTGAGCTCCCATCT	*HIF2A*	Nanodiagnostika
HIF2a_n	AAACAGATGGGAGCTCACACTGTGC		Nanodiagnostika
HIF3a_p	ACCGGAGGTGCTGTACCAGCTGGCT	*HIF3A*	Nanodiagnostika
HIF3a_n	AAACAGCCAGCTGGTACAGCACCTC		Nanodiagnostika
Scrambled_p	ACCGGCACTACCAGAGCTAACTCA	None	Nanodiagnostika
Scrambled_n	AAACTGAGTTAGCTCTGGTAGTGC		Nanodiagnostika

2.2. Methods

2.2.1. Bacterial Preparation and Transformation

Streaking and Cultivation of Bacteria from Stab Cultures

Plasmids were obtained as transformed bacteria in stab culture format. The bacterial stab was streaked onto LB agar plates and antibiotic selection was performed according to Table 2.5 by using either 100 µg/mL ampicillin or 50 µg/mL kanamycin. Plates were incubated overnight (from 12 hours to 18 hours) at 37 °C. On the next day, single colonies were collected from the plates and inoculated in LB medium including the same antibiotic and concentrations. Liquid cultures were incubated overnight (from 12 hours to 18 hours) at 37 °C while shaking at 250 rpm. Following incubation, a portion of the overnight culture was aliquoted and mixed with glycerol to a final concentration of 25 %, and used for long-term storage at –80 °C.

Preparation of Chemically Competent Cells

For preparation of chemically competent cells, a single colony of *E. coli* strain DH10B from a LB agar plate was used to inoculate 5 mL LB medium and grown overnight at 37 °C with shaking at 250 rpm. The next day, 100 µL of the overnight culture was used to inoculate 10 mL of LB medium, which was incubated at 37 °C with shaking at 250 rpm until the culture reached mid-logarithmic growth phase (OD_{600} = 0.5 to 0.7).

The culture was then chilled on ice and the cells were collected by centrifugation at 4 °C and 2000 × g for 10 minutes. The cell pellet was gently resuspended in a 1:2 ratio of chilled 0.01 M NaCl solution. After a second centrifugation step under the same condition, the cell pellet was resuspended in a 1:2 ratio of chilled 0.1 M $CaCl_2$ solution and incubated on ice for 30 minutes. Following a final centrifugation, the cells were resuspended in a 1:20 ratio of chilled 0.1 M $CaCl_2$ solution. Aliquots of 100 µL were prepared and either used directly for transformation or supplemented with glycerol to a final concentration of 25 % for long-term storage at –80 °C.

Chemical Transformation of Competent Cells

For each transformation, 100 µL of competent cells were gently mixed with 1 ng to 100 ng of plasmid DNA and incubated on ice for 30 minutes. Cells were then subjected to heat shock at 42 °C for 2 minutes and immediately returned to ice for 2 minutes. Recovery was done by adding LB medium in a 1:10 ratio, followed by incubation at 37 °C with shaking at 250 rpm for 30 minutes.

After recovery, transformed cells were collected by centrifugation at 6000 × g for 1 minute. 800 µL of the supernatant were removed, and the cell pellet was gently resuspended in the remaining medium before plating on LB agar plates containing the appropriate antibiotic for selection. Plates were incubated overnight at 37 °C, and colony growth was assessed the following day.

2.2.2. Plasmid Purification

Plasmid Extraction using Alkaline Lysis

From 1 mL liquid overnight culture, cells were pelleted by centrifugation for 1 minute at 10 000 × g, resuspended in 100 µL Tris-EDTA buffer, and lysed with 200 µL 0.1 M NaOH with 1 % SDS. After inverting the sample, 150 µL of 3 M sodium acetate at pH 7.0 was added, followed by the addition of 450 µL chloroform. The mixture was centrifuged at 14 000 × g for 10 minutes. From the upper phase containing plasmid DNA, 300 µL was transferred to a new tube, precipitated with 300 µL isopropanol, and centrifuged for 10 minutes at 14 000 × g. The DNA pellet was washed with 70 % ethanol, centrifuged 5 minutes at 14 000 × g, and air-dried for 30 minutes before resuspension in 20 µL nuclease-free water. Samples were stored at –20 °C.

Plasmid Extraction using Columns

Plasmid DNA was purified using the GeneJET Plasmid Miniprep Kit according to the manufacturer‘s recommendations. Before purification, the liquid overnight culture was centrifuged

at 3500 × g for 4 minutes, and the supernatant was removed. All following centrifugation steps were carried out at 14 000 × g at room temperature. Purified plasmids were stored at –20 °C.

Sample Purification from Agarose Gel

Following restriction digestion, DNA samples were separated by electrophoresis on 1 % agarose gels at 120 V for 40 minutes. Bands of interest were visualized under UV light, excised with a sterile scalpel, and transferred to a clean microcentrifuge tube. The DNA was then purified from the gel slices using the GeneJET Gel Extraction Kit according to the manufacturer‘s protocol. Samples were stored at –20 °C.

2.2.3. Concentration Measurement of Nucleic Acid Samples

Nucleic acid concentrations were measured using a NanoDrop One^{C} spectrophotometer. Blanking was performed with the same reagent used to elute the sample. For each measurement, 1 µL of sample was applied to the pedestal. Absorbance was recorded at 230 nm, 260 nm, and 280 nm to determine sample concentration as well as A_{260}/A_{280} and A_{260}/A_{280} purity ratios. All measurements were conducted at room temperature.

2.2.4. Nucleic Acid Analysis

Restriction Analysis

Diagnostic restriction digests were performed using FastDigest restriction enzymes. Each reaction was assembled in a total volume of 20 µL using the components indicated in Table 2.9 and incubated at 37 °C for 15 minutes without an additional inactivation step. Additional control reactions, including a mock digest and a water control, were included with each restriction digest.

Table 2.9 Reaction mixture for restriction digest using FastDigest restriction enzymes.

Component	Volume (µL)
10× FastDigest Green Buffer	2
Plasmid DNA	Varies (up to 1 µg)
FastDigest Restriction Enzyme	1
Nuclease-free water	To 20

Gel Electrophoresis

Gels were prepared by dissolving 1 % agarose in TAE buffer, followed by addition of 1× SYBR^{TM} Safe. After solidification, the gel was placed into the electrophoresis chamber and 10 µL of sample was loaded together with 2 µL of TriTrack loading dye, unless a dye was already present in the reaction. Samples were run alongside the O‘GeneRuler DNA Ladder Mix as a molecular weight standard and a water control. Electrophoresis was regularly carried out at 120 V for 40 minutes and DNA bands were visualized using a molecular imager (Bio-Rad, Universal Hood II) and analyzed with Image Lab^{TM} Software 6.1.

2.2.5. Plasmid Construction and Cloning Procedures

Cloning of sgRNA Sequences into MuLE Donor Vectors

Complementary oligonucleotides encoding sgRNAs targeting *HIF1A*, *HIF2A*, *HIF3A*, and a scrambled control were designed with sticky ends compatible with BveI-generated overhangs. Oligonucleotides were resuspended in annealing buffer at a concentration of 2 µg each, mixed in equal volumes to a final volume of 50 µL, and heated to 95 °C for 5 minutes. The mixture was allowed to cool gradually to room temperature over 45 minutes. Annealed products were diluted to a final concentration of 1 ng/µL with nuclease-free water for downstream ligation.

Annealed oligonucleotides were ligated into BveI-digested MuLE donor vectors using T4 DNA Ligase for restriction enzyme-based cloning. Ligation reactions were prepared according to Table 2.10 by using 100 ng of linear vector DNA. Reactions were incubated at 22 °C for 60 minutes to improve ligation efficiency. Up to 5 µL of the ligation mixture was used to transform 100 µL of chemically competent *E. coli* DH10B cells. Alongside the ligation reactions, transformation controls included an uncut vector to assess the viability of competent cells, and a digested vector without ligase to evaluate background colony formation resulting from undigested or self-ligated vector.

Table 2.10 Reaction mixture for ligation of annealed oligonucleotides into MuLE donor vectors.

Component	Volume (µL)
Linear vector DNA	Varies
Insert DNA	5:1 molar ratio over vector
10× T4 DNA Ligase Buffer	2
T4 DNA Ligase	0.2
Nuclease-free water	To 20

MultiSite Gateway Cloning

Multi-fragment recombination reactions were performed using the LR Clonase™ II Plus Enzyme Mix to recombine entry vectors into lentiviral destination vectors compatible with the MuLE system. Prior to recombination, the lentiviral destination vector was linearized using the SmaI restriction enzyme by incubating the reaction at 37 °C for 15 minutes, followed by heat inactivation at 85 °C for 5 minutes. For recombination, each reaction was assembled in a total volume of 8 µL containing 10 fmol of each entry vector and 20 fmol of the linearized destination vector. The reaction volume was adjusted with Tris-EDTA buffer. After mixing, 2 µL of LR Clonase™ II Plus Enzyme Mix was added and reactions were incubated at 25 °C for 16 hours. To terminate the reaction, 1 µL Proteinase K was added, followed by incubation at 37 °C for 10 minutes. The entire reaction volume was subsequently used to transform chemically competent *E. coli* DH10B cells.

2.2.6. Mammalian Cell Culture Handling

Thawing Cells from Cryogenic Storage

Mammalian cells were thawed from cryogenic storage by placing the cryovial in a 37 °C water bath until only a small ice crystal remained. The vial was disinfected with 70 % ethanol and opened under sterile conditions. Cells were transferred to 9 mL of pre-warmed growth medium and centrifuged at 1000 × g for 3 minutes at room temperature. After removal of the supernatant containing DMSO, the cell pellet was resuspended in fresh growth medium and seeded into a cell culture flask. Flasks were incubated at 37 °C in a humidified incubator with 5 % CO_2.

Passaging of Cells

Cells were passaged upon reaching from 70 % to 90 % confluency. Culture medium, PBS and Trypsin-EDTA were prewarmed to 37 °C. In a biosafety cabinet, the spent medium was aspirated, and cells were washed with PBS. Trypsin-EDTA (1×) was added to cover the cell layer, and cells were incubated at 37 °C for approximately 3 minutes until detachment was observed. Trypsinization was neutralized with an equal amount of growth medium, and cells were resuspended by pipetting. The suspension was transferred to a 15 mL conical tube and centrifuged at 1000 × g for 3 minutes. After removal of the supernatant, the cell pellet was resuspended in fresh growth medium.

For cell counting, 10 µL of the cell suspension was mixed with 10 µL of trypan blue, and 10 µL of the mixture was loaded onto a counting slide and analyzed using an automated cell counter (Countess 3, Invitrogen). The number of viable and dead cells was determined, and the appropriate number of viable cells was calculated for seeding. Cells were diluted accordingly in fresh pre-warmed growth medium and seeded into a new cell culture flask at a split ratio of 1:4 to 1:8 for HEK293T/17 cells or 1:3 to 1:8 for MIA PaCa-2 cells. Culture flasks were gently swirled to distribute cells evenly and returned to a humidified incubator at 37 °C with 5 % CO_2.

Cryopreservation of Cells

Cells were prepared for cryopreservation following the same procedure as described for passaging, including detachment with Trypsin-EDTA, neutralization with growth medium, centrifugation, and resuspension in fresh medium. After cell detachment, viability and total cell number were determined.

Cells were then centrifuged again and resuspended in pre-cooled freezing medium at a final concentration of around 2×10^6 viable cells/mL. Aliquots of 1 mL cell suspension were transferred into cryovials, placed in a pre-cooled isopropanol freezing container, and stored at –70 °C for around 24 hours, before transferring frozen vials to liquid nitrogen for long-term storage.

2.2.7. Lentiviral Vector Production and Transduction

Lentiviral Production in HEK293T/17 Cells

Lentiviral particles were produced by transfection of HEK293T/17 cells using PEI as transfection reagent. One day prior to transfection, cells were seeded at a density of 2.2×10^6 cells per 6 cm dish in complete medium and incubated overnight at 37 °C with 5 % CO_2. For packaging, the plasmids psPAX2, pMD2.G, and a pMuLE transfer plasmid were combined in Opti-MEM™ to a final volume of 300 µL per 6 cm dish according to Table 2.11. In parallel, PEI was diluted in Opti-MEM™ to achieve a DNA:PEI ratio of 1:4 in a total volume of 300 µL per 6 cm dish. The PEI solution was added dropwise to the DNA mixture while gently flicking the tube, and the mixture was incubated for 15 minutes at room temperature. During this incubation period, 25 µM chloroquine diphosphate was added to the cell culture medium. After incubation, the DNA mixture was added dropwise to the cells without disturbing the monolayer. Cells were incubated at 37 °C with 5 % CO_2 for 18 hours, before the transfection medium was replaced with fresh complete medium. Cells were cultured for an additional 48 hours before harvesting the supernatant containing the virus. Viral media was centrifuged at 2100 × g for 5 minutes at room temperature and filtered through a 0.45 µm polyethersulfone filter. Filtered virus was aliquoted and stored at –80 °C.

Table 2.11 Amount of each plasmid used for lentiviral packaging. Volumes are given for a single transfection reaction corresponding to one 6 cm dish.

Component	Volume (pmol)
psPAX2	0.78
pMD2.G	0.432
pMuLE Transfer Plasmid	0.984

General Transduction Procedure

To determine the functional titer of lentiviral preparations in MIA PaCa-2 cells, two complementary strategies were employed: (1) fluorescence-based detection of reporter gene expression, and (2) colony formation following antibiotic selection. One day prior to transduction, 75 000 MIA PaCa-2 cells were seeded per well of 6-well plates and incubated overnight at 37 °C with 5 % CO_2 and 21 % O_2. On the following day, thawed lentiviral supernatant was serially diluted in complete medium containing 10 µg/mL polybrene according to Table 2.12. After aspirating the old medium, 1.5 mL of the viral dilution was added to each well. One well was left untransduced to serve as a negative control. A parallel well was used to determine the number of transduced cells. Plates were incubated under standard conditions overnight. At 18 hours post-transduction, the viral supernatant was replaced with 2 mL fresh complete medium, and incubation was continued.

Table 2.12 Serial dilutions of lentiviral supernatant used for transduction of MIA PaCa-2 cells.

Dilution (Ratio)	Dilution (Factor)	Virus Volume (µL)	Media Volume (µL)
1:1	10^{0}	825	825
1:10	10^{-1}	150	1500
1:25	4×10^{-2}	60	1440
1:50	2×10^{-2}	30	1470
1:100	10^{-2}	150 (from 10^{-1})	1500
1:1000	10^{-3}	150 (from 10^{-2})	1500
1:10 000	10^{-4}	150 (from 10^{-3})	1500
1:100 000	10^{-5}	150 (from 10^{-4})	1500
1:1 000 000	10^{-6}	150 (from 10^{-5})	1500

Fluorescence-Based Titering

At 72 hours post-transduction, fluorescent reporter expression was assessed using an inverted fluorescence microscope (OlympusIX83) together with the cellSens Dimension software. Quantification of fluorescent cells was performed using Fiji (ImageJ, version 1.54p). Background substraction and uniform adjustment of brightness and contrast were applied to all images, and a binary mask was generated to calculate the percentage of fluorescent cells. Identical analysis parameters were used for all images within an experiment to ensure consistency. Only wells with ≤ 40 % fluorescent cells were included in the quantification to minimize overlapping signals and ensure accuracy.

The functional titer, expressed in transduction units per milliliter (TU/mL), and the Multiplicity of Infection (MOI), defined as the average number of viral particles per cell, were calculated using the following formulas:

$$\text{Titer}\left(\frac{\text{TU}}{\text{mL}}\right) = \frac{N \times F \times D}{V_T} \qquad \text{and} \qquad \text{MOI} = \frac{\text{Titer}\left(\frac{\text{TU}}{\text{mL}}\right) \times V_T}{N}$$

Where N is the number of cells at the time of transduction, F is the fraction of fluorescent cells, D is the dilution factor, and V_T is the transduction volume in mL.

Antibiotic Selection-Based Titering

A parallel strategy assessed the functional titer of virus encoding antibiotic resistance to geneticin (G418). Prior to the assay, the minimal lethal concentration was empirically determined by treating untransduced MIA PaCa-2 cells with antibiotic concentrations from 50 µg/mL to 1000 µg/mL. Accordingly, 800 µg/mL G418 was used, allowing colony formation in transduced wells while causing complete death in the untransduced control. During selection, the medium was replaced every four days. After successful selection, wells were washed with PBS and stained using 0.1 % crystal violet solution for 10 minutes at room temperature. Excess dye was removed by three PBS washes, and resistant colonies were manually counted in wells displaying discrete, non-overlapping foci. Functional titers and MOI were calculated using the following formulas:

$$\text{Titer}\left(\frac{\text{TU}}{\text{mL}}\right) = \frac{C}{V} \times D \qquad \text{and} \qquad \text{MOI} = \frac{\text{Titer}\left(\frac{\text{TU}}{\text{mL}}\right) \times V_T}{N}$$

Where C is the number of colonies, V is the volume of media in the well given in mL, D is the lentiviral dilution factor, N is the number of cells at the time of transduction, and V_T is the transduction volume in mL.

2.2.8. Hypoxic Treatment and HIF-1α Inhibition in MIA PaCa-2 Cells

MIA PaCa-2 cells were seeded in 6-well plates and incubated under normoxic conditions (21 % O_2, 5 % CO_2) until reaching 60 % confluence. Cells were then transferred to a hypoxia chamber (1 % O_2, 5 % CO_2) for defined durations of 5 hours, 12 hours, and 24 hours. Additionally, the same number of cultures was pre-treated with 10 µM CAY10585 HIF-1α inhibitor. Following treatment, cells were placed in the hypoxia chamber and incubated at the same time intervals as untreated hypoxic controls. A parallel control was cultured under normoxic conditions. After incubation, cells were immediately lysed and RNA was extracted.

2.2.9. Gene Expression Analysis

RNA Purification using Columns

Total RNA was extracted from MIA PaCa-2 cells using the RNeasy Mini Kit. Cells were harvested by direct lysis in the culture well. The lysate was homogenized by passing through a blunt 20-gauge needle attached to a RNase-free syringe. To increase the final RNA concentration, the eluate obtained after the first elution with 50 µL RNase-free water was reapplied onto the same column and eluted again under identical conditions. The purified RNA was stored at –80 °C.

Complementary DNA (cDNA) Synthesis

cDNA was synthesized from total RNA using the SuperScript™ IV VILO™ Master Mix with ezDNase Enzyme, according to the manufacturer‘s protocol. All steps were performed on ice. Per 20 µL reaction, 1 µg of RNA was used and a no-reverse transcription (no-RT) control was prepared (Table 2.13). Resulting cDNA was stored at –20 °C.

Table 2.13 Reaction components for genomic DNA digestion and cDNA synthesis using the SuperScript™ IV VILO™ Master Mix.

Genomic DNA Digestion		**cDNA Synthesis**	
Component	**Volume (µL)**	**Component**	**Volume (µL)**
10X ezDNase Buffer	1	SuperScript™ IV VILO™ Master Mix	4
ezDNase Enzyme	1		
Template RNA	Varies (1 µg)	Nuclease-free water	6
Nuclease-free water	To 10		

Real-Time Quantitative PCR (RT-qPCR) for Gene Expression Analysis

RT-qPCR was performed using the PowerTrack™ SYBR™ Green Master Mix following the manufacturer‘s recommendations (Table 2.14). Amplification reactions were prepared on ice in a total

volume of 10 µL and by using 10 ng of cDNA per reaction. Reaction mixtures were loaded into a 96-well optical PCR plate, sealed with optical adhesive film, and RT-qPCR was conducted using the standard cycling mode. Data were generated using the StepOne Plus Real-Time PCR System (Applied Biosystems). All reactions were set up in technical duplicates, and no-template controls (NTCs) as well as no-RT control samples were included for each experimental setup.

Table 2.14 Reaction mixture and thermal cycling conditions used for RT-qPCR.

RT-qPCR Rection Mixture		**Cycler Program**			
Component	**Volume (µL)**	**Step**	**Temperature (°C)**	**Time (s)**	**Cycles**
cDNA template (10 ng/µL)	1	Enzyme activation	95	120	1
Yellow Sample Buffer	0.5	Denature	95	15	40
PowerTrack™ SYBR™ Green Master Mix	10	Anneal/Extend	60	60	
Primers (8 µM)	1				
Nuclease-free water	7.5				

2.2.10. Statistical Analysis

Quantification of fluorescent cells from microscopy images was performed as descibed in Section 2.2.7. Statistical comparisons between lentiviral dilutions were performed using pairwise two-tailed t-tests, and significance was indicated as follows: *** $p < 0.001$, ** $p < 0.01$, * $p < 0.05$, ns (not significant, $p > 0.05$).

Relative gene expression analysis from RT-qPCR data was carried out as detailed in Section 2.2.9. Amplification plots and quantification cycle (Cq) values were analyzed using StepOne Software v2.3, together with Microsoft Excel and R software version 4.4.3. Relative gene expression was calculated using the ΔΔCq method, with normalization to the GAPDH housekeeping gene and the normoxia control condition.

All graphs were generated with R software version 4.4.3. Unless otherwise stated, all data are presented as mean values, with error bars representing the standard deviation of biological replicates.

3. Results

3.1. Preparation and Validation of Plasmid Constructs

3.1.1. Selection of Plasmids for MultiSite Gateway Cloning

To generate single-, double-, and triple-knockout constructs containing one, two, or three sgRNAs together with Cas9 within the MuLE system, suitable donor, entry, and destination vectors were selected from the MuLE system kit comprising 96 plasmids (Figure 3.1). Vectors were selected based on the presence of complementary *attL/R* recombination sites to enable directional and compatible multi-fragment assembly via the MultiSite Gateway reaction.

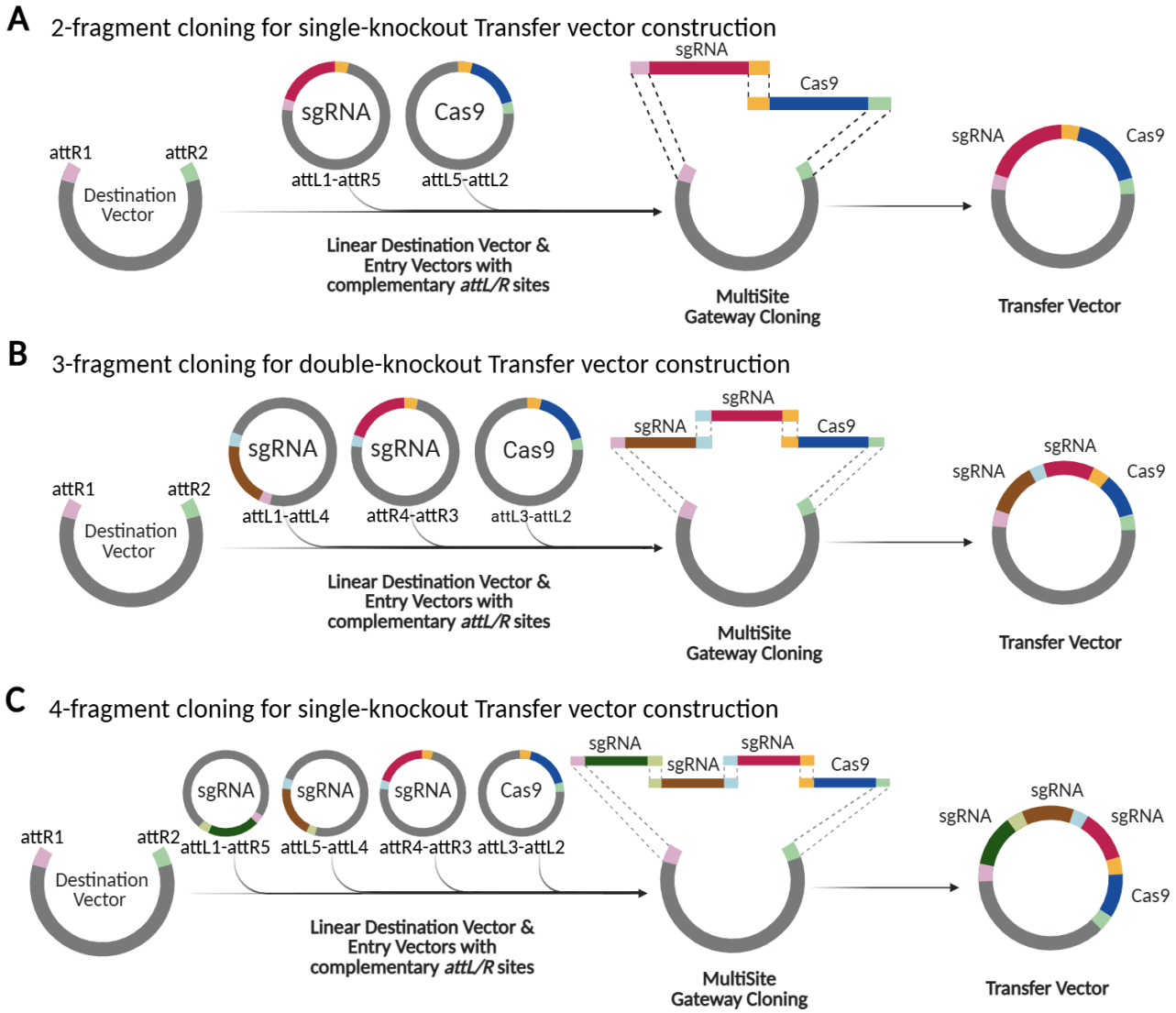

Figure 3.1 Schematic overview of donor, entry, and destination vector selection for MultiSite Gateway cloning within the MuLE system. Constructs were designed based on compatible *attL/R* recombination sites to enable directional assembly of single-knockout **(A)**, double-knockout **(B)**, and triple-knockout **(C)** vectors. The figure was created with Biorender.com.

For single-knockout constructs, pMuLE ENTR U6 stuffer sgRNA scaffold L1-R5 was selected as the donor vector, to be combined with pMuLE ENTR SV40-hCas9 L5-L2, an entry vector expressing SV40-driven hCas9, and inserted into either pMuLE Lenti Dest eGFP (containing an eGFP

marker) or pMuLE Lenti Dest Neo (containing a neomycin resistance gene) (Figure 3.1A). For double-knockout constructs, pMuLE ENTR U6 stuffer sgRNA scaffold L1-L4 and pMuLE ENTR U6 stuffer sgRNA scaffold R4-R3 were selected as donor vectors, to be combined with pMuLE ENTR SV40-hCas9 L3-L2 and recombined into one of the destination vectors (Figure 3.1B). For triple-knockout constructs, pMuLE ENTR U6 stuffer sgRNA scaffold L1-R5, pMuLE ENTR U6 stuffer sgRNA scaffold L5-L4, and pMuLE ENTR U6 stuffer sgRNA scaffold R4-R3 were combined with pMuLE ENTR SV40-hCas9 L3-L2 and one of the destination vectors (Figure 3.1C).

3.1.2. Purification and Verification of Plasmid Constructs

Plasmid preparations were subjected to diagnostic restriction digestion and agarose gel electrophoresis to verify identity and structural integrity (Figure 3.2). During the screening process, multiple bacterial colonies were analyzed for each plasmid. Some clones were excluded due to the presence of unexpected or missing fragments, indicating incomplete or incorrect plasmids. The plasmids that displayed restriction patterns corresponding to the expected fragment sizes (Table 3.1) were selected.

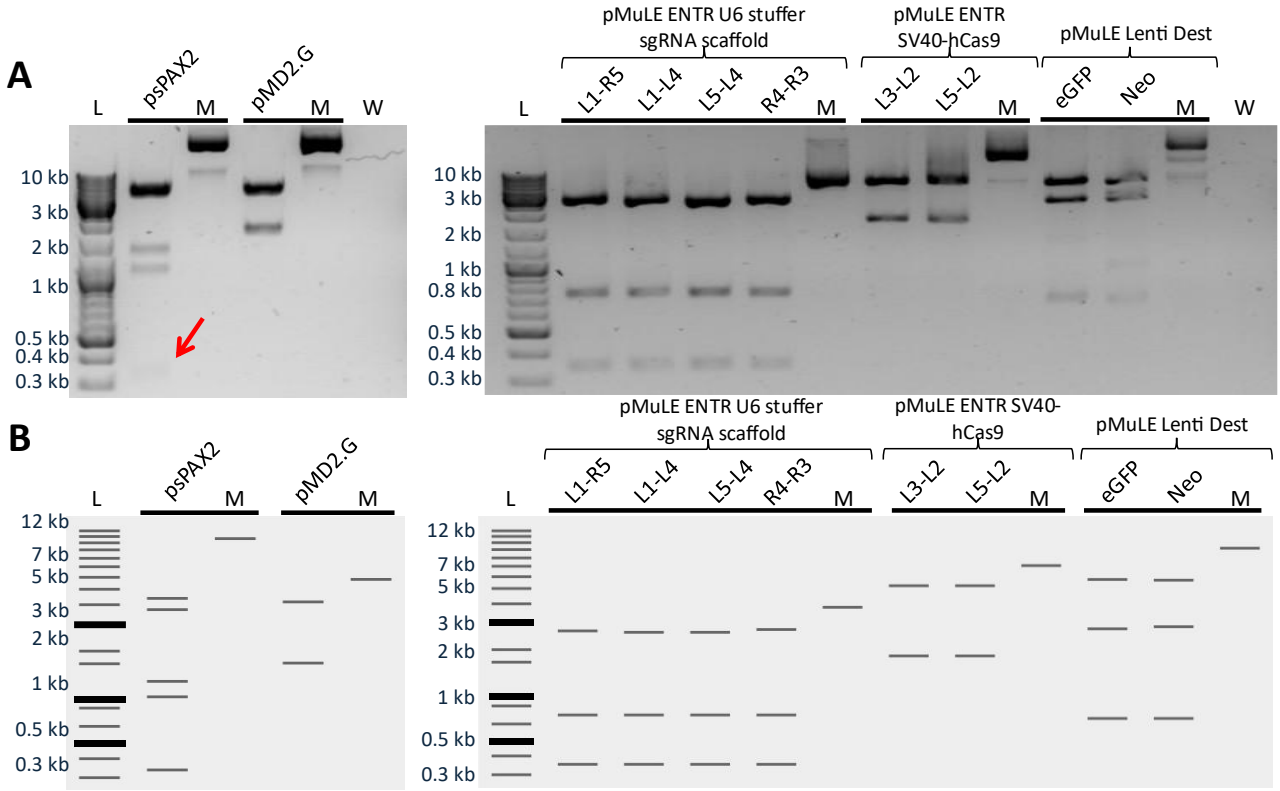

Figure 3.2 Verification of plasmid identity by diagnostic restriction digest. **(A)** Representative gel images of plasmids digested with FastDigest restriction enzymes, separated on a 1 % agarose gel stained with SYBR Safe. The gel was run at 120 V for 40 minutes. The red arrow indicates the shortest band of sample psPAX2. **(B)** Simulated restriction digest of corresponding plasmids, indicating expected fragment sizes. The figure was generated using Benchling.com. L – molecular weight ladder; M – mock digest (no restriction enzyme); W – water control.

Table 3.1 Plasmids analyzed by diagnostic restriction digest with applied restriction enzyme combinations and the corresponding expected fragment sizes for verification by agarose gel electrophoresis.

Plasmid	Restriction Enzymes	Expected Fragment Sizes (bp)
psPAX2	BamHI, EcoRI	4370, 3720, 1273, 1009, 337
pMD2.G	EcoRI	4154, 1668
pMuLE ENTR U6 stuffer sgRNA scaffold L1-R5	EcoRI, XhoI	2634, 739, 352
pMuLE ENTR U6 stuffer sgRNA scaffold L1-L4	EcoRI, XhoI	2585, 739, 352
pMuLE ENTR U6 stuffer sgRNA scaffold L5-L4	EcoRI, XhoI	2682, 739, 352
pMuLE ENTR U6 stuffer sgRNA scaffold R4-R3	EcoRI, XhoI	2692, 739, 352
pMuLE ENTR SV40-hCas9 L3-L2	BamHI, EcoRI	5252, 1817
pMuLE ENTR SV40-hCas9 L5-L2	BamHI, EcoRI	5256, 1817
pMuLE Lenti Dest eGFP	BamHI, XhoI	5734, 2734, 703
pMuLE Lenti Dest Neo	BamHI, XhoI	5721, 2813, 703

3.2. Generation of sgRNA Entry Vectors by Restriction Enzyme-based Cloning

3.2.1. Design and Cloning of sgRNA Sequences into Entry Vectors

To assemble single and multiplexed CRISPR/Cas9 constructs, sgRNA target sequences within exon 2 of *HIF1A*, *HIF2A*, and *HIF3A* were designed for high on-target activity and minimal off-target effects. A 5‘ guanine was added to enhance U6 promoter-driven transcription. In addition to the gene-specific guides, a scrambled sgRNA sequence with no predicted target site in the human genome was included as a non-targeting control, following the approach previously described by Cuesta-Borràs et al. (2023). All oligonucleotide pairs were synthesized with overhangs compatible with BveI-generated ends for directional cloning.

Selected pMuLE U6 stuffer donor vectors with varying recombination sites were linearized by BveI digestion, excising a 739 bp fragment containing the chloramphenicol resistance cassette and an incorporated EcoRI restriction site. The linearized backbones of around 3000 bp were separated by gel electrophoresis and purified by gel purification. Through cloning of sgRNA into this backbone, a total of nine distinct sgRNA entry vectors were generated to accommodate all combinations required for two-fragment, three-fragment, and four-fragment MultiSite Gateway recombination reactions. Representative images show the cloning of *HIF2A*-targeting sgRNA into the linearized backbone of pMuLE ENTR U6 stuffer sgRNA scaffold L1-L4 (Figure 3.3). The transformation plate (Figure 3.3A) represents the experimental condition including all components. A high number of colonies was observed, indicating both efficient transformation and good viability of the competent cells. The positive control (Figure 3.3B) consisted of transformation with an uncut donor vector, which had not been digested with BveI and therefore lacked the insert. As expected, colonies were observed, confirming the viability of competent cells. However, the number of colonies was lower compared to

the experimental condition, which may be attributed to minor batch-to-batch variability in the preparation of competent cells. Importantly, the colony number remained sufficient to validate the functionality of the transformation. The negative control (Figure 3.3C), which used the same reaction mixture as the experimental condition but without ligase, served to assess background colony formation from undigested or self-ligated vector. Only a small number of colonies was detected, indicating that self-ligation without ligase was minimal and that the majority of colonies observed on the experimental plate were likely due to successful integration of the sgRNA into the donor vector backbone.

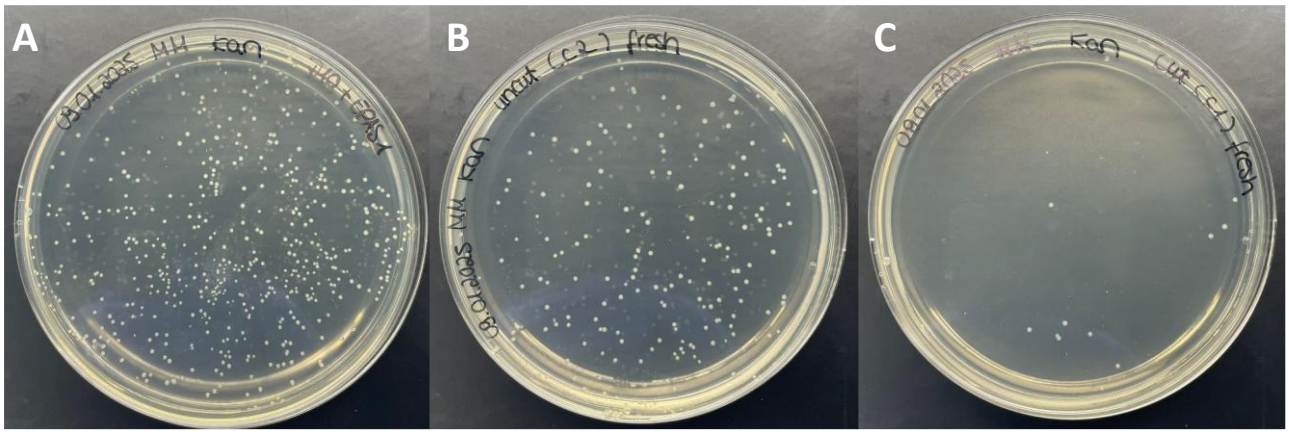

Figure 3.3 Representative LB agar plates following transformation of *E. coli* DH10B with BveI-digested pMuLE ENTR U6 stuffer sgRNA scaffold L1-L4 and the *HIF2A*-targeting sgRNA insert. **(A)** Experimental transformation using ligation of the linearized donor vector with annealed *HIF2A* sgRNA oligonucleotides. **(B)** Positive control using the uncut donor vector to verify competent cell viability and confirm antibiotic resistance. **(C)** Negative control using BveI-digested donor vector without ligase to assess background colony formation due to undigested or self-ligated donor plasmid.

3.2.2. Selection and Verification of Positive Clones

To confirm successful sgRNA insertion, transformed colonies were subjected to dual antibiotic replica plating. In this approach, single colonies were transferred onto two selective plates containing either kanamycin alone or a combination of kanamycin and chloramphenicol to differentiate between correctly modified and background clones. Colonies with correctly ligated sgRNA sequences lost the chloramphenicol cassette during BveI digestion and were expected to grow only on kanamycin plates, whereas background colonies or self-ligated plasmids would grow on both media. Candidate colonies were subsequently cultured, and plasmid DNA was isolated for additional verification by diagnostic restriction digestion using EcoRI and XhoI. Successful insertion of sgRNA resulted in excision of the chloramphenicol cassette, which also removed one of the EcoRI restriction sites, yielding two fragments in correctly modified vectors, compared to three fragments in unmodified donor vectors.

A representative agarose gel showing five entry vectors with sgRNA insertion and an unmodified donor vector is presented in Figure 3.4. entry vectors containing the sgRNA insert exhibited two bands of approximately 2.6 kb and 370 bp, respectively. In contrast, the unmodified donor vector showed three distinct fragments due to the retention of the chloramphenicol gene and

its associated EcoRI site. All nine generated sgRNA entry vectors were confirmed and subsequently used for the assembly of transfer vector constructs.

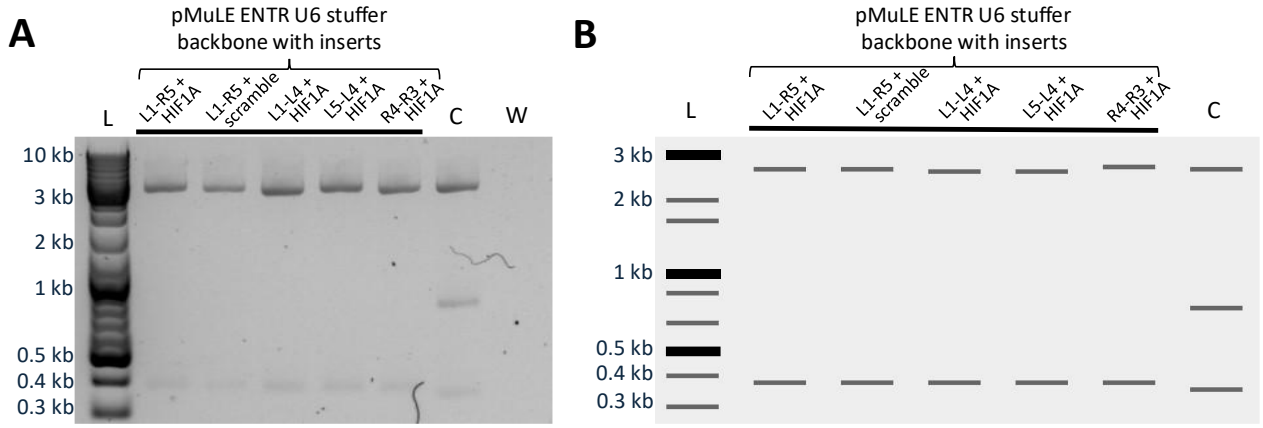

Figure 3.4 Verification of sgRNA entry vectors by diagnostic restriction digest. **(A)** Representative gel images of EcoRI/XhoI-digested sgRNA entry vectors separated on a 1 % agarose gel stained with SYBR Safe. The gel was run at 120 V for 40 minutes. **(B)** Simulated restriction digest of the corresponding vectors, indicating expected fragment sizes. The figure was generated using Benchling.com. L – molecular weight ladder; C – control vector (pMuLE ENTR U6 stuffer sgRNA scaffold without insert); W – water control.

3.3. Assembly of Lentiviral Transfer Vectors via MultiSite Gateway Cloning

3.3.1. Assembly of Single Knockout Transfer Vectors

While the overall aim of the project was the generation of multiplexed knockouts of *HIF1A*, *HIF2A*, and *HIF3A*, at this stage the focus was intentionally shifted to the assembly and validation of single-knockout vectors to first evaluate system functionality and efficiency under controlled conditions. Lentiviral transfer vectors for single-knockouts were generated using MultiSite Gateway cloning by combining three entry vectors (pMuLE ENTR U6 HIF1A sgRNA L1-R5, pMuLE ENTR U6 HIF2A sgRNA L1-R5, and pMuLE ENTR U6 HIF3A sgRNA L1-R5) with pMuLE ENTR SV40-hCas9 L5-L2 and a destination vector. For *HIF1A* and *HIF2A*, pMuLE Lenti Dest eGFP enabled fluorescent tracking, whereas for *HIF3A*, pMuLE Lenti Dest Neo facilitated antibiotic selection. The dual use of eGFP and neomycin markers allowed assessment of fluorescence-based versus antibiotic-based selection approaches for subsequent experiments.

Given that the destination vectors used had a size of approximately 9.2 kb, just below the 10 kb linearization threshold recommended by the protocol, initial cloning attempts were conducted without linearization but failed to yield any colonies. Subsequently, linearization was attempted using XhoI, which has a single restriction site within the backbone sequence (Figure 3.5A). This reaction produced only single colonies, with sequencing revealing incomplete and random fusion of vector fragments (data not shown). As an alternative, linearization was performed using SmaI, which cuts within the *ccDB* toxin gene that is removed during recombination, thus preserving the backbone as a single fragment. This resulted in colony formation for all three transfer vectors, representatively shown for the transfer vector targeting *HIF3A* (Figure 3.5B-D). The experimental transformation, in which all components for the assembly were combined, resulted in the formation of only a small number of

bacterial colonies on the selection plate (Figure 3.5B). This low number was consistent across vector constructs. A positive control transformation using the pUC19 plasmid carrying an ampicillin resistance gene produced a high number of colonies, confirming that the competent *E. coli* DH10B cells were viable and the transformation procedure was efficient (Figure 3.5C). In contrast, the negative control transformation with the destination vector alone, which contains the *ccDB* toxin gene, yielded no colonies (Figure 3.5D). This outcome confirmed the efficiency of negative selection, as the *ccDB* gene induces cell death in bacteria carrying non-recombined vectors.

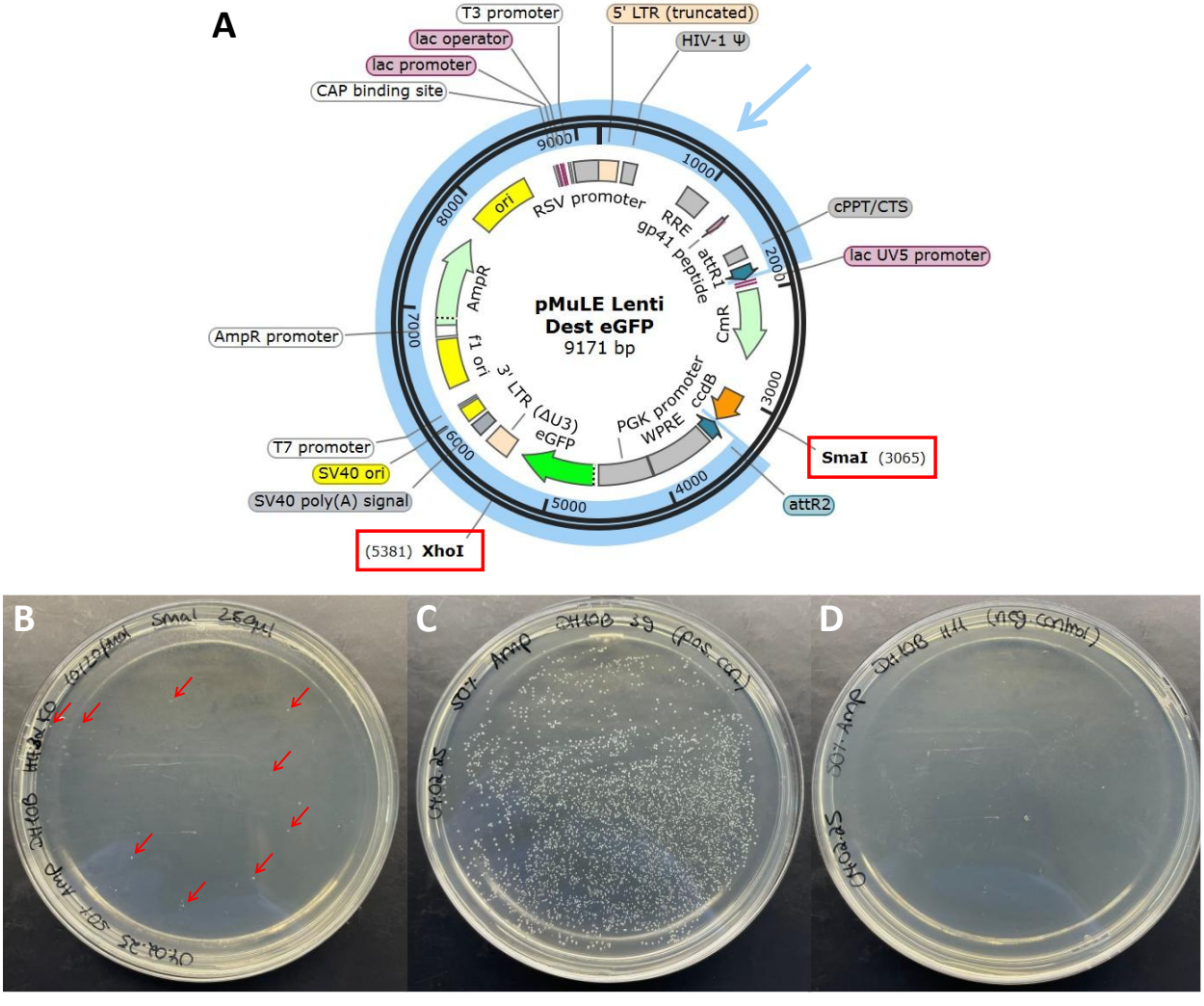

Figure 3.5 LB agar plates and plasmid map related to transfer vector generation. **(A)** Plasmid map of pMuLE Lenti Dest eGFP showing the backbone region (blue) and XhoI/SmaI restriction sites (red). The figure was created with SnapGene. **(B)** Experimental transformation of *E. coli* DH10B with pMuLE ENTR U6 HIF3A sgRNA L1-R5, pMuLE ENTR SV40-hCas9 L5-L2, and SmaI-linearized pMuLE Lenti Dest Neo to generate a single-knockout transfer vector targeting *HIF3A*. Red arrows indicate bacterial colonies. **(C)** Positive control using pUC19 plasmid to verify competent cell viability and confirm ampicillin resistance. **(D)** Negative control using the uncut destination vector carrying the *ccDB* toxin cassette to assess the efficiency of negative selection.

3.3.2. Verification of Transfer Vector Constructs

Plasmid DNA from individual colonies was analyzed by diagnostic restriction digestion using EcoRI. All selected plasmids corresponded to the expected sizes for each transfer vector, as summarized in Table 3.2. Representative gels of selected digested colonies are shown in Figure 3.6A

and 3.6B. To further confirm complete plasmid integrity, selected plasmids were sent for sequencing. For each plasmid, sequencing confirmed a correctly assembled sequence corresponding to the expected full-length construct. All transfer vectors contained a sgRNA expression cassette under the control of the U6 promoter derived from pMuLE ENTR U6 stuffer sgRNA scaffold L1-R5, and a hCas9 expression cassette driven by the SV40 promoter from pMuLE ENTR SV40-hCas9 L5-L2. The *HIF1A*- and *HIF2A*-targeting constructs incorporated a lentiviral backbone containing regulatory and packaging elements, as well as an eGFP reporter cassette. In contrast, the *HIF3A*-targeting construct contained the same backbone structure but incorporated a neomycin resistance cassette instead of the eGFP reporter. Sequence analysis confirmed full identity with the reference sequences for the pMuLE Lenti U6 HIF1A sgRNA SV40-hCas9 eGFP (Figure C) and pMuLE Lenti U6 HIF2A sgRNA SV40-hCas9 eGFP (Figure D) constructs. In the pMuLE Lenti U6 HIF3A sgRNA SV40-hCas9 Neo construct (Figure E), minor differences were detected, including small insertions, deletions, and point mutations localized to non-coding regions of the plasmid.

Table 3.2 Transfer plasmids analyzed by diagnostic restriction digestion. List of constructed transfer plasmids, their total sizes, and the corresponding fragment sizes obtained after EcoRI digestion, as verified by agarose gel electrophoresis.

Transfer Vector	Total Size (bp)	Fragment Sizes (bp)
pMuLE Lenti U6 HIF1A sgRNA SV40-hCas9 eGFP	12 461	6827, 4208, 987, 439
pMuLE Lenti U6 HIF2A sgRNA SV40-hCas9 eGFP	12 461	6827, 4208, 987, 439
pMuLE Lenti U6 HIF3A sgRNA SV40-hCas9 Neo	12 540	6906, 4208, 987, 439

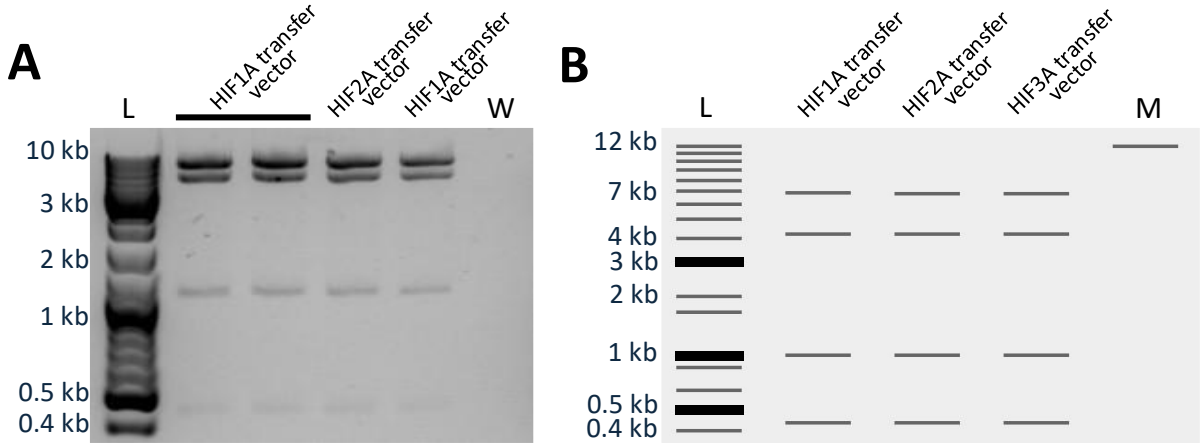

Figure 3.6 (continued on next page) Verification and visualization of pMuLE transfer vectors. **(A)** Representative gel of EcoRI-digested transfer vectors separated on a 1 % agarose gel stained with SYBR Safe. Gel was run at 120 V for 40 minutes. L – molecular weight ladder; M – mock digest; W – water control. **(B)** Simulated EcoRI digest showing expected fragment sizes, generated with Benchling.com. **(C-E)** Annotated plasmid maps of pMuLE Lenti U6 HIF1A sgRNA SV40-hCas9 eGFP **(C)**, pMuLE Lenti U6 HIF2A sgRNA SV40-hCas9 eGFP **(D)**, and pMuLE Lenti U6 HIF3A sgRNA SV40-hCas9 Neo **(E)**, generated with SnapGene.

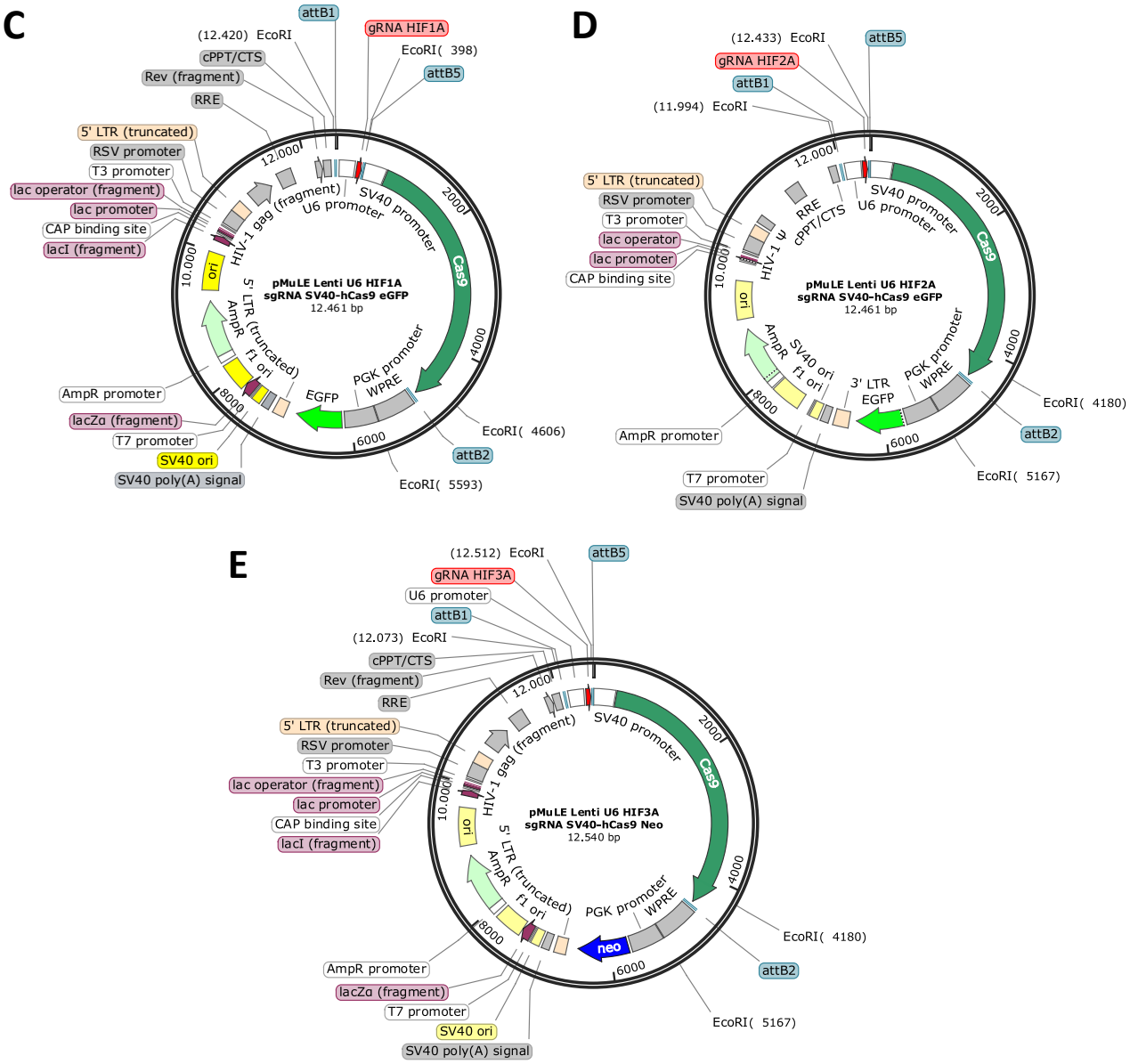

Figure 3.6 (continued) Verification and visualization of pMuLE transfer vectors. **(A)** Representative gel of EcoRI-digested transfer vectors separated on a 1 % agarose gel stained with SYBR Safe. Gel was run at 120 V for 40 minutes. L – molecular weight ladder; M – mock digest; W – water control. **(B)** Simulated EcoRI digest showing expected fragment sizes, generated with Benchling.com. **(C-E)** Annotated plasmid maps of pMuLE Lenti U6 HIF1A sgRNA SV40-hCas9 eGFP **(C)**, pMuLE Lenti U6 HIF2A sgRNA SV40-hCas9 eGFP **(D)**, and pMuLE Lenti U6 HIF3A sgRNA SV40-hCas9 Neo **(E)**, generated with SnapGene.

3.4. Optimization and production of Lentiviral Particles in HEK293T/17 Cells

Prior to lentiviral production, transfection conditions were optimized in HEK293T/17 cells to identify the most effective DNA:PEI mass ratio with minimal cytotoxicity. For this experiment, cells were transfected with the pMuLE Lenti U6 HIF2A sgRNA SV40-hCas9 eGFP transfer vector alone, excluding packaging and envelope plasmids, conditions later used for viral production. Transfection efficiencies were assessed at DNA:PEI mass ratios of 1:3, 1:4, and 1:5 (Figure 3.7A). The percentage of fluorescent cells was 1.72 % ± 0.01 for 1:3, 2.46 % ± 0.19 for 1:4, and 2.28 % ± 0.25 for 1:5 (Figure 3.7B). Statistical analysis showed a significant increase at 1:4 compared to 1:3 ($p < 0.01$), with no significant difference between 1:4 and 1:5 ($p > 0.05$). Although 1:4 yielded the highest mean

efficiency, the 1:5 condition exhibited greater variability and increased cytotoxicity, as evident by more floating and detached cells (data not shown). Therefore, a DNA:PEI ratio of 1:4 was selected for subsequent lentiviral production, offering best transfection efficiency with acceptible cell viability.

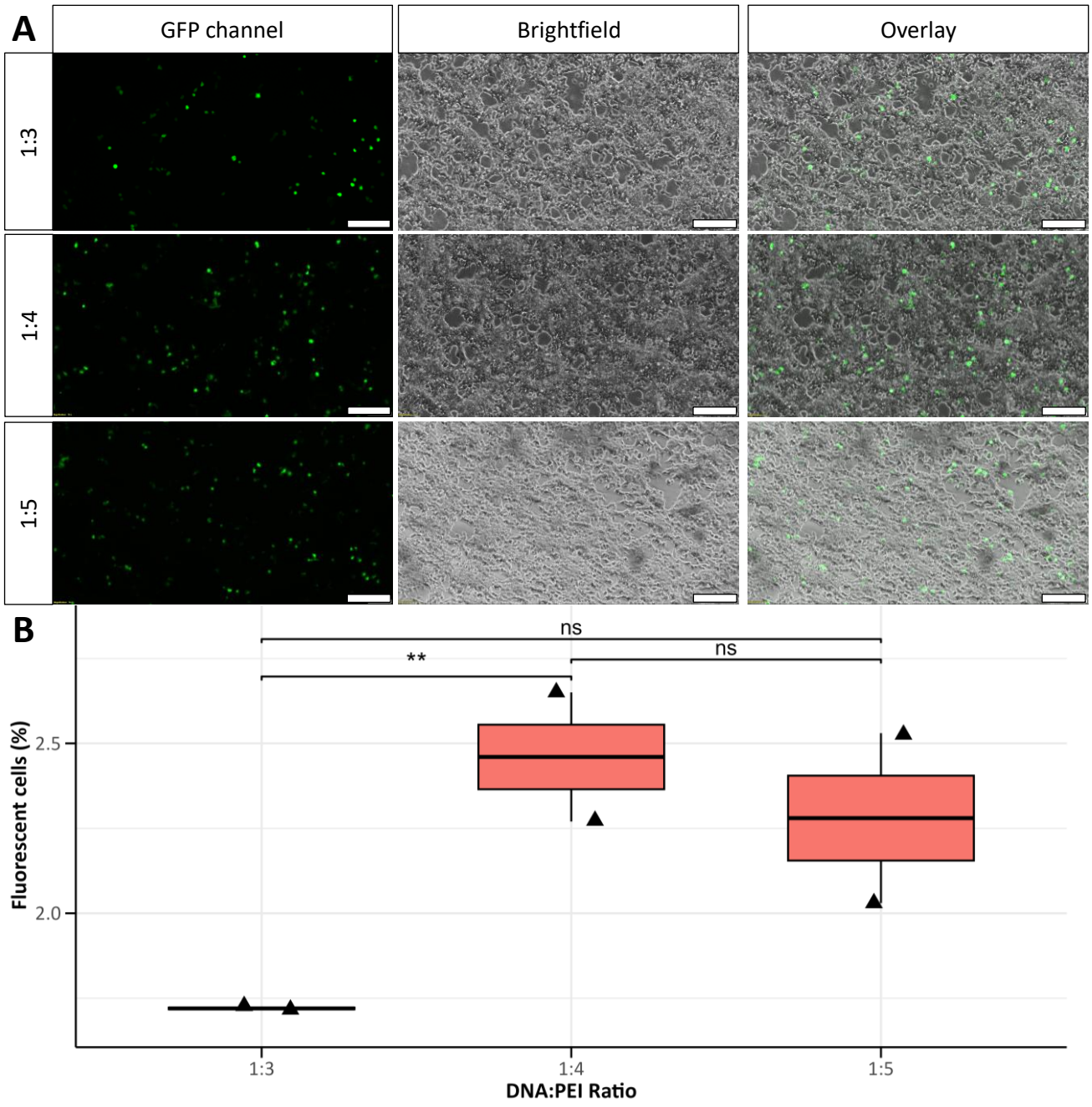

Figure 3.7 Optimization of transfection efficiency in HEK293T/17 cells for lentiviral particle production. **(A)** Representative fluorescence and brightfield images of HEK293T/17 cells transfected with pMuLE Lenti U6 HIF2A sgRNA SV40-hCas9 eGFP transfer vector at DNA:PEI ratios of 1:3, 1:4, and 1:5. Images were acquired 72 hours post-transfection using an OlympusIX83 inverted microscope and cellSens Dimension software with a 10× objective. Scale bar: 200 µm. **(B)** Quantification of the percentage of fluorescent cells for each DNA:PEI ratio (n = 2). Statistical significance was determined using t-test. ***p < 0.001; **p < 0.01; *p < 0.05; ns – not significant.

3.5. Lentiviral Transduction of MIA PaCa-2 Cells

Prior to performing gene knockout experiments, the functional titer of the produced lentiviral constructs was determined to ensure accurate and reproducible transduction. The efficiency of lentivirus production and transduction can vary considerably between viral batches, constructs, and target cell types (Dong & Kantor, 2021). Therefore, quantification of the infectious viral particles is essential. An optimal viral titer is critical to achieve an appropriate multiplicity of infection (MOI). Low titers result in insufficient transduction rates and inadequate representation of edited cells, whereas excessively high titers may cause multiple viral integration events per cell (Dong & Kantor, 2021) due to the simultaneous introduction of multiple sgRNAs and Cas9 molecules. Consequently, accurate titer determination enables standardized transduction conditions and minimizes variability between experiments. Two independent methods were employed to assess the functional titer of MuLE-based lentiviral preparations.

3.5.1. Determination of Functional Viral Titer by Fluorescence-Based Quantification

To assess transduction efficiency and determine functional viral titer, MIA PaCa-2 cells were transduced with serial dilutions of lentiviral supernatants carrying the MuLE constructs pMuLE Lenti U6 HIF1A sgRNA SV40-hCas9 eGFP and pMuLE Lenti U6 HIF2A sgRNA SV40-hCas9 eGFP, as already described in section 2.2.7. Fluorescence imaging was performed 72 hours post-transduction, and for each dilution three independent images were acquired.

For the *HIF1A*-targeting construct, transduction efficiencies were highest in the 1:1 condition, where nearly all cells exhibited eGFP fluorescence (Figure 3.8A). At the 1:10 dilution, the percentage of fluorescent cells dropped markedly to around 9 % followed by a gradual decline through the 1:25 and 1:50 dilutions, approaching near-background levels at the 1:100 dilution (Figure 3.8B). Statistical analysis using t-test showed highly significant differences between the 1:1 condition compared to more diluted samples ($p < 0.001$). For the *HIF1A*-targeting construct, a similar transduction pattern was observed across all dilutions (Figure 3.8C). The 1:1 virus dilution showed fluorescence for all visualized cells, while a decreasing trend could be observed from dilutions 1:10 onward, mirroring that seen with the *HIF1A*-targeting construct, with fluorescence progressively declining across 1:25 and 1:50, and reaching background levels by 1:100 (Figure 3.8D). Notably, fluorescence in the 1:1 viral dilution condition was significantly higher than all other dilutions ($p < 0.001$), which was comparable to the *HIF1A*-targeting construct.

Based on the transduction efficiencies, the functional viral titer was determined by averaging values calculated from the 1:10 to 1:50 dilutions, which yielded consistent and quantifiable transduction rates below the saturation threshold. The resulting titers were 1.07×10^5 TU/mL for the *HIF1A*-targeting construct and 1.44×10^5 TU/mL for the *HIF2A*-targeting construct. Applying

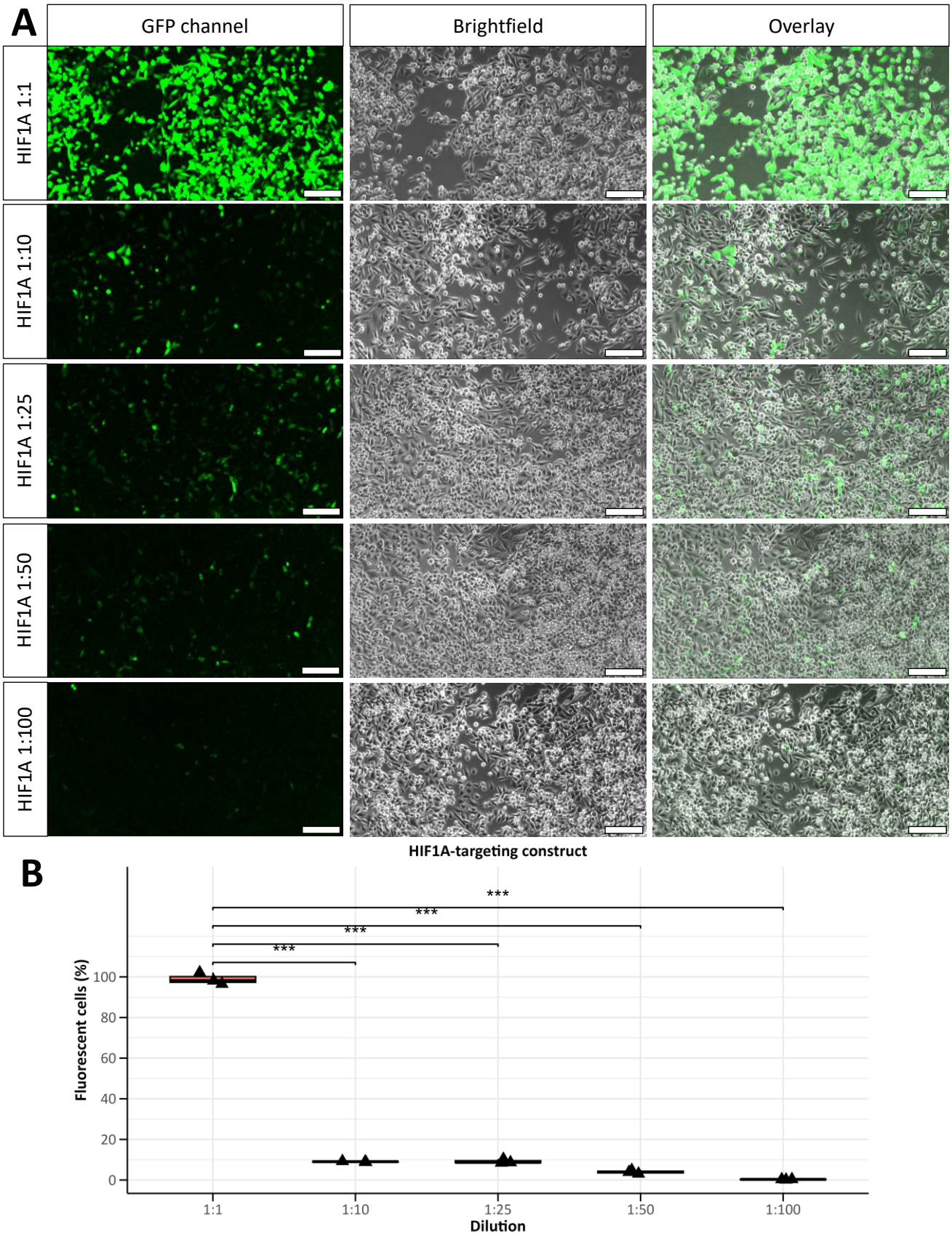

Figure 3.8 (continued on next page) Fluorescent quantification of transduced MIA PaCa-2 cells. **(A-B)** Cells transduced with the HIF1A-targeting construct. Fluorescent images (A) and measured percentage of fluorescent cells **(B)**. **(C-D)** Cells transduced with the HIF2A-targeting construct. Fluorescent images **(C)** and measured percentage of fluorescent cells **(D)**. Analysis was performed in Fiji (ImageJ, version 1.54p); scale bar: 200 µm; n = 3. Statistical significance was determined using t-test: ***p < 0.001; **p < 0.01; *p < 0.05; ns – not significant.

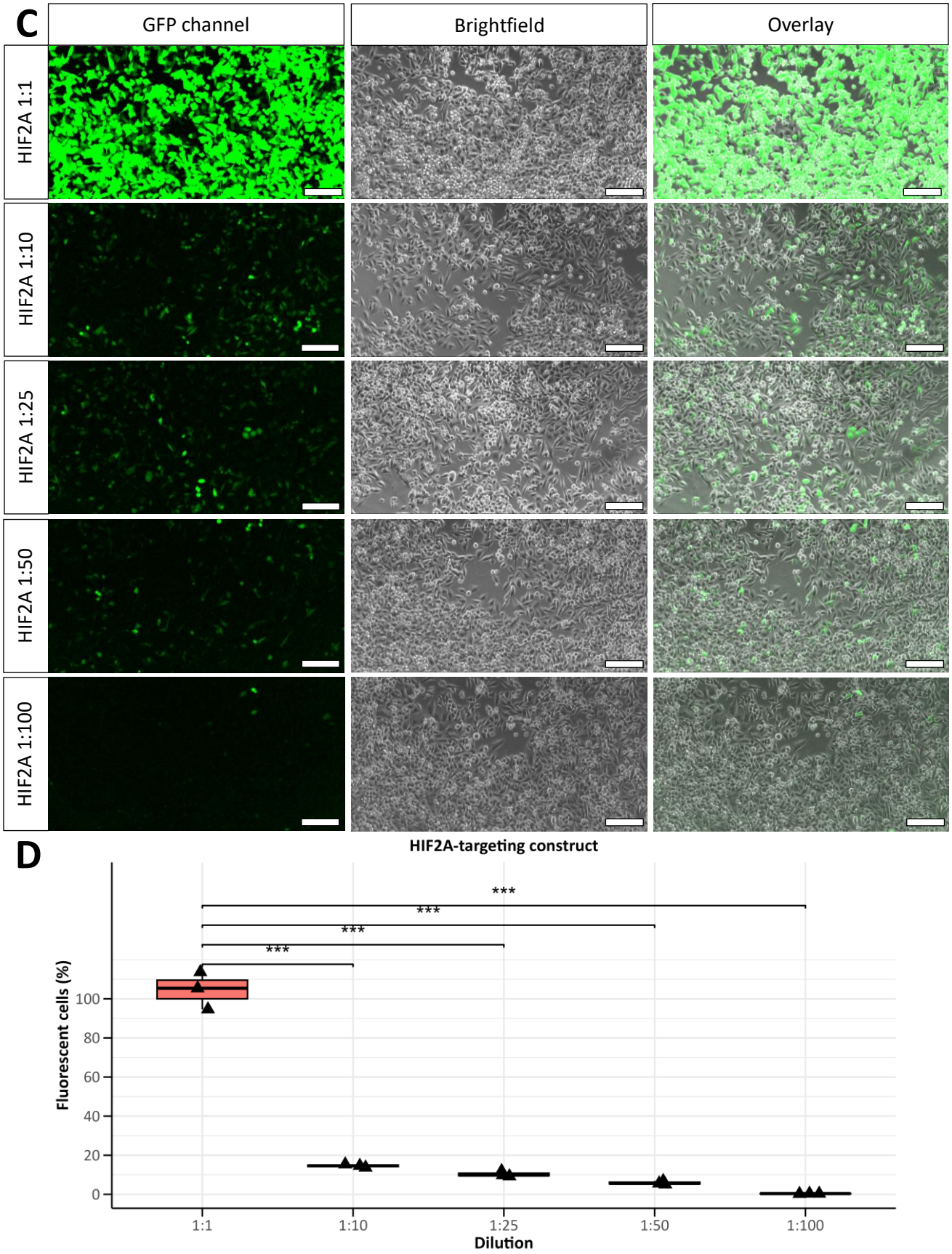

Figure 3.8 (continued) Fluorescent quantification of transduced MIA PaCa-2 cells. **(A-B)** Cells transduced with the HIF1A-targeting construct. Fluorescent images (A) and measured percentage of fluorescent cells **(B)**. **(C-D)** Cells transduced with the HIF2A-targeting construct. Fluorescent images **(C)** and measured percentage of fluorescent cells **(D)**. Analysis was performed in Fiji (ImageJ, version 1.54p); scale bar: 200 µm; n = 3. Statistical significance was determined using t-test: ***p < 0.001; **p < 0.01; *p < 0.05; ns – not significant.

1.5 mL of virus to 93 000 cells per well corresponded to a MOI of 1.72 for *HIF1A*- and 2.32 for *HIF2A*-targeting construct. These values indicate effective transduction efficiency under the applied conditions, with a clear dose-dependent response across dilutions.

3.5.2. Determination of Functional Viral Titer by Antibiotic Selection

Determination of appropriate antibiotic concentration

A G418 kill curve assay was performed to identify the optimal concentration for antibiotic selection (Figure 3.9). Cytotoxicity effects were first observed at concentrations ≥400 µg/mL by day two, with progressive cell detachment beginning at ≥500 µg/mL from day four onward. At concentrations ≥800 µg/mL, nearly all adherent cells were absent by day ten. On day 12, cell viabilty was assessed visually. No viable attached cells were detected at 900 µg/mL or 1000 µg/mL. Notably, high variability between replicates at 600 µg/mL and 1000 µg/mL was evident from additional quantitative viability measurements. Based on consistent loss of viability and complete detachment of adherent cells, 800 µg/mL was selected as the working concentration for G418-based selection.

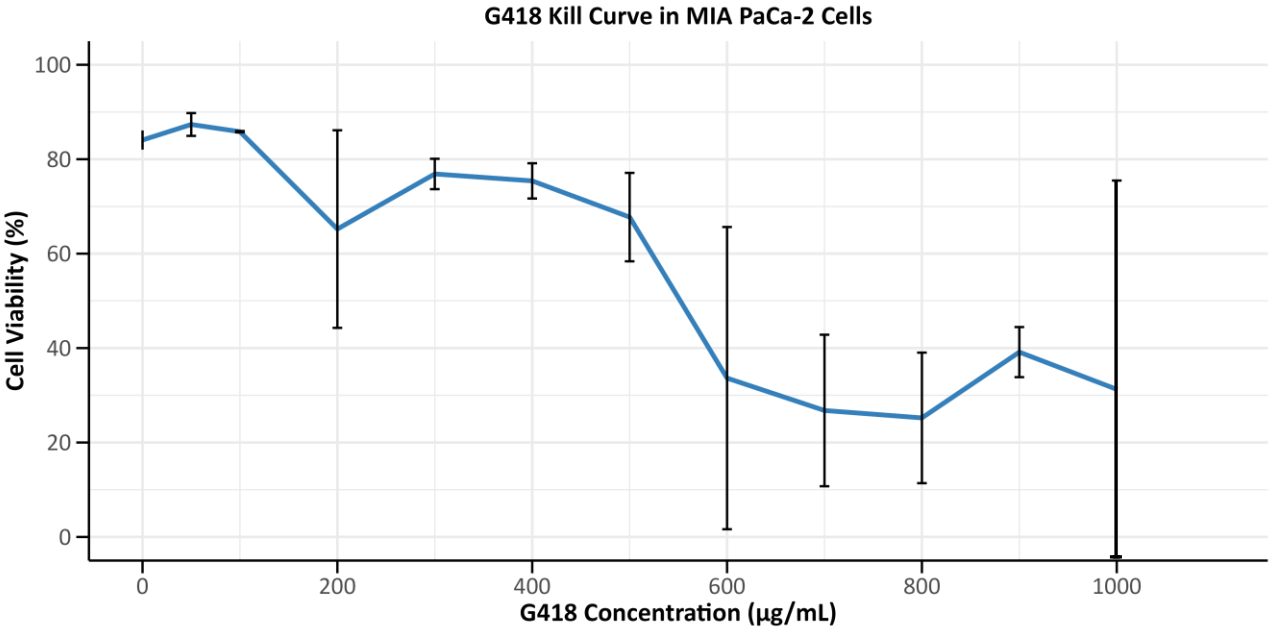

Figure 3.9 G418 kill curve in MIA PaCa-2 cells. MIA PaCa-2 cells were treated with increasing concentrations of G418 (from 0 µg/mL to 1000 µg/mL). Cell viability was assessed on day 12 using an automated cell counter and is presented as mean ± SD (n = 2).

Determination of Functional Viral Titer by Antibiotic Selection

To determine the functional titer of the *HIF3A*-targeting constructs, MIA PaCa-2 cells were transduced with serial dilutions of viral supernatant ranging from 1:1 to 1:1 000 000. Following selection with 800 µg/mL G418 for 12 days, surviving colonies were fixed, stained, and counted (Table 3.3 and Figure 3.10). At high viral concentrations (1:1 to 1:100), excessive cell survival precluded accurate colony quantification (data not shown). In contrast, higher dilutions (1:1000 to 1:1 000 000) yielded clearly distinguishable individual colonies. The functional titer was calculated

using colony counts from dilutions between 1:1000 and 1:100 000, excluding the most dilute condition (1:1 000 000). Based on these values, a functional titer of 5.38×10^5 TU/mL was determined, corresponding to a MOI of 8.68 under the applied experimental conditions.

Table 3.3 Number of colonies counted after antibiotic-based selection of *HIF3A*-targeting construct delivery.

Dilution	Number of Colonies
1:1000	152
1:10 000	57
1:100 000	17
1:1 000 000	7

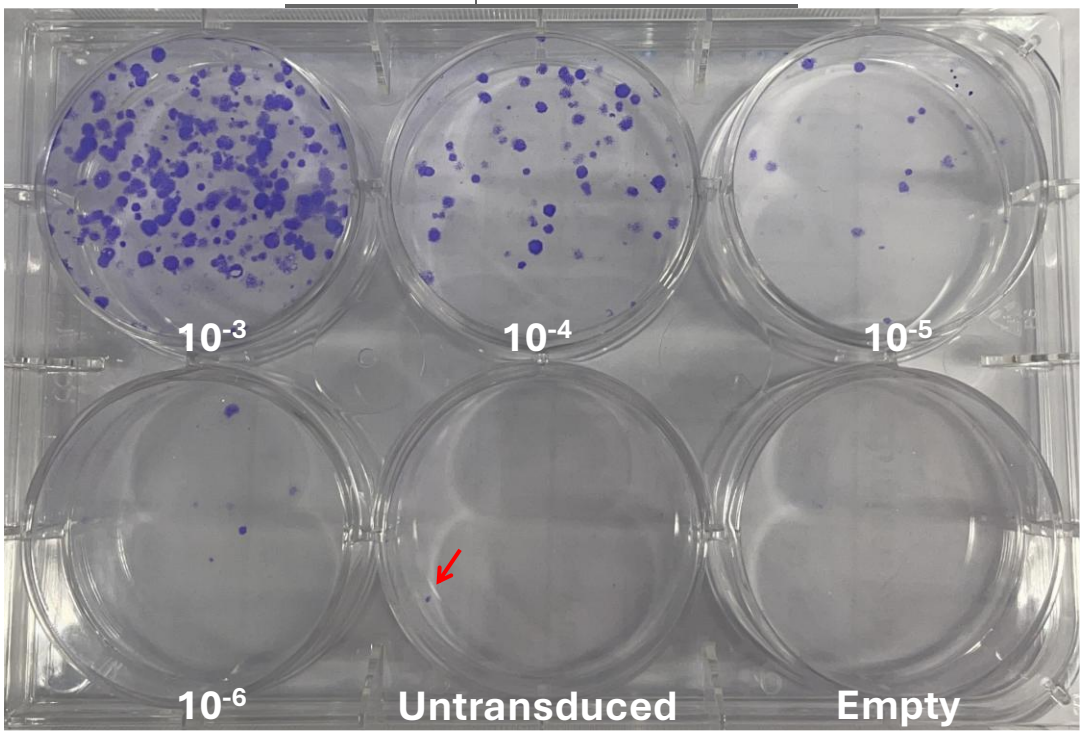

Figure 3.10 Antibiotic-based viral titer determination. MIA PaCa-2 cells transduced with *HIF3A*-targeting lentiviral constructs were selected with 800 µg/mL G418. Stained 6-well plate with viral dilutions from 1:1000 to 1:1 000 000 and an untransduced control. Staining was performed on day 12 post-transduction. The red arrow indicates a colony in the untransduced control.

3.6. Transcriptional Response of MIA PaCa-2 Cells to Hypoxia

Studying the early transcriptional response of pancreatic cancer cells to hypoxia using the MIA PaCa-2 *in vitro* model offers a distinct advantage over common *in vivo* models, as it enables precise oxygen control without interfering influences from the TME or stromal interactions. This allows for the investigation of the direct cellular transcriptional response to hypoxic conditions. The following section presents an analysis and comparison of gene expression levels of HIF isoforms and selected downstream targets in wild-type MIA PaCa-2 cells exposed to short-term (5 hours), intermediate (12 hours), and prolonged (24 hours) hypoxia, with or without pharmacological inhibition of HIF-1α by CAY10585.

3.6.1. Gene Expression Analysis

Collected wild-type MIA PaCa-2 cells at the described time points and under the specified conditions were used for total RNA extraction followed by cDNA synthesis for RT-qPCR (Figure 3.11A). Initially, the transcriptional response of *HIF1A*, *HIF2A*, and *HIF3A* was investigated to assess isoform-specific dynamics under hypoxia. Subsequently, the expression of key downstream targets involved in angiogenesis, metabolic adaptation, and cytoskeletal remodeling was evaluated. *VEGFA* and *VEGFC* were selected as markers of angiogenesis, *GLUT1* as a mediator of metabolic reprogramming, and *RHOC* as a contributor to cytoskeletal changes and invasiveness.

HIF1A: Expression in hypoxic cells remained close to normoxic baseline levels at 12 hours, while showing a slight decrease at 5 hours and a marked reduction at 24 hours. Treatment with the HIF-1α inhibitor CAY10585 induced a strong elevation of *HIF1A* transcript levels across all time points, peaking at 12 hours compared to untreated hypoxic samples.***HIF2A***: mRNA levels in untreated hypoxic controls exhibited consistent downregulation throughout the time course. In contrast, CAY10585 treatment led to sustained low expression at 5 hours, followed by a substantial increase at 12 hours and 24 hours.

HIF3A: *HIF3A* was the most strongly downregulated isoform under hypoxia, with the lowest levels recorded at 24 hours. Upon CAY10585 treatment, notable upregulation of *HIF3A* was observed, at 12 hours and 24 hours. The temporal pattern closely resembled that of *HIF2A* under the same conditions.

GLUT1: Expression in untreated hypoxic samples was markedly upregulated at 5 hours and 12 hours, before decreasing at 24 hours. CAY10585 further enhanced *GLUT1* expression at all time points, with maximal induction at 5 hours compared to untreated controls.

VEGFC: Expression exhibited an early moderate reduction under hypoxia after 5 hours, followed by pronounced suppression at 12 hours and 24 hours. Application of CAY10585 further exacerbated the downregulation of *VEGFC*, resulting in extremely low transcript levels under prolonged hypoxia.

RHOC: Expression remained largely stable at 5 hours under hypoxia, decreased moderately at 12 hours, and strongly declined at 24 hours. CAY10585 had only a marginal impact, causing slightly higher expression levels at 12 hours and 24 hours relative to untreated controls, yet remaining well below normoxic values.

VEGFA: Expression in hypoxic untreated samples progressively decreased, with the most pronounced suppression at 24 hours. CAY10585 administration led to a clear induction of *VEGFA* transcripts at 12 hours and 24 hours, indicative of a compensatory transcriptional response despite pharmacological inhibition of HIF-1α.

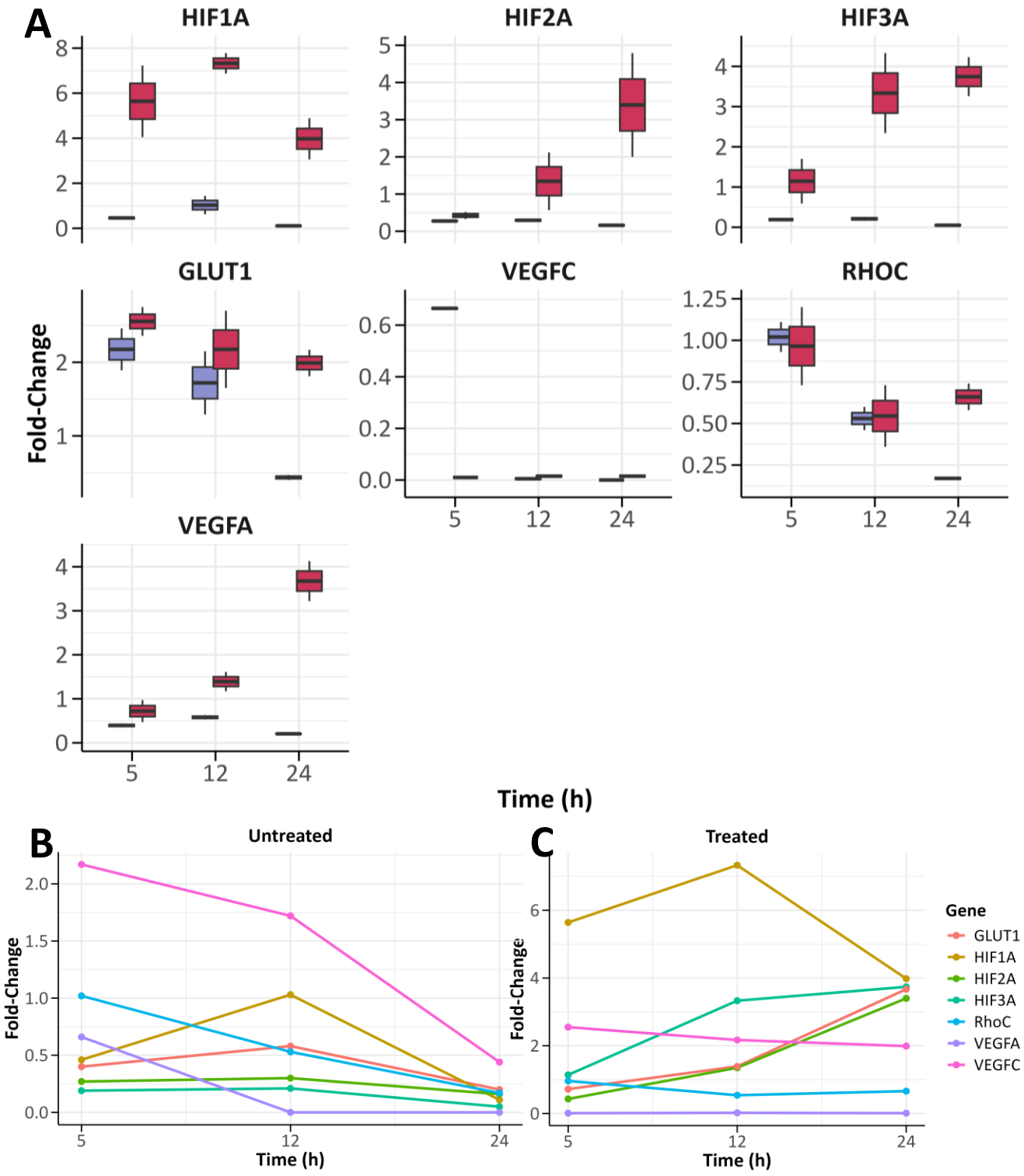

Figure 3.11 Time-dependent expression of HIF isoforms and downstream targets in MIA PaCa-2 cells. **(A)** Boxplots showing relative mRNA levels of selected genes after 5 hours, 12 hours, and 24 hours of hypoxia (1 % O_2). Blue = untreated; red = treated with 10 µM CAY10585. Expression values are normalized to *GAPDH*; n = 2. **(B)** Time-course plot of gene expression under hypoxia for untreated wild-type MIA PaCa-2 cells. (C) Time-course plot of gene expression under hypoxia for MIA PaCa-2 cells treated with 10 µM CAY10585. Data represent mean values (n = 2); plots are generated with R.

Analysis of hypoxia-related gene expression revealed distinct temporal regulation of HIF isoforms and their targets under low oxygen (Figure 3.11B). Inhibition of HIF-1α by CAY10585 induced compensatory upregulation of most genes, while others remained suppressed (Figure 3.11C).

4. Discussion

PDAC exhibits one of the most severe hypoxic profiles among solid tumors, contributing to its aggressive phenotype and resistance to therapy (Koong et al., 2000; Yuen & Díaz, 2014). HIFs are key transcriptional regulators of the adaptive response to low oxygen, yet their individual roles in PDAC remain incompletely understood. While *HIF1A* and *HIF2A* have been studied in various tumor contexts, the functional relevance of *HIF3A* and the interplay between isoforms in PDAC have not been systematically addressed (Zhou et al., 2011; Ravenna et al., 2016). Therefore, this thesis aimed to establish a MuLE-based CRISPR/Cas9 platform for generating single knockouts of *HIF1A*, *HIF2A*, or *HIF3A* in MIA PaCa-2 cells, and to assess the transcriptional response of wild-type cells to defined hypoxia (1 % O_2), with or without pharmacological HIF-1 α inhibition, thereby providing a foundation for future multiplexed knockout approaches and functional studies on isoform-specific roles of HIFs in PDAC.

4.1. Methodological Rationale for Choosing MuLE for Isoform-Specific Knockouts

The MuLE system was selected as a gene-editing tool for isoform-specific knockouts in MIA PaCa-2 cells due to its combination of stability, modularity, and scalability (Albers et al., 2015). This decision was based on both the biological characteristics of the cell model and the technical requirements for investigating hypoxia-regulated gene expression in PDAC. One of the primary advantages of the MuLE system lies in its ability to mediate stable transgene integration in mammalian cells via lentiviral delivery, along with its adaptability for transducing multiple sgRNAs and Cas9 from a single plasmid (Albers et al., 2015). In the context of this project, lentiviral delivery provides a stable and efficient system for gene expression, which is particularly advantageous for functional studies requiring stable gene disruption under prolonged hypoxic conditions, where transient expression methods would be inadequate.

Another key rationale for using MuLE was its capability for multiplexed genome editing (Albers et al., 2015). Since HIF isoforms are partially redundant and can exert both overlapping and antagonistic effects in hypoxic signaling (Ravenna et al., 2016; Zhang et al., 2017), single-gene knockout experiments may be insufficient to fully dissect isoform-specific functions. The MuLE system supports coordinated expression of multiple sgRNAs from a single lentiviral construct using MultiSite Gateway recombination (Albers et al., 2015), allowing future expansion of this study to include double- and triple-knockouts without major workflow adjustments.

In this study, MuLE constructs were designed to incorporate either the fluorescent reporter eGFP, or a neomycin resistance gene, highlighting the system‘s versatility and enabling a comparative evaluation of both selection strategies. The use of eGFP allowed rapid quantification of transduction efficiency, while neomycin selection facilitated stable enrichment of edited cell populations. Testing

both markers validated successful transgene delivery in MIA PaCa-2 cells and provided a basis for selecting the most suitable strategy for downstream applications. Moreover, this dual strategy enhances the adaptability of the system for future project extensions, including multiplexed knockout designs or clonal selection workflows.

Alternative delivery systems, such as adeno-associated viral (AAV) vectors or non-integrating plasmid-based systems, were not considered optimal for this study. AAV vectors have a limited packaging capacity of approximately 4.5 kb (Bak & Porteus, 2017), which is insufficient for the constructs used here, as their sizes approached 12.4 kb due to the inclusion of Cas9, sgRNA, and selectable markers. Plasmid transfection, although technically simpler, typically results in transient and heterogeneous expression (Tseng et al., 1997), making it unsuitable for the prolonged hypoxic culture and sustained functional analysis required in this context. In contrast, the MuLE system enables stable genomic integration via lentiviral delivery and supports modular, high-throughput construct assembly and combinatorial gene editing through MultiSite Gateway recombination (Albers et al., 2015).

4.2. Evaluation of the MuLE Cloning Workflow

The MuLE system workflow employed in this study was designed to generate lentiviral constructs enabling CRISPR/Cas9-mediated and isoform-specific knockout of *HIF1A*, *HIF2A*, or *HIF3A*. Originally introduced by Albers et al. (2015), the MuLE system was developed as a modular and flexible platform for assembling complex polycistronic constructs using MultiSite Gateway recombination. In their presentation of the system, Albers et al. (2015) reported cloning efficiencies of up to 90 %, 65 %, and 25 % for assemblies involving two, three, or four entry vectors, respectively. They also demonstrated that the resulting constructs remained stable in bacteria without evidence of unwanted recombination (Albers et al., 2015). While the modularity and directional control of the MuLE system were successfully reproduced, variable cloning efficiencies across different stages required protocol optimization to improve reproducibility and overall yield.

4.2.1. Assessment of Entry Vector Cloning Efficiency

The initial step of sgRNA cloning into donor vectors, while conceptually straightforward, offered important initial insights into the practical efficiency and reproducibility of the application of the MuLE system. Albers et al. (2015) demonstrated that the MuLE platform supports modular vector construction using donor vectors equipped with U6 promoters and Type IIS restriction sites, allowing directional insertion of guide sequences followed by ligation. In this work, the insertion of sgRNAs into BveI-digested and gel-purified donor backbones generally resulted in high transformation efficiency with a low frequency of background colonies (Figure 3.3). Minor variability in background

formation was observed, most likely due to contamination from uncut plasmid or incomplete separation of DNA fragments during gel purification.

To address this issue, dual antibiotic replica plating was employed to identify correctly recombined constructs. The donor vectors used in this study carried both a kanamycin resistance gene and a chloramphenicol resistance cassette embedded in a stuffer sequence between two BveI sites, which also included one of two EcoRI restriction sites. Upon BveI digestion, this stuffer fragment was excised and replaced in the subsequent ligation step by the annealed sgRNA oligonucleotide. Thus, following transformation, colonies containing successfully recombined entry vectors could be identified by their growth on kanamycin-only plates and lack of growth on plates containing both kanamycin and chloramphenicol. This negative selection method proved effective in distinguishing recombined clones from background arising due to the undigested or self-ligated vector.

Diagnostic restriction digestion provided additional verification. In the original donor vector, the presence of two EcoRI and one XhoI site yielded three DNA fragments upon digestion (Figure 3.4). In contrast, successful replacement of the stuffer fragment with the sgRNA insert eliminated one EcoRI site, resulting in only two visibile fragments in the gel. This pattern was consistently observed in all of the selected clones, supporting the interpretation that the stuffer sequence had been successfully removed and replaced. However, a notable limitation of this verification strategy is that it does not allow differentiation between specific sgRNA sequences or donor backbones. Given that multiple donor vectors of very similar length and restriction site architecture were used, plasmid variants could not be reliably distinguished by fragment size. As sequencing was not performed at this stage, entry vector identity was inferred based on the predefined cloning plan and physical separation of constructs during preparation. Despite this limitation, the combined use of replica plating and diagnostic digestion was considered adequate to confirm successful insertion.

4.2.2. Evaluation of Transfer Vector Assembly

Following successful generation of entry vectors, MultiSite Gateway LR recombination was used to assemble complete lentiviral transfer constructs.

Optimization of Gateway Recombination Efficiency

The system is designed to recombine multiple entry vectors into a destination vector through site-specific recombination between different *attL* and *attR* sites, enabling the directional assembly of complex constructs (Albers et al., 2015). Although the system is theoretically capable of rapidly generating polycistronic constructs (Albers et al., 2015), several technical limitations were encountered in practice that affected overall cloning efficiency.

Initial attempts to perform LR recombination using circular destination vectors consistently failed to produce viable colonies, despite proper stoichiometry and reaction conditions. Although the Gatway recombination protocol suggests linearization for destination vectors larger than 10 kb, the

vectors used in this study were approximately 9.2 kb in size – slightly below this threshold but already approaching the upper range for efficient recombination and bacterial transformation, as specified by the protocol. These failures were therefore attributed to the relatively large size of the destination plasmids, which may have reduced recombination efficiency or impaired transformation.

To address this, two strategies for linearization were tested. In the first attempt, the destination vector was digested with XhoI, which cuts within the plasmid backbone (Figure 3.5A). Although this enabled linearization of the vector, only isolated colonies were obtained after transformation. These displayed unexpected fragment sizes upon diagnostic EcoRI digestion. One plasmid from this condition was sequenced, which revealed nonspecific and incomplete recombination events (data not shown). Large portions of the construct were missing, and the assembly appeared random, with recombination occurring outside of the designated *att* sites. These findings suggest that cleavage of the plasmid backbone at non-permissive sites disrupted the structural integrity required for correct recombination, resulting in incorrect vector assembly.

A second approach using SmaI for linearization proved more effective. SmaI cuts within the toxin *ccdB* cassette, which is removed during successful Gateway recombination and replaced by the incoming entry vectors. Importantly, this strategy leaves the vector backbone intact and allows recombination to occur strictly between functional *att* sites. Under these conditions, colony formation was visibly improved, although still limited (Figure 3.5B). Instead of the 2000 to 15 000 colonies expected for two-fragment recombination, as indicated in the protocol, only five to ten colonies were observed per plate. Colonies appeared slowly, often requiring 20 hours of incubation to become visible, and a subset failed to grow further upon subculturing. This behavior likely reflects the large size and complexity of the assembled transfer vectors of approximately 12.4 kb, which are known to reduce plasmid stability, bacterial replication rates, and transformation efficiency (Chan et al., 2002).

Validation and Structural Integrity of Transfer Vectors

Despite the low yield, the colonies that successfully expanded were screened by EcoRI restriction digestion. All showed the expected banding patterns consistent with correct recombination (Figure 3.6A-B). From these, one representative clone per transfer construct was selected and validated using Oxford Nanopore sequencing. Full-length sequence analysis confirmed the successful assembly of the constructs and the preserved integrity of all inserted components, including sgRNA, Cas9, and reporter or selection cassettes, in the correct order and orientation (Figure 3.6C-E). These results underline that, while recombination efficiency was lower than anticipated, the fidelity of the MuLE system remained intact when appropriate linearization and selection strategies were employed.

While the Gateway-based MuLE system is presented as a rapid cloning strategy (Albers et al., 2015), our findings show that the actual timeline is extended due to the need for plasmid purification, bacterial expansion, verification steps, and the slow growth of large constructs. Although the

transformation efficiency was markedly lower than theoretical expectations, the clones obtained under optimized conditions were structurally correct and validated by sequencing, confirming that the MuLE system remains a reliable platform for constructing large, polycistronic lentiviral vectors – provided that critical technical adaptations are implemented.

4.3. Lentiviral Packaging and Titer Considerations

Efficient production of lentiviral particles is a critical step in CRISPR/Cas9-mediated gene editing workflows, particularly when aiming for stable genomic integration in target cells. In the context of the MuLE system, lentiviral vectors must deliver large and complex constructs that include Cas9, sgRNA, and selectable or reporter cassettes. Achieving sufficiently high viral titers is therefore essential to ensure reliable and reproducible transduction. While the MuLE system is theoretically compatible with high-efficiency packaging, practical limitations were encountered during viral production in this work.

4.3.1. Transfection Efficiency in HEK293T/17 Cells

To initially assess the efficiency of plasmid uptake, general transfection experiments were performed using HEK293T/17 cells (Figure 3.7A). These cells are widely used for lentiviral production due to their high transfectability and robust viral yield (American Type Culture Collection, 2024a). According to the provider‘s specifications and published data, transfection efficiencies in HEK293T/17 cells can reach up to 99 % under optimized conditions (American Type Culture Collection, 2024a). However, under the tested conditions in this work, the maximum transfection efficiency reached was 2.46 % $\pm$ 0.19, as determined by eGFP expression at a DNA:PEI ratio of 1:4 (Figure 3.7B). Importantly, no increase in cytotoxicity or evidence of increased cell death was observed at this ratio, suggesting that the DNA:PEI ratio was well tolerated but suboptimal in promoting efficient plasmid delivery.

A potential contributing factor to the low transfection efficiency was the deviation from the PEI preparation protocol. Literature indicates that transfection outcomes can be significantly influenced by PEI concentration, as it directly affects the physicochemical properties of the complexes and their ability to mediate cellular uptake (Sang et al., 2015). While the original protocol recommended preparing PEI at a concentration of 1 mg/mL, a lower concentration of 0.323 µg/mL was used in this study, with corresponding volume adjustments based on molecular weight ratios. PEI facilitates DNA delivery by forming polyplexes – positively charged complexes with the negatively charged plasmid DNA (Boussif et al., 1995). These polyplexes rely on a strong surface charge to bind to the cell membrane and enter the cell via endocytosis (Boussif et al., 1995). Once inside, PEI also plays a key role in endosomal escape, which disrupts the endosomal membrane and enables cytoplasmic release of the DNA (Boussif et al., 1995). When PEI is diluted, these processes can become less efficient due

to altered polyplex size, weaker charge interactions, and reduced buffering capacity (Boussif et al., 1995). Although the DNA:PEI mass ratio was maintained, the use of a more diluted PEI stock may have negatively affected complex formation and uptake, thereby contributing to the reduced transfection efficiency observed in this work.

4.3.2. Lentiviral Titer Outcome and Packaging Constraints

Following general transfection, lentiviral packaging was performed using the same DNA:PEI ratio and transfer vector, along with co-transfection of the second-generation packaging plasmids psPAX2 and pMD2.G (Figure 3.8). The resulting viral titers – 1.07×10^5 TU/mL for *HIF1A*-targeting construct, 1.44×10^5 TU/mL for *HIF2A*-targeting construct, and 5.38×10^5 TU/mL for the *HIF3A*-targeting construct – can be classified as moderate compared to the typical benchmark of 10^6 TU/mL and higher, achieved under optimized conditions (Albers et al., 2015). However, these titers were notably higher than those reported by Albers et al., (2015) for comparable plasmid sizes, where constructs around 12.5 kb yielded titers as low as 10^3 TU/mL. This suggests that while the overall transfection efficiency was reduced, the MuLE system remains effective even for large constructs when combined with a robust packaging protocol. The large size of the lentiviral vectors remains a key limiting factor, as it negatively impacts packaging efficiency and can also impair transcriptional activity and nuclear import in transfected cells (Albers et al., 2015).

In summary, lentiviral titers obtained in this work were limited by both large plasmid size and reduced transfection efficiency, which together constrained packaging success. While HEK293T/17 cells provide a well-established platform for lentiviral production (American Type Culture Collection, 2024a), the moderate transfection efficiency observed under the tested conditions likely limited the number of packaging-competent cells. Despite these constraints, transduction efficiency in MIA PaCa-2 cells was unexpectedly high relative to the measured titers and even exceeded those reported by Albers et al. (2015) for similarly sized constructs. This suggests that the functional quality of the viral particles produced was sufficient to achieve effective gene delivery.

4.4. Transduction Efficiency and Marker-Based Selection

4.4.1. Quantification of Transduction Efficiency and Functional Titers

The assessment of lentiviral transduction in MIA PaCa-2 cells revealed distinct patterns depending on the type of selection marker and the dilution of the viral supernatant. These observations not only reflect the performance of the MuLE-based constructs but also underscore the challenges associated with quantifying functional titers (Dong & Kantor, 2021), especially in a cell line known for its morphological variability and plasticity, such as MIA PaCa-2 (American Type Culture Collection, 2024b).

Two constructs, targeting *HIF1A* and *HIF2A*, were designed with an eGFP marker to facilitate fluorescence-based monitoring of transduction (Figure 3.8), while the *HIF3A*-targeting construct relies on neomycin resistance for antibiotic-based selection (Figure 3.10). At first glance, the calculated titers of 1.07×10^5 TU/mL for *HIF1A*, 1.44×10^5 TU/mL for *HIF2A*, and 5.38×10^5 TU/mL for the *HIF3A* – along with corresponding MOIs of 1.72, 2.32, and 8.68, respectively – suggested efficient transduction rates. This appears to align with the observed high fluorescence in cells transduced with the *HIF1A*- and *HIF2A*-targeting constructs. However, further verification is needed, particularly for the *HIF3A*-targeting construct, where the disproportionately elevated titer deviates from expected values. This apparent discrepancy indicates that calculated titers and MOI may not accurately reflect the effective viral load per cell. Such inconsistencies are frequently encountered in titering assays and often arise from inherent methodological assumptions underlying the calculation process (Geraerts et al., 2006). To obtain reliable titer estimates, only dilutions resulting in fluorescence in 40 % or fewer cells should be used, as this reduces undercounting caused by multiple integration events being registered as single transduction events. At the same time, dilutions must remain within the linear detection range to avoid overcounting due to background fluorescence or non-specific signals, as indicated by the protocols followed in this study. Accordingly, to ensure optimal accuracy, titers for eGFP-expressing constructs were calculated from dilutions from 1:10 to 1:50, while titers for neomycin-selected constructs were determined from colony counts at dilutions ranging from 1:1000 to 1:100 000. In cases such as the *HIF1A*-targeting construct, where near-complete fluorescence was observed at the 1:1 virus dilution, it is plausible that multiple viral particles were delivered per cell. This violates the assumption of single transduction events and leads to an underestimation of functional titer. Conversely, in the case of the *HIF3A*-targeting construct, where titer was calculated based on colony formation at higher dilution ratios, even minor inconsistencies due to pipetting or uneven colony distribution can significantly impact the titer estimation, which also led to the exclusion of the 1:1 000 000 dilution ratio (Geraerts et al., 2006). Nevertheless, this raises the possibility that the titer of the *HIF3A*-targeting construct was overestimated, which may explain the discrepancy between calculated titers.

4.4.2. Methodological Considerations of Selection Marker Systems

The use of two distinct selection markers – eGFP fluorescence and neomycin resistance – highlighted important methodological considerations regarding the accuracy and interpretability of transduction efficiency. eGFP-based monitoring is regarded as a precise approach for estimating functional titers, as successful transduction can be directly visualized via fluorescence (Geraerts et al., 2006). In many protocols, fluorescence-activated cell sorting (FACS) is employed to quantitatively assess the proportion of eGFP-positive cells, providing high-resolution, single-cell data (Geraerts et al., 2006). However, in this study, FACS analysis was not performed. Instead,

fluorescence estimation was conducted manually using fluorescence microscopy. This method introduces subjectivity and is particularly challenging in morphologically heterogeneous cell lines, such as MIA PaCa-2, with round and spindle-shaped cells that complicate automated cell segmentation and size-based analysis (Wang, 2012). To address this, total cell area and eGFP-positive area were quantified using Fiji (ImageJ), and the relative fluorescent area was used as a proxy for transduction efficiency. This approach was chosen for its reproducibility under the given experimental conditions.

In contrast, antibiotic selection using neomycin resistance provides a binary readout, with cells either surviving or dying under selection (Charrier et al., 2011). However, this method involves several additional complexities. The introduction of selection pressure may confer a proliferative or survival advantage to cells that received multiple viral integrations and therefore express higher levels of the resistance gene (Geraerts et al., 2006). Conversely, cells that were transduced only once may not express sufficient resistance protein to survive the antibiotic concentration used, resulting in their elimination despite successful transduction, thereby introducing bias into titer estimation (Geraerts et al., 2006). Moreover, variability in colony formation, uneven plating, and the difficulty of accurately counting colonies further limit the precision of this method (Geraerts et al., 2006). These limitations are particularly evident in the *HIF3A*-targeting sample, where small differences in colony numbers resulted in large variations in calculated titers between dilutions.

4.4.3. Limitations and the Need for Downstream Validation

Crucially, neither of the two selection strategies provides insight into the specific transduction outcome at the genomic or transcriptomic level (Wu et al., 2024). While both markers clearly show successful delivery of the lentiviral construct into MIA PaCa-2 cells, they do not confirm correct viral integration into the genome or functional gene knockout (Wu et al., 2024). Fluorescence and antibiotic resistance are indirect indices for transduction but provide no information on whether the sgRNA introduced via MuLE constructs effectively disrupted target genes (Geraerts et al., 2006). Furthermore, the presence of polyclonal populations complicates interpretation, as untransduced cells may still be present, and even transduced clones may vary in their editing outcomes due to possible off-target effects or multiple transduction events within the same cell (Geraerts et al., 2006). Therefore, while the current results confirm efficient lentiviral delivery and the initial potential for selection, further validation steps are essential. Monoclonal expansion by limiting dilution will be necessary to ensure that each derived line originates from a single, uniformly edited progenitor cell (Hong et al., 2024). Subsequent analysis, including RT-qPCR, protein expression profiling, and sequencing, will be required to confirm complete knockout of *HIF1A*, *HIF2A*, or *HIF3A*.

4.5. Transcriptional Dynamics Under Hypoxia and Pharmacological Modulation

Hypoxia is a key driver of tumor progression in pancreatic cancer, yet the transcriptional dynamics it induces remain insufficiently characterized, especially for specific models such as MIA PaCa-2 cells. Existing data under defined hypoxic conditions, particularly in combination with pharmacological inhibition, remain limited. Therefore, this part of the study aimed to establish the baseline transcriptional response to hypoxia in wild-type MIA PaCa-2 cells with or without pharmacological inhibition of HIF-1α. These results should serve as an important reference for comparison in subsequent experiments involving isoform-specific HIF knockouts and offer initial insight into how HIFs and their downstream targets respond under defined conditions.

4.5.1. Expression Patterns under Hypoxia

To evaluate the transcriptional dynamics of hypoxia in pancreatic cancer, expression levels of *HIF1A*, *HIF2A*, *HIF3A,* and selected hypoxia-responsive genes were analyzed by RT-qPCR at multiple time points of exposure to 1 % O_2 in MIA PaCa-2 cells (Figure 3.11). Target genes were chosen to reflect isoform-specific HIF regulation, with *VEGFA* and *GLUT1* representing well-characterized HIF-1α targets (Jiang et al., 1996; Akakura et al., 2001; McGinn et al., 2017), *VEGFC* reported as HIF-2α-dependent (Ndiaye et al., 2019), and *RHOC* described as a downstream effector of HIF-3α in hypoxic pancreatic cancer (Zhou et al., 2018). At the same time, the choice of downstream genes allowed a functional readout across angiogenesis, metabolic, and invasive pathways in the context of differential HIF isoform expression.

All three HIF-α isoforms underwent transcriptional repression over the course of hypoxic exposure. This trend was most pronounced for *HIF3A*, which exhibited near-complete loss of mRNA expression. The suppression of *HIF1A* mRNA aligns with previous observations in MIA PaCa-2 and other models, where transcriptional downregulation co-occurs with protein accumulation due to post-translational stabilization (Wang et al., 2007; Lin et al., 2011; Jaśkiewicz et al., 2022). Meanwhile, the unexpected repression of *HIF2A* contradicts its proposed role as a chronic hypoxia responder in various tumor and endothelial cells (Lin et al., 2011; Jaśkiewicz et al., 2022). This deviation may be explained by the exceptionally low basal expression of *HIF2A* in MIA PaCa-2 and its potentially limited transcriptional competence. The profound decrease in *HIF3A* mRNA also stands in contrast to studies reporting increased expression and invasion-promoting activity of HIF-3α under hypoxia in pancreatic cancer cells (Zhou et al., 2018). These discrepancies may stem from post-transcriptional repression, or a temporal delay in transcriptional activation not captured within the analyzed timeframe.

Among downstream targets, *GLUT1* was the only gene to display a classical hypoxia-induced activation pattern. As a direct transcriptional target of HIF-1α (Akakura et al., 2001; McGinn et al.,

2017), *GLUT1* was strongly induced during early hypoxia, indicative of a rapid metabolic switch toward glycolysis. However, this upregulation was transient, with expression declining under sustained low oxygen. This behavior is consistent with previous studies reporting *GLUT1* mRNA destabilization during prolonged hypoxia (Lin et al., 2011), reflecting its primary regulation by early-phase HIF-1α protein stabilization.

VEGFA, a canonical HIF-1α target and key mediator of angiogenesis (Jiang et al., 1996; Liao & Johnson, 2007), did not follow the expected upregulation under hypoxia. Although it is also regulated by HIF-2α in other tumor types (Skuli et al., 2009; Lin et al., 2011), such regulation has not been reported in MIA PaCa-2. The transcriptional repression of *VEGFA* observed here may reflect a disconnect between HIF protein activity and gene transcription, or alternative regulatory layers such as microRNA interference or translational control. This interpretation is supported by previous reports showing increased VEGFA protein expression in hypoxic MIA PaCa-2 despite limited transcriptional changes (Bao et al., 2022).

VEGFC, which has been proposed to be a HIF-2α-dependent gene but not a HIF-1α target (Ndiaye et al., 2019), showed complete transcriptional downregulation under hypoxia. Given that *HIF2A* expression was also suppressed, this finding likely reflects the loss of positive HIF-2α-driven transcription. Importantly, prior work suggests that HIF-2α may suppress *VEGFC* mRNA while simultaneously promoting its protein expression (Ndiaye et al., 2019), highlighting the complexity of post-transcriptional regulation.

RHOC expression also declined over time, which aligns with the observed repression of *HIF3A*. *RHOC* has been shown to be a direct transcriptional target of HIF-3α in hypoxic MIA PaCa-2 cells, contributing to cytoskeletal remodeling and invasion (Zhou et al., 2018). The parallel suppression of both genes in this study suggests that the HIF-3α-RhoC axis was not activated under the applied hypoxic conditions. This may reflect insufficient duration of hypoxia to trigger the invasive program, or a requirement of additional cofactors.

The transcriptional profile of hypoxia-exposed MIA PaCa-2 cells reveals a complex regulatory landscape dominated by mRNA repression rather than induction. Despite the transient upregulation of *GLUT1*, likely driven by early HIF-1α activity, the downregulation of *VEGFA*, *VEGFC*, and *RHOC* suggests limited engagement of angiogenic and invasive programs at the transcriptional level. However, given previous reports demonstrating discordance between mRNA and protein levels – for example, the hypoxia-induced accumulation of HIF-1α protein despite transcriptional repression (Wang et al., 2007) – further analysis of protein expression is essential to determine whether the observed transcriptional downregulation translates into lower functional activity.

4.5.2. Effects of HIF-1α Inhibition by CAY10585 on Hypoxia Response

To simulate transient loss of HIF-1 α activity and investigate potential compensatory mechanisms, MIA PaCa-2 cells were treated with the small molecule inhibitor CAY10585 under 1 % O_2 for the same time points as before without additional treatment (Figure 3.11). CAY10585 has been shown to selectively inhibit HIF-1 α at the protein level, suppressing its accumulation and transcriptional activity, but does not interfere with mRNA directly (Minegishi et al., 2013). Thus, this pharmacological approach was employed as a functional mimic of *HIF1A* knockout to obtain preliminary insights into isoform redundancy and adaptive responses prior to stable gene editing.

Compared to untreated hypoxia, CAY10585 treatment led to a dramatic upregulation of *HIF1A* mRNA, with expression increasing by more than 7-fold at 12 hours. Under hypoxia alone, *HIF1A* transcript levels remained near baseline or were strongly downregulated. This result contrasts sharply with previous literature reporting *HIF1A* mRNA downregulation under hypoxia (Wang et al., 2007; Lin et al., 2011; Jaśkiewicz et al., 2022), and instead suggests a feedback loop where inhibition of HIF-1α protein triggers compensatory transcriptional upregulation. Similar mRNA increases have been observed under other HIF-1α-targeted interventions (McGinn et al., 2017).

Notably, *HIF2A* and *HIF3A* were also induced under CAY10585 treatment, in stark contrast to the consistent transcriptional downregulation of both isoforms under hypoxia alone. By 24 hours, *HIF2A* and *HIF3A* were expressed at 3- to 4-fold higher levels compared to normoxic conditions, whereas they remained below baseline in untreated hypoxia samples. These findings support the idea that HIF isoforms exhibit functional compensation when HIF-1α is impaired.

Among downstream targets, *GLUT1* remained stably upregulated under CAY10585 across all time points, showing slightly higher or sustained levels relative to untreated hypoxia samples. Since *GLUT1* is a well-established direct target of HIF-1α (Akakura et al., 2001; McGinn et al., 2017), the maintenance of its expression suggests that HIF-1α inhibition was either incomplete or that *GLUT1* transcription may be maintained by HIF-2α, whose expression was also elevated under treatment. This result is in line with findings that early *GLUT1* activation under hypoxia can persist due to mRNA stability or redundant transcription factor input (Lin et al., 2011).

VEGFA, which was repressed under hypoxia alone, exhibited a striking reversal with strong induction under CAY10585 treatment. This change suggests that *VEGFA* transcription is restored or mediated, likely via increased HIF-2α levels. Indeed, *VEGFA* is a shared target of both HIF-1α and HIF-2α (Jiang et al., 1996; Skuli et al., 2009), and increased *VEGFA* expression has been observed in response to HIF-1α inhibition in endothelial cells (Tang et al., 2021). In contrast, *VEGFC* expression remained completely repressed under both hypoxic conditions, with or without CAY10585. This persistence suggests that HIF-2α does not act as a transcriptional activator of *VEGFC* in MIA PaCa-

2, consistent with prior studies indicating that it may suppress *VEGFC* mRNA while enhancing its protein expression through post-transcriptional mechanisms (Ndiaye et al., 2019).

RHOC, which was also suppressed under hypoxia alone, showed only slight changes with CAY10585 and remained transcriptionally repressed overall. This was unexpected given the observed increase in *HIF3A* mRNA, as HIF-3α has been shown to directly activate *RHOC* transcription under hypoxia in pancreatic cancer cells (Zhou et al., 2018). The lack of induction here may suggest that the transcriptional presence of HIF-3α alone is insufficient, and that *RHOC* regulation requires additional cofactors or post-translational activation of HIF-3α.

In summary, CAY10585 treatment under hypoxia induced a marked transcriptional reprogramming distinct from the untreated hypoxia response. The observed upregulation of all three HIF isoforms indicates robust transcriptional compensation for HIF-1 α inhibition. This was paralleled by a restoration or induction of key downstream genes such as *VEGFA* and *GLUT1*, highlighting possible redundancy and isoform substitution within the HIF network. Conversely, the continued repression of *VEGFC* and *RHOC* despite elevated upstream regulators underscores the complexity of transcriptional control and the potential involvement of post-transcriptional or epigenetic mechanisms. These findings indicate that pharmacological inhibition of HIF-1α does not fully replicate the effects of genetic deletion at the transcriptional level, highlighting the necessity of follow-up studies involving protein-level analyses and stable *HIF1A* knockout models to accurately assess functional consequences.

Conclusions

1. Entry vectors encoding sgRNAs targeting *HIF1A*, *HIF2A*, or *HIF3A* were successfully generated using restriction enzyme-based cloning into MuLE donor plasmids, and verified by diagnostic restriction digestion and antibiotic selection.
2. Functional lentiviral transfer vectors for single HIF isoform knockouts were assembled by MultiSite Gateway recombination, integrating sgRNA targeting *HIF1A*, *HIF2A*, or *HIF3A*, and SV40-driven hCas9 into either a MuLE destination vector carrying eGFP (for *HIF1A* and *HIF2A* transfer vectors) or a neomycin resistance gene (for *HIF3A* transfer vector).
3. Functional lentiviral particles encoding CRISPR/Cas9 constructs for targeted *HIF1A*, *HIF2A*, or *HIF3A* knockout were generated using second-generation packaging in HEK293T/17 cells, yielding low-titer virus.
4. Transduction of MIA PaCa-2 cells with MuLE-based lentiviral constructs resulted in detectable eGFP expression or neomycin resistance, confirming the successful genomic integration of the delivered knockout constructs.
5. Transcriptional analysis of wild-type MIA PaCa-2 cells revealed a distinct hypoxia-induced gene expression profile at 1 % O_2, which was further modulated by pharmacological inhibition of HIF-1α, thereby establishing a baseline for future comparison with genetically modified MIA PaCa-2 cells.

Future perspectives

Ongoing efforts include the monoclonal selection and expansion of MIA PaCa-2 cells transduced with MuLE-based knockout constructs to isolate clonal populations for downstream analysis. Future work will aim to confirm successful gene disruption through sequencing of the targeted loci, accompanied by RT-qPCR and Western blot analysis to verify transcript and protein depletion of the respective HIF isoforms. Once validated, the generated knockout cell lines could be subjected to functional assays under both normoxic and hypoxic conditions to assess potential changes in proliferation, migration, invasion, EMT, and metabolic adaptation.

Complementary transcriptomic profiling may provide additional insights into isoform-specific regulatory networks and downstream effectors. Moreover, the generation of double and triple HIF knockouts using the MuLE system would enable a more comprehensive characterization of functional redundancy and interaction among *HIF1A*, *HIF2A*, and *HIF3A*. Such investigations may contribute to a deeper understanding of HIF-driven hypoxic signaling in pancreatic cancer and help identify novel targets for therapeutic interventions in PDAC.

Author's Personal Contribution

I contributed to the refinement of the research idea by identifying necessary protocol adaptations and methodological adjustments throughout the project to ensure feasibility and reproducibility. Together with RM, I conducted experiments, including the cultivation and maintenance of bacterial and mammalian cell cultures, the generation of lentivirus, MuLE CRISPR/Cas9 knockouts, and RT-qPCR for gene expression analysis. I optimized cell culture conditions under normoxic and hypoxic conditions, and contributed to protocol development, troubleshooting, result validation, and data analysis. I prepared the original draft of this thesis, including visual data representation and figures, integrating the findings and analysis. Revisions were made based on feedback from GR and RM.

Acknowledgements

First and foremost, I would like to express my deepest gratitude to my supervisor, Dr. Giancarlo Russo, for the opportunity to join his research group and for his invaluable guidance throughout this project. His expertise, support, and encouragement have been instrumental in shaping both my research and my development as a scientist.

I am especially grateful to PhD student Rūta Matulevičiūtė for her essential role in project planning, her assistance throughout the research process, and her invaluable help in refining my practical skills. Her patience, mentorship, and unwavering support have had a significant impact on my work, and I truly appreciate her dedication.

I also extend my sincere thanks to members of other working groups, particularly Neringa Daugelavičienė and Eimina Dirvelytė from the group of Urtė Neniškytė, Andrius Jasinevičius from the group of Aušra Sasnauskienė, and Eglė Jakubauskienė for sharing their expertise with Rūta and me, guiding us in working with mammalian cells and lentivirus, and providing us with the opportunity to conduct research in their laboratories and with their equipment.

Lastly, I would like to acknowledge the entire Russo group for fostering a warm and stimulating work environment, making this experience both productive and enjoyable. I am especially grateful to Lina Aitmanaitė for always being available to answer questions and for her helpful suggestions throughout the project.

References

Akakura, N., Kobayashi, M., Horiuchi, I., Suzuki, A., Wang, J., Chen, J., Niizeki, H., Kawamura, K., Hosokawa, M., & Asaka, M. (2001). Constitutive Expression of Hypoxia-inducible Factor-1α Renders Pancreatic Cancer Cells Resistant to Apoptosis Induced by Hypoxia and Nutrient Deprivation1. *Cancer Research*, *61*(17), 6548–6554.

Albers, J., Danzer, C., Rechsteiner, M., Lehmann, H., Brandt, L. P., Hejhal, T., Catalano, A., Busenhart, P., Gonçalves, A. F., Brandt, S., Bode, P. K., Bode-Lesniewska, B., Wild, P. J., & Frew, I. J. (2015). A versatile modular vector system for rapid combinatorial mammalian genetics. *The Journal of Clinical Investigation*, *125*(4), 1603–1619. https://doi.org/10.1172/JCI79743

American Type Culture Collection (2024a). HEK293T/17 SF (ACS-4500) [Cell line]. Available from: https://www.atcc.org/products/acs-4500, accessed [23. March 2025].

American Type Culture Collection (2024b). MIA PaCa-2 (CRL-1420) [Cell line]. Available from: https://www.atcc.org/products/crl-1420, accessed [20. February 2025].

Arany, Z., Huang, L. E., Eckner, R., Bhattacharya, S., Jiang, C., Goldberg, M. A., Bunn, H. F., & Livingston, D. M. (1996). An essential role for p300/CBP in the cellular response to hypoxia. *Proceedings of the National Academy of Sciences*, *93*(23), 12969–12973. https://doi.org/10.1073/pnas.93.23.12969

Bak, R. O., & Porteus, M. H. (2017). CRISPR-mediated Integration of Large Gene Cassettes using AAV Donor Vectors. *Cell Reports*, *20*(3), 750–756. https://doi.org/10.1016/j.celrep.2017.06.064

Bao, Y.-Y., Zhong, J.-T., Shen, L.-F., Dai, L.-B., Zhou, S.-H., Fan, J., Yao, H.-T., & Lu, Z.-J. (2022). Effect of Glut-1 and HIF-1α double knockout by CRISPR/CAS9 on radiosensitivity in laryngeal carcinoma via the PI3K/Akt/mTOR pathway. *Journal of Cellular and Molecular Medicine*, *26*(10), 2881–2894. https://doi.org/10.1111/jcmm.17303

Bigos, K. J., Quiles, C. G., Lunj, S., Smith, D. J., Krause, M., Troost, E. G., West, C. M., Hoskin, P., & Choudhury, A. (2024). Tumour response to hypoxia: Understanding the hypoxic tumour microenvironment to improve treatment outcome in solid tumours. *Frontiers in Oncology*, *14*. https://doi.org/10.3389/fonc.2024.1331355

Boussif, O., Lezoualc'h, F., Zanta, M. A., Mergny, M. D., Scherman, D., Demeneix, B., & Behr, J. P. (1995). A versatile vector for gene and oligonucleotide transfer into cells in culture and in vivo: Polyethylenimine. *Proceedings of the National Academy of Sciences of the United States of America*, *92*(16), 7297–7301. https://doi.org/10.1073/pnas.92.16.7297

Bray, F., Laversanne, M., Sung, H., Ferlay, J., Siegel, R. L., Soerjomataram, I., & Jemal, A. (2024). Global cancer statistics 2022: GLOBOCAN estimates of incidence and mortality worldwide for 36 cancers in 185 countries. *CA: A Cancer Journal for Clinicians*, *74*(3), 229–263. https://doi.org/10.3322/caac.21834

Chan, V., Dreolini, L. F., Flintoff, K. A., Lloyd, S. J., Mattenley, A. A. (2002). The Effect of Increasing Plasmid Size on Transformation Efficiency in Escherichia coli. *Journal of Experimental Microbiology and Immunology, 2*, 207-223.

Charrier, S., Ferrand, M., Zerbato, M., Précigout, G., Viornery, A., Bucher-Laurent, S., Benkhelifa-Ziyyat, S., Merten, O. W., Perea, J., & Galy, A. (2011). Quantification of lentiviral vector copy numbers in individual hematopoietic colony-forming cells shows vector dose-dependent effects on the frequency and level of transduction. *Gene Therapy*, *18*(5), 479–487. https://doi.org/10.1038/gt.2010.163

Chee, J. Y. & Foan Chin, C. (2015). Gateway Cloning Technology: Advantages and Drawbacks. *Cloning & Transgenesis, 4,* 1.

Chen, Z., Han, F., Du, Y., Shi, H., & Zhou, W. (2023). Hypoxic microenvironment in cancer: Molecular mechanisms and therapeutic interventions. *Signal Transduction and Targeted Therapy*, *8*(1), 1–23. https://doi.org/10.1038/s41392-023-01332-8

Cockman, M. E., Masson, N., Mole, D. R., Jaakkola, P., Chang, G.-W., Clifford, S. C., Maher, E. R., Pugh, C. W., Ratcliffe, P. J., & Maxwell, P. H. (2000). Hypoxia Inducible Factor-α Binding and Ubiquitylation by the von Hippel-Lindau Tumor Suppressor Protein *. *Journal of Biological Chemistry*, *275*(33), 25733–25741. https://doi.org/10.1074/jbc.M002740200

Cong, L., Ran, F. A., Cox, D., Lin, S., Barretto, R., Habib, N., Hsu, P. D., Wu, X., Jiang, W., Marraffini, L. A., & Zhang, F. (2013). Multiplex Genome Engineering Using CRISPR/Cas Systems. *Science (New York, N.Y.)*, *339*(6121), 819–823. https://doi.org/10.1126/science.1231143

Cuesta-Borràs, E., Salvans, C., Arqués, O., Capdeville, J., Palmer, H. G., Puig, I. (2023) DPPA3-HIF1 α axis controls colorectal cancer chemoresistance by imposing a slow cell-cycle phenotype. *Cell Reports, 42,* 112927.

Dong, W., & Kantor, B. (2021). Lentiviral Vectors for Delivery of Gene-Editing Systems Based on CRISPR/Cas: Current State and Perspectives. *Viruses*, *13*(7), 1288. https://doi.org/10.3390/v13071288

Elegheert, J., Behiels, E., Bishop, B., Scott, S., Woolley, R. E., Griffiths, S. C., Byrne, E. F. X., Chang, V. T., Stuart, D. I., Jones, E. Y., Siebold, C., & Aricescu, A. R. (2018). Lentiviral transduction of mammalian cells for fast, scalable and high-level production of soluble and membrane proteins. *Nature Protocols*, *13*(12), 2991–3017. https://doi.org/10.1038/s41596-018-0075-9

Ferlay, J., Ervik, M., Lam, F., Laversanne, M., Colombet, M., Mery, L., Piñeros, M., Znaor, A., Soerjomataram, I., Bray, F. (2024). Global Cancer Observatory: Cancer Today. Lyon, France: International Agency for Research on Cancer. Available from: https://gco.iarc.who.int/today, accessed [20 January 2025].

Fujii, T., Inoue, N., Nobeyama, T., Inoue, J., Ogasawara, S., Otani, Y., Fujii, S., Ito, C., & Fukunaga, R. (2023). A simple, rapid, and efficient method for generating multigene-knockout culture cells by the CRISPR/Cas9 system. *Genes to Cells*, *28*(5), 390–397. https://doi.org/10.1111/gtc.13021

Garcia, C. J. G., Huang, Y., Fuentes, N. R., Turner, M. C., Monberg, M. E., Lin, D., Nguyen, N. D., Fujimoto, T. N., Zhao, J., Lee, J. J., Bernard, V., Yu, M., Delahoussaye, A. M., Sacarello, I. J., Caggiano, E. G., Phan, J. L., Deorukhkar, A., Molkentine, J. M., Saur, D., … Taniguchi, C. M. (2022). Stromal HIF2 Regulates Immune Suppression in the Pancreatic Cancer Microenvironment. *Gastroenterology*, *162*(7), 2018–2031. https://doi.org/10.1053/j.gastro.2022.02.024

Geraerts, M., Willems, S., Baekelandt, V., Debyser, Z., & Gijsbers, R. (2006). Comparison of lentiviral vector titration methods. *BMC Biotechnology*, *6*, 34. https://doi.org/10.1186/1472-6750-6-34

Gradiz, R., Silva, H. C., Carvalho, L., Botelho, M. F., & Mota-Pinto, A. (2016). MIA PaCa-2 and PANC-1 – pancreas ductal adenocarcinoma cell lines with neuroendocrine differentiation and somatostatin receptors. *Scientific Reports*, *6*(1), 21648. https://doi.org/10.1038/srep21648

Hao, X., Ren, Y., Feng, M., Wang, Q., & Wang, Y. (2021). Metabolic reprogramming due to hypoxia in pancreatic cancer: Implications for tumor formation, immunity, and more. *Biomedicine & Pharmacotherapy*, *141*, 111798. https://doi.org/10.1016/j.biopha.2021.111798

Heikkilä, M., Pasanen, A., Kivirikko, K. I., & Myllyharju, J. (2011). Roles of the human hypoxia-inducible factor (HIF)-3α variants in the hypoxia response. *Cellular and Molecular Life Sciences: CMLS*, *68*(23), 3885–3901. https://doi.org/10.1007/s00018-011-0679-5

Hong, T., Bae, S.-M., Song, G., & Lim, W. (2024). Guide for generating single-cell–derived knockout clones in mammalian cell lines using the CRISPR/Cas9 system. *Molecules and Cells*, *47*(7), 100087. https://doi.org/10.1016/j.mocell.2024.100087

Hu, J.-X., Zhao, C.-F., Chen, W.-B., Liu, Q.-C., Li, Q.-W., Lin, Y.-Y., & Gao, F. (2021). Pancreatic cancer: A review of epidemiology, trend, and risk factors. *World Journal of Gastroenterology*, *27*(27), 4298–4321. https://doi.org/10.3748/wjg.v27.i27.4298

Huang, C. K., Lv, L., Chen, H., Sun, Y., & Ping, Y. (2023). ENO1 promotes immunosuppression and tumor growth in pancreatic cancer. *Clinical and Translational Oncology*, *25*(7), 2250–2264. https://doi.org/10.1007/s12094-023-03114-8

Huang, R., & Zhou, P.-K. (2020). HIF-1 signaling: A key orchestrator of cancer radioresistance. *Radiation Medicine and Protection*, *1*(1), 7–14. https://doi.org/10.1016/j.radmp.2020.01.006

Jaśkiewicz, M., Moszyńska, A., Króliczewski, J., Cabaj, A., Bartoszewska, S., Charzyńska, A., Gebert, M., Dąbrowski, M., Collawn, J. F., & Bartoszewski, R. (2022). The transition from HIF-1 to HIF-2 during prolonged hypoxia results from reactivation of PHDs and HIF1A mRNA instability. *Cellular & Molecular Biology Letters*, *27*(1), 109. https://doi.org/10.1186/s11658-022-00408-7

Jeong, J.-W., Bae, M.-K., Ahn, M.-Y., Kim, S.-H., Sohn, T.-K., Bae, M.-H., Yoo, M.-A., Song, E. J., Lee, K.-J., & Kim, K.-W. (2002). Regulation and Destabilization of HIF-1α by ARD1-Mediated Acetylation. *Cell*, *111*(5), 709–720. https://doi.org/10.1016/S0092-8674(02)01085-1

Jiang, B.-H., Rue, E., Wang, G. L., Roe, R., & Semenza, G. L. (1996). Dimerization, DNA Binding, and Transactivation Properties of Hypoxia-inducible Factor 1 *. *Journal of Biological Chemistry*, *271*(30), 17771–17778. https://doi.org/10.1074/jbc.271.30.17771

Jiang, Z., White, R. A., & Wang, T. C. (2020). Adult Pancreatic Acinar Progenitor-like Populations in Regeneration and Cancer. *Trends in Molecular Medicine*, *26*(8), 758–767. https://doi.org/10.1016/j.molmed.2020.04.003

Jinek, M., Chylinski, K., Fonfara, I., Hauer, M., Doudna, J. A., & Charpentier, E. (2012a). A programmable dual RNA-guided DNA endonuclease in adaptive bacterial immunity. *Science (New York, N.Y.)*, *337*(6096), 816–821. https://doi.org/10.1126/science.1225829

Koong, A. C., Mehta, V. K., Le, Q. T., Fisher, G. A., Terris, D. J., Brown, J. M., Bastidas, A. J., & Vierra, M. (2000). Pancreatic tumors show high levels of hypoxia. *International Journal of Radiation Oncology, Biology, Physics*, *48*(4), 919–922. https://doi.org/10.1016/S0360-3016(00)00803-8

Lando, D., Peet, D. J., Gorman, J. J., Whelan, D. A., Whitelaw, M. L., & Bruick, R. K. (2002). FIH-1 is an asparaginyl hydroxylase enzyme that regulates the transcriptional activity of hypoxia-inducible factor. *Genes & Development*, *16*(12), 1466–1471. https://doi.org/10.1101/gad.991402

Lee, K. E., Spata, M., Bayne, L. J., Buza, E. L., Durham, A. C., Allman, D., Vonderheide, R. H., & Simon, M. C. (2016). Hif1a Deletion Reveals Pro-Neoplastic Function of B Cells in Pancreatic Neoplasia. *Cancer Discovery*, *6*(3), 256–269. https://doi.org/10.1158/2159-8290.CD-15-0822

Leibnitz Institute DSMZ (n.d.) German Collection of Microorganisms and Cell Cultures. MIA PaCa-2 (ACC733) [Cell line]. Available from: https://www.webshop.dsmz.de/en/human-animal-cell-lines/MIA-PACA-2.html, accessed [20 Februrary 2025].

Liao, D., & Johnson, R. S. (2007). Hypoxia: A key regulator of angiogenesis in cancer. *Cancer and Metastasis Reviews*, *26*(2), 281–290. https://doi.org/10.1007/s10555-007-9066-y

Lin, Q., Cong, X., & Yun, Z. (2011a). Differential hypoxic regulation of hypoxia-inducible factors 1α and 2α. *Molecular Cancer Research : MCR*, *9*(6), 757–765. https://doi.org/10.1158/1541-7786.MCR-11-0053

Loboda, A., Jozkowicz, A., & Dulak, J. (2010). HIF-1 and HIF-2 Transcription Factors—Similar but Not Identical. *Molecules and Cells*, *29*(5), 435–442. https://doi.org/10.1007/s10059-010-0067-2

Mahon, P. C., Hirota, K., & Semenza, G. L. (2001). FIH-1: A novel protein that interacts with HIF-1α and VHL to mediate repression of HIF-1 transcriptional activity. *Genes & Development*, *15*(20), 2675–2686. https://doi.org/10.1101/gad.924501

Makarova, K. S., Wolf, Y. I., Alkhnbashi, O. S., Costa, F., Shah, S. A., Saunders, S. J., Barrangou, R., Brouns, S. J. J., Charpentier, E., Haft, D. H., Horvath, P., Moineau, S., Mojica, F. J. M., Terns, R. M., Terns, M. P., White, M. F., Yakunin, A. F., Garrett, R. A., van der Oost, J., … Koonin, E. V. (2015). An updated evolutionary classification of CRISPR–Cas systems. *Nature Reviews. Microbiology*, *13*(11), 722–736. https://doi.org/10.1038/nrmicro3569

Mali, P., Yang, L., Esvelt, K. M., Aach, J., Guell, M., DiCarlo, J. E., Norville, J. E., & Church, G. M. (2013). RNA-Guided Human Genome Engineering via Cas9. *Science (New York, N.Y.)*, *339*(6121), 823–826. https://doi.org/10.1126/science.1232033

McCarty, N. S., Graham, A. E., Studená, L., & Ledesma-Amaro, R. (2020). Multiplexed CRISPR technologies for gene editing and transcriptional regulation. *Nature Communications*, *11*, 1281. https://doi.org/10.1038/s41467-020-15053-x

McGinn, O., Gupta, V. K., Dauer, P., Arora, N., Sharma, N., Nomura, A., Dudeja, V., Saluja, A., & Banerjee, S. (2017). Inhibition of hypoxic response decreases stemness and reduces tumorigenic signaling due to impaired assembly of HIF1 transcription complex in pancreatic cancer. *Scientific Reports*, *7*(1), 7872. https://doi.org/10.1038/s41598-017-08447-3

McGuigan, A., Kelly, P., Turkington, R. C., Jones, C., Coleman, H. G., & McCain, R. S. (2018). Pancreatic cancer: A review of clinical diagnosis, epidemiology, treatment and outcomes. *World Journal of Gastroenterology*, *24*(43), 4846–4861. https://doi.org/10.3748/wjg.v24.i43.4846

Minegishi, H., Fukashiro, S., Ban, H. S., & Nakamura, H. (2013). Discovery of Indenopyrazoles as a New Class of Hypoxia Inducible Factor (HIF)-1 Inhibitors. *ACS Medicinal Chemistry Letters*, *4*(2), 297–301. https://doi.org/10.1021/ml3004632

Nascimento-Filho, C. H. V., Glinos, A. T., Jang, Y., Goloni-Bertollo, E. M., Castilho, R. M., & Squarize, C. H. (2022). From Tissue Physoxia to Cancer Hypoxia, Cost-Effective Methods to Study Tissue-Specific O2 Levels in Cellular Biology. *International Journal of Molecular Sciences*, *23*(10), 5633. https://doi.org/10.3390/ijms23105633

National Cancer Institute. (n.d.). Pancreatic cancer – National Institutes of Health. Available from: https://www.cancer.gov/types/pancreatic, accessed [13 January 2025].

Ndiaye, P. D., Dufies, M., Giuliano, S., Douguet, L., Grépin, R., Durivault, J., Lenormand, P., Glisse, N., Mintcheva, J., Vouret-Craviari, V., Mograbi, B., Wurmser, M., Ambrosetti, D., Rioux-Leclercq, N., Maire, P., & Pagès, G. (2019). VEGFC acts as a double-edged sword in renal cell carcinoma aggressiveness. *Theranostics*, *9*(3), 661–675. https://doi.org/10.7150/thno.27794

Neuhöfer, P., Roake, C. M., Kim, S. J., Lu, R. J., West, R. B., Charville, G. W., & Artandi, S. E. (2021). Acinar cell clonal expansion in pancreas homeostasis and carcinogenesis. *Nature*, *597*(7878), 715–719. https://doi.org/10.1038/s41586-021-03916-2

Orth, M., Metzger, P., Gerum, S., Mayerle, J., Schneider, G., Belka, C., Schnurr, M., & Lauber, K. (2019). Pancreatic ductal adenocarcinoma: Biological hallmarks, current status, and future perspectives of combined modality treatment approaches. *Radiation Oncology*, *14*(1), 141. https://doi.org/10.1186/s13014-019-1345-6

Parandavar, E., & Yazdanparast, R. (2017). Differential impact of various reactive oxygen species (ROS) on HIF-1α/p53 direct interaction in SK-N-MC neuroblastoma cells. *Cell & Bioscience*, *7*(1), 52. https://doi.org/10.1186/s13578-017-0180-4

Park, W., Chawla, A., & O'Reilly, E. M. (2021). Pancreatic Cancer: A Review. *JAMA*, *326*(9), 851–862. https://doi.org/10.1001/jama.2021.13027

Pirona, A. C., Oktriani, R., Boettcher, M., & Hoheisel, J. D. (2020). Process for an efficient lentiviral cell transduction. *Biology Methods & Protocols*, *5*(1), bpaa005. https://doi.org/10.1093/biomethods/bpaa005

Qian, J., & Rankin, E. B. (2019). Hypoxia-Induced Phenotypes that Mediate Tumor Heterogeneity. *Advances in Experimental Medicine and Biology*, *1136*, 43–55. https://doi.org/10.1007/978-3-030-12734-3_3

Rakotomalala, A., Escande, A., Furlan, A., Meignan, S., & Lartigau, E. (2021). Hypoxia in Solid Tumors: How Low Oxygenation Impacts the "Six Rs" of Radiotherapy. *Frontiers in Endocrinology*, *12*, 742215. https://doi.org/10.3389/fendo.2021.742215

Rankin, E., & Giaccia, A. (2008). The role of hypoxia-inducible factors in tumorigenesis. *Cell Death and Differentiation*, *15*(4), 678–685. https://doi.org/10.1038/cdd.2008.21

Ravenna, L., Salvatori, L., & Russo, M. A. (2016). HIF3α: The little we know. *The FEBS Journal*, *283*(6), 993–1003. https://doi.org/10.1111/febs.13572

Rawla, P., Sunkara, T., & Gaduputi, V. (2019). Epidemiology of Pancreatic Cancer: Global Trends, Etiology and Risk Factors. *World Journal of Oncology*, *10*(1), 10–27. https://doi.org/10.14740/wjon1166

Sadozai, H., Acharjee, A., Kayani, H. Z., Gruber, T., Gorczynski, R. M., & Burke, B. (2024). High hypoxia status in pancreatic cancer is associated with multiple hallmarks of an immunosuppressive tumor microenvironment. *Frontiers in Immunology*, *15*. https://doi.org/10.3389/fimmu.2024.1360629

Salnikov, A. V., Liu, L., Platen, M., Gladkich, J., Salnikova, O., Ryschich, E., Mattern, J., Moldenhauer, G., Werner, J., Schemmer, P., Büchler, M. W., & Herr, I. (2012). Hypoxia Induces EMT in Low and Highly Aggressive Pancreatic Tumor Cells but Only Cells with Cancer Stem Cell Characteristics Acquire Pronounced Migratory Potential. *PLoS ONE*, *7*(9), e46391. https://doi.org/10.1371/journal.pone.0046391

Sang, Y., Xie, K., Mu, Y., Lei, Y., Zhang, B., Xiong, S., Chen, Y., & Qi, N. (2015). Salt ions and related parameters affect PEI–DNA particle size and transfection efficiency in Chinese hamster ovary cells. *Cytotechnology*, *67*(1), 67–74. https://doi.org/10.1007/s10616-013-9658-z

Sasaki, N., Gomi, F., Hasegawa, F., Hirano, K., Fujiwara, M., Toyoda, M., & Ishiwata, T. (2020). Characterization of the metastatic potential of the floating cell component of MIA PaCa-2, a human pancreatic cancer cell line. *Biochemical and Biophysical Research Communications*, *522*(4), 881–888. https://doi.org/10.1016/j.bbrc.2019.11.120

Schwörer, S., Cimino, F. V., Ros, M., Tsanov, K. M., Ng, C., Lowe, S. W., Carmona-Fontaine, C., & Thompson, C. B. (2023). Hypoxia Potentiates the Inflammatory Fibroblast Phenotype Promoted by Pancreatic Cancer Cell–Derived Cytokines. *Cancer Research*, *83*(10), 1596–1610. https://doi.org/10.1158/0008-5472.CAN-22-2316

Shi, R., Liao, C., & Zhang, Q. (2021). Hypoxia-Driven Effects in Cancer: Characterization, Mechanisms, and Therapeutic Implications. *Cells*, *10*(3), 678. https://doi.org/10.3390/cells10030678

Shi, Y., & Gilkes, D. M. (2025). HIF-1 and HIF-2 in cancer: Structure, regulation, and therapeutic prospects. *Cellular and Molecular Life Sciences*, *82*(1), 44. https://doi.org/10.1007/s00018-024-05537-0

Siegel, R. L., Kratzer, T. B., Giaquinto, A. N., Sung, H., & Jemal, A. (2025). Cancer statistics, 2025. *CA: A Cancer Journal for Clinicians*, *75*(1), 10–45. https://doi.org/10.3322/caac.21871

Simon, B., Weinel, R., Höhne, M., Watz, J., Schmidt, J., Körtner, G., & Arnold, R. (1994). *Frequent Alterations of the Tumor Suppressor Genes ~53 and DCC in Human Pancreatic Carcinoma*. *106*(6).

Singhal, A., Styers, H. C., Rub, J., Li, Z., Torborg, S. R., Kim, J. Y., Grbovic-Huezo, O., Feng, H., Tarcan, Z. C., Sahin Ozkan, H., Hallin, J., Basturk, O., Yaeger, R., Christensen, J. G., Betel, D., Yan, Y., Chio, I. I. C., de Stanchina, E., & Tammela, T. (2024). A Classical Epithelial State Drives Acute Resistance to KRAS Inhibition in Pancreatic Cancer. *Cancer Discovery*, *14*(11), 2122–2134. https://doi.org/10.1158/2159-8290.CD-24-0740

Skuli, N., Liu, L., Runge, A., Wang, T., Yuan, L., Patel, S., Iruela-Arispe, L., Simon, M. C., & Keith, B. (2009). Endothelial deletion of hypoxia-inducible factor–2α (HIF-2α) alters vascular function and tumor angiogenesis. *Blood*, *114*(2), 469–477. https://doi.org/10.1182/blood-2008-12-193581

Stoffel, E. M., Brand, R. E., & Goggins, M. (2023). Pancreatic Cancer: Changing Epidemiology and New Approaches to Risk Assessment, Early Detection, and Prevention. *Gastroenterology*, *164*(5), 752–765. https://doi.org/10.1053/j.gastro.2023.02.012

Storz, P. (2017). Acinar cell plasticity and development of pancreatic ductal adenocarcinoma. *Nature Reviews. Gastroenterology & Hepatology*, *14*(5), 296–304. https://doi.org/10.1038/nrgastro.2017.12

Tang, M., Bolderson, E., O'Byrne, K. J., & Richard, D. J. (2021). Tumor Hypoxia Drives Genomic Instability. *Frontiers in Cell and Developmental Biology*, *9*. https://doi.org/10.3389/fcell.2021.626229

Tao, J., Yang, G., Zhou, W., Qiu, J., Chen, G., Luo, W., Zhao, F., You, L., Zheng, L., Zhang, T., & Zhao, Y. (2021). Targeting hypoxic tumor microenvironment in pancreatic cancer. *Journal of Hematology & Oncology*, *14*, 14. https://doi.org/10.1186/s13045-020-01030-w

Tiwari, A., Tashiro, K., Dixit, A., Soni, A., Vogel, K., Hall, B., Shafqat, I., Slaughter, J., Param, N., Le, A., Saunders, E., Paithane, U., Garcia, G., Campos, A. R., Zettervall, J., Carlson, M., Starr, T. K., Marahrens, Y., Deshpande, A. J., … Bagchi, A. (2020). Loss of HIF1A From Pancreatic Cancer Cells Increases Expression of PPP1R1B and Degradation of p53 to Promote Invasion and Metastasis. *Gastroenterology*, *159*(5), 1882-1897.e5. https://doi.org/10.1053/j.gastro.2020.07.046

Tseng, W.-C., Haselton, F. R., & Giorgio, T. D. (1997). Transfection by Cationic Liposomes Using Simultaneous Single Cell Measurements of Plasmid Delivery and Transgene Expression *. *Journal of Biological Chemistry*, *272*(41), 25641–25647. https://doi.org/10.1074/jbc.272.41.25641

Vaupel, P., Flood, A. B., & Swartz, H. M. (2021). Oxygenation Status of Malignant Tumors vs. Normal Tissues: Critical Evaluation and Updated Data Source Based on Direct Measurements with pO2 Microsensors. *Applied Magnetic Resonance*, *52*(10), 1451–1479. https://doi.org/10.1007/s00723-021-01383-6

Vito, A., El-Sayes, N., & Mossman, K. (2020). Hypoxia-Driven Immune Escape in the Tumor Microenvironment. *Cells*, *9*(4), Article 4. https://doi.org/10.3390/cells9040992

Wang, C.-W. (2012). Fast automatic quantitative cell replication with fluorescent live cell imaging. *BMC Bioinformatics*, *13*, 21. https://doi.org/10.1186/1471-2105-13-21

Wang, F., Li, S. S., Segersvärd, R., Strömmer, L., Sundqvist, K.-G., Holgersson, J., & Permert, J. (2007). Hypoxia Inducible Factor-1 Mediates Effects of Insulin on Pancreatic Cancer Cells and Disturbs Host Energy Homeostasis. *The American Journal of Pathology*, *170*(2), 469–477. https://doi.org/10.2353/ajpath.2007.060489

Wang, G. L., & Semenza, G. L. (1995). Purification and Characterization of Hypoxia-inducible Factor 1 (∗). *Journal of Biological Chemistry*, *270*(3), 1230–1237. https://doi.org/10.1074/jbc.270.3.1230

Wani, A. K., Akhtar, N., Singh, R., Prakash, A., Raza, S. H. A., Cavalu, S., Chopra, C., Madkour, M., Elolimy, A., & Hashem, N. M. (2023). Genome centric engineering using ZFNs, TALENs and CRISPR-Cas9 systems for trait improvement and disease control in Animals. *Veterinary Research Communications*, *47*(1), 1–16. https://doi.org/10.1007/s11259-022-09967-8

Warburg, O., Wind, F., Negelein, E. (1926). The Metabolism of Tumors in the Body. The Journal of General Physiology, 519-510.

Wu, X., Zhou, X., Wang, Y., Wu, J., Liang, Q., Yang, X., Zhang, K., & Meng, S. (2024). Development and validation of a droplet digital PCR method for quantifying lentiviral vector infectious titer. *Heliyon*, *10*(20), e38512. https://doi.org/10.1016/j.heliyon.2024.e38512

Yang, H., Bailey, P., & Pilarsky, C. (2019). CRISPR Cas9 in Pancreatic Cancer Research. *Frontiers in Cell and Developmental Biology*, *7*. https://doi.org/10.3389/fcell.2019.00239

Yoo, Y., Kong, G., & Lee, M. (2006). Metastasis-associated protein 1 enhances stability of hypoxia-inducible factor-1α protein by recruiting histone deacetylase 1. *The EMBO Journal*, *25*(6), 1231–1241. https://doi.org/10.1038/sj.emboj.7601025

Yu, F., White, S. B., Zhao, Q., & Lee, F. S. (2001). HIF-1α binding to VHL is regulated by stimulus-sensitive proline hydroxylation. *Proceedings of the National Academy of Sciences*, *98*(17), 9630–9635. https://doi.org/10.1073/pnas.181341498

Yuen, A., & Díaz, B. (2014). The impact of hypoxia in pancreatic cancer invasion and metastasis. *Hypoxia*, *2*, 91–106. https://doi.org/10.2147/HP.S52636

Zeitouni, D., Pylayeva-Gupta, Y., Der, C. J., & Bryant, K. L. (2016). KRAS Mutant Pancreatic Cancer: No Lone Path to an Effective Treatment. *Cancers*, *8*(4), 45. https://doi.org/10.3390/cancers8040045

Zhang, Q., Lou, Y., Zhang, J., Fu, Q., Wei, T., Sun, X., Chen, Q., Yang, J., Bai, X., & Liang, T. (2017). Hypoxia-inducible factor-2α promotes tumor progression and has crosstalk with Wnt/β-catenin signaling in pancreatic cancer. *Molecular Cancer*, *16*(1), 119. https://doi.org/10.1186/s12943-017-0689-5

Zhou, L., Sokolskaja, E., Jolly, C., James, W., Cowley, S. A., & Fassati, A. (2011). Transportin 3 Promotes a Nuclear Maturation Step Required for Efficient HIV-1 Integration. *PLoS Pathogens*, *7*(8), e1002194. https://doi.org/10.1371/journal.ppat.1002194

Zhou, X., Guo, X., Chen, M., Xie, C., & Jiang, J. (2018). HIF-3α Promotes Metastatic Phenotypes in Pancreatic Cancer by Transcriptional Regulation of the RhoC–ROCK1 Signaling Pathway. *Molecular Cancer Research*, *16*(1), 124–134. https://doi.org/10.1158/1541-7786.MCR-17-0256

Appendix

Appendix A. Gene names used in the work

Gene Abbreviation	Full Name	Protein
ARNT	Aryl Hydrocarbon Receptor Nuclear Translocator	HIF-1β
CA9	Carbonic Anhydrase 9	CAIX
CD44	CD44 Molecule	CD44
CDH1	Cadherin 1	E-Cadherin
CDH2	Cadherin 2	N-Cadherin
CDKN2A	Cyclin Dependent Kinase Inhibitor 2A	p16
CREBBP	CREB Binding Protein	CBP
CTNNB1	Catenin Beta 1	β-Catenin
EGLN1/2/3	Egl-9 Family Hypoxia Inducible Factor	PHD1/2/3
EP300	E1A Binding Protein P300	p300
EPAS1	Endothelial PAS Domain Protein 1	HIF-2α
EPCAM	Epithelial Cell Adhesion Molecule	CD326
HIF1A	Hypoxia Inducible Factor 1 Subunit Alpha	HIF-1α
HIF1AN	Hypoxia Inducible Factor 1 Alpha Inhibitor	FIH
HIF2A	Hypoxia Inducible Factor 2 Subunit Alpha	HIF-2α
HIF3A	Hypoxia Inducible Factor 3 Subunit Alpha	HIF-3α
IL6	Interleukin 6	IL-6
KRAS	KRAS Proto-Oncogene, GTPase	KRAS
$KRAS^{G12D}$	KRAS G12D Mutant	$KRAS^{G12D}$
LDHA	Lactate Dehydrogenase A	LDHA
LOX	Lysyl Oxidase	LOX
MMP9	Matrix Metallopeptidase 9	MMP-9
MYC	MYC Proto-Oncogene, BHLH Transcription Factor	c-Myc
POU5F1	POU Class 5 Homeobox 1	OCT4
PROM1	Prominin-1	CD133
RHOC	Ras Homolog Family Member C	RhoC
ROCK1	Rho Associated Coiled-Coil Containing Protein Kinase 1	ROCK1
SLC2A1	Solute Carrier Family 2 Member 1	GLUT1
SMAD4	SMAD Family Member 4	SMAD4
SNAI1	Snail Family Transcriptional Repressor 1	Snail
SNAI2	Snail Family Transcriptional Repressor 2	Slug
TGDB1	Transforming Growth Factor Beta 1	TGF-β
TP53	Tumor Protein P53	p53
TWIST1	Twist Family BHLH Transcription Factor 1	Twist1
TWIST2	Twist Family BHLH Transcription Factor 2	Twist2
VEGFA	Vascular Endothelial Growth Factor A	VEGFA
VEGFC	Vascular Endothelial Growth Factor C	VEGFC
VHL	Von Hippel-Lindau Tumor Suppressor	VHL
VIM	Vimentin	Vimentin